# Transport and Assembly of Nanoparticles in a Tunable Nanofluidic Confinement

---

Dissertation

zur

Erlangung der naturwissenschaftlichen Doktorwürde
(Dr. sc. nat.)

vorgelegt der

Mathematisch-naturwissenschaftlichen Fakultät

der

Universität Zürich

von

Stefan Fringes

aus

Deutschland

Promotionskommission
Prof. Dr. Madhavi Krishnan (Vorsitz)
Dr. Armin W. Knoll (Leitung der Dissertation)
Prof. Dr. Stefan Seeger

Zürich, 2017

# Abstract

The investigation of nanoparticles in nanofluidic environments is particularly interesting because many mechanisms operate efficiently on the nanoscale. The stability of nanoparticles in such systems is governed by the interplay of repulsive and attractive forces. Understanding of the underlying physics is fundamental for particle transport, trapping and assembly. These manipulations of nano-objects are essential to develop novel lab-on-a-chip devices for diagnostics or to fabricate the next generation of nanoscale electronic devices.

In this thesis a novel and versatile setup is presented, which can confine and detect nanoparticles between two parallel and tunable surfaces. The upper confining surface is given by a modified cover-glass, which provides optical access to the nanofluidic slit with a high numerical aperture objective. The lower surface is typically a piece of a silicon wafer, which is coated with an oxide or polymer. The relative position of both surfaces can be precisely adjusted in five dimensions. By using piezo elements the gap distance can be handled with subnanometer accuracy and a parallelization of less than 1 nm vertical deviation over a distance of 10 $\mu$m is achieved.

An optical imaging technique, called interferometric scattering detection, is used to track the motion of the particles. This technique scales not only favorably with particle size but also enables the measurement of vertical distances in the system. The separation of the confining surfaces can be determined with subnanometer accuracy, while the position of spherical 60 nm gold particles can be identified with an accuracy of $< 10$ nm in the vertical direction and $< 5$ nm in the lateral direction, with a millisecond temporal resolution.

The stability of the setup is exploited in the measurement of the height and confinement dependent lateral diffusion coefficient of gold spheres between a glass and a polymer surface. A strong decay of the diffusion constant is observed with increasing confinement. The hindrance can not be explained by pure hydrodynamic effects alone and is most likely amplified by an electroviscous effect. An onset of subdiffusion is observed at strong confinement, which is correlated with a particle motion along paths with an increased gap distance, provided by the surface roughness.

The fact that particles preferentially sample areas of less confinement can be exploited to transport particles using a rocked Brownian Ratchet. The charged surfaces translate the 3D ratchet topography into a laterally asymmetric potential landscape under such conditions. This potential landscape can be visualized by measuring the empirical probability distribution of the particles. Their positions and thus the potential landscape can be resolved well below the diffraction limit. Comparison to theory allows the determination of intrinsic system parameters such as the Debye length or the height of the potential well. By applying a zero mean square wave electric field, particles are driven across the potential barriers along the shallow slopes, without a net fluid flow. The drift velocity is characterized in dependence of gap distance and applied electric field and a maximum drift velocity of up to $50\,\mu\text{m/s}$ is measured.

The trapping potential at a recessed structure can be increased by reducing the gap distance between the confining surfaces. It is observed that the particles jump and stay into contact with the polymer surface below a certain gap distance. The precision of the assembly process is below $10\,\text{nm}$. Furthermore, it is demonstrated that the method is scalable by depositing several gold spheres in parallel. Finally, the benefits of using a scanning probe patterning technique are exploited by overlaying an elongated topographical trap over two buried electrodes. The traps are used to confine and guide $4\,\mu\text{m} \times 0.04\,\mu\text{m}$ sized InAs nanowires into direct contact. The ability to cleanly evaporate the polymer after the deposition renders the assembly process independent of the underlying substrate.

# Zusammenfassung

Die Untersuchung von Nanopartikeln in einer nanofluidischen Umgebung ist besonders interessant, da viele Mechanismen erst effizient auf der Nano-Skala wirken. Die Stabilität von Nanopartikeln in solchen Systemen wird beherrscht durch das Wechselwirken von anziehenden und abstoßenden Kräften. Ein Verständnis der grundlegenden Physik ist wesentlich für den Transport, das Einfangen und das Absetzen von Partikeln. Solche Beeinflussungen von Nanoobjekten sind notwendig um für die Diagnostik neuartige Labore-auf-dem-Chip zu entwickeln oder um die nächste Generation elektronischer Bauteile im Nanobereich herzustellen.

In dieser Dissertation wird ein neuartiger und vielseitiger Aufbau präsentiert, mit dem man Nanopartikel zwischen zwei beweglichen und parallelen Oberflächen im Nanometer Bereich einschränken und beobachten kann. Ein modifiziertes Deckglas stellt die obere Begrenzungsfläche dar, welches den optischen Zugang zum nanofluidischem Spalt mittels eines Objektives mit hoher numerischer Apertur gewährleistet. Die untere Oberfläche ist typischerweise ein Stück eines Siliziumwafers, welches mit einem Oxid oder Polymer beschichtet ist. Die relative Lage der beiden Grenzflächen kann in fünf Dimensionen präzise eingestellt werden. Durch die Verwendung von piezoelektrischen Elementen kann der Abstand mit einer Genauigkeit von unter einem Nanometer eingestellt werden und es wird eine Parallelisierung von weniger als 1 nm vertikale Abweichung über die Distanz von 10 $\mu$m erreicht.

Eine optische Abbildungstechnik kommt zur Anwendung, die als interferometrische Streulicht Detektion bezeichnet wird, um die Bewegung der Teilchen zu verfolgen. Diese Technik skaliert nicht nur vorteilhaft für kleine Partikel, sondern sie ermöglicht auch das Messen vertikaler Distanzen. Der Abstand der einschränkenden Oberflächen kann mit einer Genauigkeit von unter einem Nanometer bestimmt werden, während die vertikale und laterale Position von sphärischen $60\,\mathrm{nm}$ Goldpartikeln jeweils mit einer Genauigkeit von $< 10\,\mathrm{nm}$ bzw. $< 5\,\mathrm{nm}$ bei einer zeitlichen Auflösung im Bereich von Millisekunden erkannt wird.

Die Stabilität des Aufbaus wird genutzt, um den lateralen Diffusionskoeffizienten der Goldkugeln zu bestimmen in Abhängigkeit

von ihrer Höhe und des Abstandes der einschränkenden Glas- und Polymeroberfläche. Ein starker Abfall des Diffusionskoeffizienten mit kleiner werdendem Spaltabstand wird gemessen. Die Verlangsamung kann nicht alleine durch hydrodynamische Effekte erklärt werden und wird wahrscheinlich durch einen elektroviskosen Effekt verstärkt. Das Einsetzen einer Subdiffusion wird bei starker Einschränkung beobachtet und es korreliert mit der Bewegung der Partikel entlang der Pfade mit erhöhtem Spaltabstand, bereitgestellt durch die Oberflächenrauigkeit.

Die Tatsache, dass Teilchen vorzugsweise die Gebiete mit einer geringeren Einschränkung besetzen, kann man sich zu eigen machen, um Partikel mit Hilfe einer wippenden Brownschen Ratsche zu transportieren. Unter solchen Gegebenheiten übertragen die geladenen Oberflächen die Topographie der 3D-Ratschen in eine laterale asymmetrische Potentiallandschaft. Diese Potentiallandschaft kann durch das Messen der empirischen Wahrscheinlichkeitsverteilung der Teilchen visualisiert werden. Ihre Positionen und damit die Potentiallandschaft können mit einer Auflösung weit unterhalb der Beugungsgrenze aufgelöst werden. Der Vergleich mit der Theorie erlaubt es, die intrinsischen Systemparameter wie die Debye-Länge oder die Höhe der Potentialwanne zu bestimmen. Durch Anlegen einer im Mittel verschwindenden elektrischen Rechteck-Spannung werden die Partikel entlang der flachen Steigungen über die Potentialbarrieren getrieben, während im Mittel keine Flüssigkeit bewegt wird. Die Driftgeschwindigkeit wird in Abhängigkeit des Spaltabstandes und des angelegten elektrischen Feldes charakterisiert und es wird eine maximale Driftgeschwindigkeit von bis zu $50\,\mu\text{m/s}$ gemessen.

Das Einfangpotential an einer vertieften Struktur kann erhöht werden, indem der Spaltabstand zwischen den Begrenzungsflächen verringert wird. Es wird beobachtet, dass die Goldpartikel ab einem gewissen Spaltabstand zur Polymeroberfläche springen und dort in Kontakt bleiben. Die Genauigkeit des Absetzprozesses ist unter 10 nm. Darüber hinaus wird durch das parallele Platzieren mehrere Goldsphären gezeigt, dass das Verfahren skalierbar ist. Schließlich werden die Vorteile der thermischen Rastersondenlithographie ausgenutzt, indem eine längliche topographische Falle ins Polymer gemeißelt wird an der Stelle wo zwei Elektroden vergraben sind. Die Fallen werden verwendet, um $4\,\mu\text{m} \times 0{,}04\,\mu\text{m}$ große InAs Nanodrähte einzuschränken und in direkten Kontakt zu führen. Die Fähigkeit, das Polymer nach der Abscheidung sauber zu verdampfen, macht den Montagevorgang unabhängig von dem darunterliegenden Substrat.

# Contents

# 1 Introduction

Synthesized nanoparticles and fabricated nanostructures often feature interesting size and material dependent optical, electrical, thermal and chemical properties, which are only apparent or become more pronounced when the dimensions of the material are reduced below 100 nm.

The size dependent band gap of semiconductor quantum dots makes them promising candidates for light-emitting diodes, photo-detectors and solar-cells [1] and they are already used today to realize true color high dynamic range displays [2, 3]. The increased surface to volume ratios of metallic nanoparticles enhances not only their catalytic properties and cooling power, but also their response to light due to surface plasmons [4, 5]. The potential of surface plasmons is immense and ranges from the realization of photonic circuits [6, 7] to chemical and biological sensors [8, 9].

Nevertheless, these nanostructures have to be integrated on a suitable surface in order to fabricate functional devices or to study their properties systematically. This can be done either by bottom-up (nanoparticle assembly) or top-down fabrication. The latter process is typically based on lithography and has been tremendously improved to continuously downscale the size of todays integrated circuits. However, the gating between the on and off state becomes less effective the smaller the devices get and more current starts to leak. All leading processor chip manufacturers address these problems by insulating the metal gate from the silicon channel with a high-$\kappa$ dielectric and changing the architecture from a planar to a fin based geometry [10]. The logical next step would be to fully wrap the gate around the conducting channel.

However, to fabricate more complex nanostructures with the top-down approach the number of involved process steps has to be increased a lot, which makes this method uneconomic at a certain point. Many of these structures can be produced by synthesis with less effort e.g. complex core-shell semiconducting nanowires [11, 12]. Furthermore, a separation of synthesis and assembly also facilitates the combination of new materials and structures which are difficult to integrate with standard CMOS processes e.g. carbon nanotubes. Recently, it has been demonstrated that a carbon nanotube transistor with a sub 10 nm gate length can outperform the speed and power of silicon devices with a similar size [13].

An assembly technique, which allows the precise placement of nanoparticles, could not only revolutionize nanoscale information technology [12, 14], but would also affect the fields of energy harvesting [15], and biological and chemical sensing [8, 16]. A variety of directed assembly techniques already exists with different advantages and limits. However, there is no universal assembly method which is capable of placing large varieties of arbitrarily shaped nano-objects, cost and time effective and with high precision. Therefore the development of new and the improvement of existing assembly techniques is still active and worthwhile.

## 1.1 Particle assembly techniques

To date there exist a myriad of assembly techniques; each of these has its own strengths and limitations. Several good reviews cover this topic and often focus on a particular particle type or the assembly technique e.g. the integration of colloidal spherical particles [17], nanowires [12] and directed self-assembly [18].

In this Section some of these techniques and the resulting devices are summarized, but there are also others which for example use bio-molecular linkers [19], superhydrophobic structures [20] or the micromanipulation of indium tips [21]. The focus here lies on the integration of nanowires, carbon nanotubes and plasmonic particles. In particular techniques such as mechanical printing and Langmuir-Blodgett have demonstrated the ability to assemble large arrays of such nanoparticles. However, both methods require a good particle alignment and distribution on the growth substrate and do not provide control over the placement on the single particle level. Such a control has been demonstrated by the techniques which assemble the particles out of a solution by utilizing e.g. capillary, dielectrophoretic and optical forces.

### Mechanical printing

Nanowires are commonly grown vertically on a substrate by a nanocluster catalyzed vapor-liquid-solid method (VLS). The nanowires can be transferred into dense parallel arrays by sliding the growth substrate over a sample with a defined applied force and speed. A big effort to realize nanowire based electronic devices has been conducted for example by the Lieber group in Harvard. They demonstrated an integrated nanowire based finite state machine [22]. The wires were assembled by separating the anchoring location from the alignment region, which resulted in parallel nanowire arrays with an alignment precision of $\pm 1^\circ$ [23]. Furthermore, they fabricated U-shaped 3D nanowire field-effects transistors with the help of localized anchoring structures. These devices can be used as bioelectric sensors, which record the action potential from electrogenic cells [24].

Parallel arrays of carbon nanotubes can be grown laterally on a quartz substrate by chemical vapor deposition (CVD). The nanotubes grow from uniform catalyst lines, which are patterned by lithography [25]. The nanotubes can be transferred to another substrate after evaporation of a gold layer and peeling both off with a thermal tape. The method can be used to transfer the nanotubes onto a sample with pre-patterned backside electrodes, which enabled the realization of a multitasking carbon nanotube computer [26] and transistors with a few nanometer short channel length [13, 27]. A similar growth and transfer process was used to realize integrated circuits on flexible plastic substrates [28].

### Langmuir–Blodgett

Particles suspended at an air-liquid interface can be first concentrated by a Langmuir–Blodgett trough. The particles are then deposited on the sample by dipping it into or pulling it out of the liquid. Close packed arrays of nanowires [29, 30], micro- and nanospheres [31, 32] have been assembled by this technique.

### Capillary assembly

In capillary assembly a droplet of colloidal suspension is moved over a topographycal structured surface. The particles then accumulate at the receding meniscus and are only deposited at the topographical guiding structures, due to capillary forces and the restoring force of the structure. The method works for particles with a size down to 2 nm and complex structures such as nanotetrapods [33]. Larger particles can be assembled on a single particle level [33, 34]. The orientation of elongated objects can be controlled by shaping the guiding structures accordingly [35]. Furthermore, patterning the guiding structures in a thermally decomposable polymer allows the transfer of aligned lines of nanorods to an arbitrary substrate without using a contact printing process, which usually alters the position of the particles [36].

### Electrostatic interactions

Sample regions or particles can be modified such that they have an opposite charge and thus selectively adsorb the particles. The selective patches can be masked by standard top-down fabrication techniques. For example, transistors based on individual silicon nanowires [37] as well as carbon nanotubes [38] have been realized utilizing this method. However, it seems to be difficult to control the number of deposited particles per patch [37] or to avoid that particles are assembled between two patches at small patch separations [38].

### Dielectrophoresis

Dielectrophoretic forces are optimally suited to assemble elongated particles on pre-patterned electrodes. In case the particle has a larger dielectric constant than the surrounding solution, a non-uniform electric field between the electrodes first polarizes the particle and then exerts an attractive force. The magnitude of the attractive force can be set *in-situ* by the applied voltage and frequency. Good control over the trapping strength and fluid flow enabled an implementation of a self-limiting single nanowire assembly process [39]. In combination with capillary forces and nanowire lift-off, large arrays of metallic and semi-conducting nanowire resonators were assembled, which could be used as biological and chemical sensors [40]. Metallic carbon nanotubes have a larger dielectric constant in comparison to semi-conducting tubes; thus the metallic ones get preferentially assembled [41].

### Optical stamping

Optical tweezers have been used to trap particles in the focus of a laser for almost 50 years [42] and are still very popular. In the first years dielectric particles where trapped by the gradient force towards the high intensity regions of the electromagnetic field, which resulted from an induced polarization of the particle by the field itself. It is more difficult to optically trap metallic particles, due to the strong scattering close to the surface plasmon resonance, but it is possible if the wavelength of the laser is sufficiently far away from this resonance [43]. The group of J. Feldmann from the LMU Munich has made tremendous progress in employing optical tweezers also as a nanofabrication tool. They exploited the repulsive scattering force of a focused laser with a wavelength close to plasmon resonance and printed 80 nm gold spheres directly out of solution onto a substrate with an accuracy better than 50 nm [44]. In a later experiment, the process was parallelized to a certain degree by creating several laser foci with a spatial light modulator [45]. The parallelization increased the assembly speed by factor of 30 to 6 particles per second, without altering the placement precision. The group also used a two-color optical printing technique to independently align and print gold nanorods [46]. However, the alignment accuracy was only ±17°. A limitation of this method is the minimum distance particles can be printed next to each other, which is approximately 300 nm [43].

## 1.2 Optical detection

In the last section several assembly techniques were presented. Handling the particles in a solution is very convenient, since the involved forces can often be tuned by the composition of the medium and a direct adsorption can be prevented. For the precise placement of particles at a desired location it seems to be crucial that the assembly process consists of three independent steps. First, the particles have to be transported to an area of influence. Second, the particles are trapped and aligned there and third, they are deposited without altering their position. The efficiency of the total assembly process is determined by all three steps. Therefore it is important to gain a fundamental understanding not only for the deposition itself, but also for the transport and trapping of nanoparticles in a fluidic environment.

Since the days of Antonie van Leeuwenhoek in the seventeenth century optical microscopes have been used to study the behavior of objects in fluidic environments. The awarding of the 2014 Nobel Prize in Chemistry to Eric Betzig, Stefan W. Hell and William E. Moerner "for the development of super-resolved fluorescence microscopy" has risen the awareness that optical imaging still is an active and important field of research. The overcoming of the Abbe diffraction limit is achieved by selectively switching the fluorescence of individual molecules on and off.

Despite the recent success of fluorescence microscopy, there are some fundamental short comings compared to pure scattering detection. The fluorophores suffer from photobleaching and they often have to be attached to an object of interest [47]. In the past two decades the sensitivity of fluorescent microscopy has been tremendously improved by using cameras which can detect almost every emitted photon and spectral filters which reduce the background noise to a minimum. However, the finite amount of photons a single fluorophore can emit prevents the long time recording with a high temporal resolution and good signal to noise ratio (SNR) [47].

In contrast to fluorescence, the amount of light, which is scattered by a small object, scales with the incoming light and is only limited by the heating due to absorption. Yet, scattering scales very unfavorably for small particles as $d^6$, where $d$ is the diameter of the particle. The scaling can be improved to $d^3$ by using a coherent light source and detecting the interference signal of light scattered by the particle and a reference plane. The group of Sandoghdar was the first who recognized the potential of this effect and promoted the detection technique under the name interferometric scattering detection (iSCAT) [48, 49]. They have demonstrated that the method can be used to detect not only nanoparticles but also single unlabelled viruses [49], molecules [50] and proteins [51] with kHz acquisition rates. The method has also been used to determine the size of nanoparticles and viruses [52], and to visualize the dynamics of the molecular motor myosin [53]. Furthermore, the phase of the interference signal provides an information on the path difference of the light originating from the particle and from the reference plane and thus yields information on its axial position [54, 55].

## 1.3 Thesis outline

In Chapter 2 the theoretical background for this thesis is reviewed. In the first part of this chapter equations are derived which are important for the stability, electrostatic trapping and assembly of colloidal particles. The second part focuses on the motion of particles under confinement.

The experimental setup, which was constructed and used to investigate the behavior of nanoparticles in a nanofluidic environment is presented in Chapter 3. In this chapter, both the fabrication of the confining surfaces is explained and the colloid used in most experiments is characterized e.g. the 60 nm gold spheres.

In Chapter 4 the methods to determine the separation of the confining walls and the vertical distance of the gold spheres to this walls are described. The technique is used to measure the gap distance dependent height distribution of the nanospheres in a nanofluidic slit consisting of either two silicon oxide surfaces or a polymer (PPA) and a glass surface.

The effect of confinement and surface roughness on the diffusion of the nanospheres in such an nanofluidic slit is investigated in Chapter 5. The motion of the spherical nanoparticles is directed in Chapter 6 by the realization of a rocking Brownian ratchet.

In Chapter 7 several types of nanoparticles are assembled by confinement dependent surface forces. The influence of these forces on the particles is investigated in detail for spherical gold nanoparticles, which are placed at predefined locations. Elongated nanorods are aligned by the shape of the guiding structures and the benefit of using a removable template is demonstrated by placing nanowires directly on prepatterned electrodes.

Chapter 8 concludes this thesis and provides an outlook on the future of transport, trapping and assembly of nanoparticles under confinement.

# 2 Theory

The aim of this chapter is to give a concise introduction to the behavior of nanoparticles in a nanofluidic environment. Therefore, the most relevant surface forces and transport phenomena are reviewed.

## 2.1 Surface forces and the stability of colloids

### 2.1.1 Van der Waals force

The Van der Waals force, named after the Dutch physicist Johannes Diderik van der Waals, is relatively weak compared to covalent bonds and ionic bonds. It is a dipole - dipole interaction, which means that the electric field of each dipole induces a preferential anti-parallel orientation of the other dipole. The Van der Waals interaction can be divided into three components [56]:

(i) Keesom interaction between two permanent dipoles,

(ii) Debye interaction between a permanent and an induced dipole,

(iii) London dispersion interaction between two induced dipoles.

The induced dipoles are caused by quantum mechanical fluctuations of the electron density distribution and are therefore present in every atom and molecule.

A macroscopic body, e.g. a colloid, consists of many atoms or molecules. According to the Hamaker approach the Van-der-Waals interaction energy per unit area between *two flat planes*, separated by the distance *d* is given by [56]

$$W_{PP}(d) = -\frac{A_H}{12\pi d^2}, \tag{2.1}$$

where $A_H$ is the Hamaker constant. The force between two spheres with the radii $a_1$ and $a_2$, separated by a small distance $d << a_1, a_2$, can be determined by the DERJAGUIN approximation [56]

$$F_{SS}(d) \approx 2\pi \frac{a_1 a_2}{a_1 + a_2} W_{PP}(d). \tag{2.2}$$

| | $A_H$ ($10^{-20}$ J) |
|---|---|
| $H_20$ | 3.7 |
| PPA | 6.2 |
| $SiO_2$ | 6.3 |
| Au | 40 |

TABLE 2.1: Most of the Hamaker constants are adapted from [56]. The Hamaker constant of PPA is determined by $A_H = 24\pi h_0^2\gamma$, where we assumed a center-to-center atom distance of $h_0 = 0.165\,\text{nm}$ and used a surfaces tension of $\gamma_{\text{PPA}} \approx 0.03\,\text{N/m}$ [59]. The Hamaker costant between two objects interacting across a third medium can be calculated with Equation 2.4. Thus, for a gold sphere separated by a water film from a silicon oxide surface we obtain $A_{\text{Au}-\text{H}_2\text{O}-\text{SiO}_2} \approx 4 \cdot 10^{-20}\,\text{J}$.

From the Equations (2.1) and (2.2) follows that the interaction energy between *two spheres* can be approximated for $d << a_1, a_2$ by

$$W_{SS}(d) \approx -\frac{A_H}{6d}\frac{a_1 a_2}{a_1 + a_2}. \tag{2.3}$$

The interaction between the objects is significantly longer-ranged than for the individual atoms, where the interaction energy decays with $1/d^6$. The Hamaker approach is to assume that the interaction energy between the atoms is non-retarded and pair-wise additive. However, pair-wise additivity ignores the influence of neighboring atoms, which is significant in media such as liquids [57]. Furthermore, due to retardation the dispersion interaction actually decays more rapidly at distances beyond about 5 nm, leading to weaker Van der Waals forces at larger separations.

The problem of additivity is avoided in the LIFSHITZ theory by treating the bodies as continuous media and deriving the forces in terms of the bulk properties such as dielectric constants and refractive indices. However, the Van-der-Waals interaction energy between two bodies still depends on the geometry of the examined problem as presented above. Only the Hamaker constant has to be to be calculated by the Lifshitz theory [57]. Tabulated values as well as information on how to calculate the non-retarded Hamaker constant for different media can be found in the literature [56, 58]. Table 2.1 summarizes the Hamaker constants for the most relevant materials within this thesis. The Hamaker constant between medium 1 and medium 3 interacting across medium 2 can be approximated by [56]

$$A_{123} \approx \left(\sqrt{A_1} - \sqrt{A_2}\right)\left(\sqrt{A_3} - \sqrt{A_2}\right). \tag{2.4}$$

If the Hamaker constants for both media 1 and 3 are either larger or smaller than of medium 2, the predicted combined Hamaker constant $A_{123}$ should be positive as seen from Equation 2.4. Thus, the Van der Waals force between two particles of the same material in a liquid suspension is always attractive. If there was only Van der Waals force, the dispersed particles would aggregate. However, aggregation can be prevented by longer-ranged repulsive electrostatic interaction [57].

### 2.1.2 Electrostatic interaction

Experiments show that surfaces in contact with water or any other liquid with a high dielectric constant usually develop a surface charge. Typically the charging of the surfaces is attributed to [56]

(i) the ionization of surface groups e.g. the dissociation of protons from surface silanol groups ($\mathrm{SiOH} \rightleftharpoons \mathrm{SiO^-} + \mathrm{H^+}$),

(ii) the adsorption (binding) of ions from solution onto the surface.

The degree of the dissociation depends on the ionic strength and $p$H of the bulk solution [60]. Both charging mechanisms can not change the charge neutrality of the enclosed system; hence, the final surface charge is balanced and screened by an equal but oppositely charged amount of counter-ions, which are arranged in a so called *electrical double layer*. Some of the counter-ions are firmly bound to the surface within the so-called Stern layer, while others are loosely bound within the *diffuse layer*. The Brownian motion of the counter-ions in the diffuse layer is affected by the diffuse layer potential, which can be described for a plane with the 1D POISSON equation [56]:

$$\frac{\mathrm{d}^2\psi_P(x)}{\mathrm{d}x^2} = -\frac{\rho(x)}{\epsilon\epsilon_0}, \tag{2.5}$$

where the $x$ coordinate is perpendicular to the plane, $\rho(x)$ represents the charge density, $\epsilon_0$ the permittivity of vacuum, $\epsilon$ the relative permittivity of the liquid and $\psi_P(x)$ the electric potential in dependence of distance $x$ from the Stern layer. Typically, the dissociated counter-ions are not the only ions in the solution. Due to auto-dissociation even "pure water" at $p$H 7 is an electrolyte containing $10^{-7}$ M (M = mol/l) of $\mathrm{H_3O^+}$ and $\mathrm{OH^-}$ ions. The net charge density is given by the distribution of counter-ions (ions of opposite charge to the surface charge) and co-ions, which follow the BOLTZMANN distribution

$$\rho(x) = -q_e \sum_i z_i \rho_{i,\infty} \mathrm{e}^{-z_i q_e \psi_P(x)/k_B T}, \tag{2.6}$$

where $q_e$ is the elementary charge, the valency $z_i$ can be either positive or negative and $\rho_{i,\infty}$ is the bulk ionic density of ion $i$, $k_B$ is the Boltzmann constant and $T$ (in K) is the absolute temperature.

The two fundamental Equations (2.5) and (2.6) can be expanded to higher dimensions yielding the 3D POISSON-BOLTZMANN (PB) equation, which can be simplified for a 1:1 electrolyte to

$$\nabla^2\psi = \kappa^2 \frac{k_B T}{q_e} \sinh\left(q_e\psi/k_B T\right), \tag{2.7}$$

where $\kappa^{-1}$ is the electrostatic screening length, called Debye length. The Debye length of a 1:1 electrolyte scales with

$$\kappa^{-1} = \sqrt{\frac{\epsilon\epsilon_0 k_B T}{2q_e^2 N_A c_\infty}} \approx 0.304\,[\mathrm{nm}]/\sqrt{c_\infty\,[1/\mathrm{M}]}. \tag{2.8}$$

where $N_A$ is the Avogadro constant and $c_\infty$ the bulk ionic concentration. In the regime of moderate surface charges, where the surface potential is $\psi < 25\,\mathrm{mV}$ ($e\psi/k_BT < 1$) the PB equation (2.7) can be linearized with a first order Taylor expansion; the result is known as the DEBYE-HÜCKEL (DH) approximation

$$\nabla^2\psi = \kappa^2\psi. \tag{2.9}$$

The solution of the PB equation for a plane $\psi_P(x)$ should not diverge for $x \to \infty$ and can be solved by an exponential decaying surface potential $\psi_{P,0}$:

$$\psi_P(x) = \psi_{P,0}\,\mathrm{e}^{-\kappa x}. \tag{2.10}$$

The Debye length $\kappa^{-1}$ can be tuned by the salt concentration as shown in Equation (2.8). Equation (2.10) reveals that the electrostatic potential becomes shorter ranged for a short debye length (i.e. high salt concentrations). The solution of the linearized PB equation for a spherical potential $\psi_S(x)$ is given by the screened Coulomb potential, also called Yukawa potential, as

$$\psi_S(r) = a\psi_{S,0}\,\frac{\mathrm{e}^{-\kappa(r-a)}}{r}, \tag{2.11}$$

where $a$ is the radius of the sphere and $\psi_{S,0}$ is the surface potential of the sphere. The solutions of linearized PB equation are good approximations at moderate surface charges ($\psi < 25\,\mathrm{mV}$) or at distances far away from the surface where the potential becomes smaller than $k_BT/e$. However, in order to match the solutions for the nonlinear conditions the surface potential for the plane $\psi_{P,0}$ and the sphere $\psi_{P,0}$ in Equation (2.10) and (2.11) have to be replaced by an "effective" surface potentials $\psi_{eff0}$, which can be determined from numerical solutions [61].

The effective spherical surface potential $\psi_{S,eff0}$ is obtained as [62]

$$\psi_{S,eff0} = \frac{k_\mathrm{B}T}{q_e} 8\tanh(\overline{\psi_{S,0}}/4)\left(1+\sqrt{1-\frac{2A+1}{(A+1)^2}\tanh(\overline{\psi_{S,0}}/4)^2}\right)^{-1}, \qquad (2.12)$$

using the dimensionless potential $\overline{\psi_{S,0}} = \psi_{S,0}q_e/k_\mathrm{B}T$ and a dimensionless particle radius $A = a\kappa$. For the isolated plane the effective potential $\psi_{P,eff0}$ can be obtained from Equation (2.12) for $A \to \infty$ and with the dimensionless plane potential $\overline{\psi_{P,0}} = \psi_{P,0}q_e/k_\mathrm{B}T$ as

$$\psi_{P,eff0} = \frac{k_\mathrm{B}T}{q_e} 4\tanh(\overline{\psi_{P,0}}/4). \qquad (2.13)$$

The combination of linearized PB equation ((2.10) and (2.11)) and rescaled effective surface potential (Equation (2.12) and (2.13)) deviates from the true solution of the full PB only by a few percent if $A > 0.1$ and $\psi_0 < 5k_BT/q_e$ ($\psi_0 < 125\,\mathrm{mV}$) [61].

The full and the linear PB equations (Equations (2.7) and (2.9)) estimate the electrostatic potential in solution caused by a charged sphere/plate and a redistribution of the co- and counter-ions. The distribution of the ions can be determined via the Boltzmann relation. The co-/counter-ions should rearrange themselves when a second charged object is placed close to this surface. The total interaction energy between the two entities is then given by a combination of the electrostatic and osmotic interaction. The linear superposition approximation (LSA) [60, 61, 63] simplifies this problem by assuming that the surfaces are sufficiently separated such that the influence of rearrangement is negligible. This means that the LSA approximation is strictly valid only for separations $x$ larger than the Debye length $\kappa^{-1}$ of the system; however, it has been shown that the errors at smaller separations are reasonably small [61].

For the linear regime, superposition holds and it can be assumed that the potential of a sphere is not affected by the potential of a nearby plane and vice versa. With the surface charge density $\sigma_S = \epsilon\epsilon_0 \frac{\kappa a+1}{a}\psi_{S,0}$ and the surface area of the sphere the interaction energy between a sphere and a plane is given for a 1:1 electrolyte by

$$W_{PS}(h) = 4\pi\epsilon\epsilon_0 a\psi_{S,0}\psi_{P,0}\mathrm{e}^{-\kappa(h-a)}. \qquad (2.14)$$

Figure 2.1 schematically depicts the situation where the sphere is now confined by two planes, which are separated by gap distance $d$. The distances between the surface of the sphere and the lower and upper confining plane are given by $x_L = d - h - a$ and $x_U = h - a$, respectively. The total interaction energy $W(d,h)_{PSP}$ is the sum of the two interaction energies between the sphere and

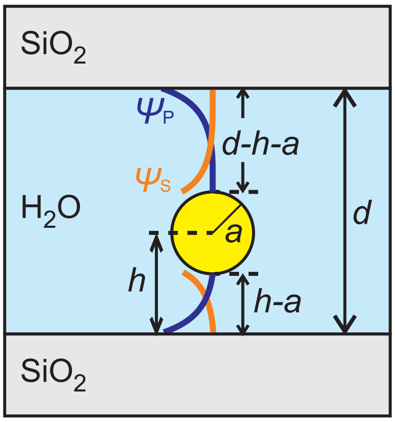

FIGURE 2.1: The linear superposition approximation (LSA) suggests that one can simply add (superpose) the potentials originating from the sphere $\psi_S$ and the plane $\psi_P$.

each plane

$$W_{PSP}(d,h) = W_{PS,eff0}\left(\mathrm{e}^{-(d-h-a)\kappa} + \mathrm{e}^{-(h-a)\kappa}\right). \tag{2.15}$$

with

$$W_{PS,eff0} = 4\pi\epsilon\epsilon_0 a\psi_{P,eff0}\psi_{S,eff0}. \tag{2.16}$$

The Equations (2.15) and (2.16) can be used to calculate the change in interaction energy for a charged particle confined by like charged surfaces at two different gap distances $d_1$ and $d_2$. It follows that the system gains potential energy when the particle moves from the smaller to the larger gap distance area $d_1 < d_2$. This can be easily seen for the case where the particle is located in the middle of the gap, i.e. $h = d/2$, then the difference in energy is approximately given by

$$W_{PSP}(d_2) - W_{PSP}(d_1) \underset{d_1<<d_2}{\approx} -2W_{PS,eff0}\mathrm{e}^{-(d_1/2-a)\kappa}, \tag{2.17}$$

which is always negative as long as the surface potentials of the plane and the sphere are like charged. However, to obtain an exact result for a complex geometry as depicted in Figure 2.2 one has to perform numerical simulations. Furthermore, at small separations the surface potential of a dissociated surface is also affected by the presence of an other potential, which is known as charge regulation.

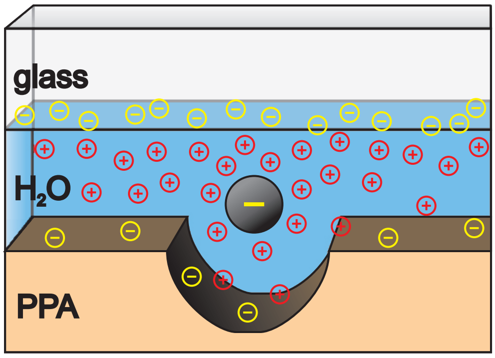

FIGURE 2.2: Schematic of a negative charged particle trapped by the electrostatic interaction above a recessed structure. The negative charge of the surfaces is screened by the the positive charged counter ions.

### 2.1.3 Derjaguin-Landau-Verwey-Overbeek (DLVO) theory

The DLVO theory is named after Boris Derjaguin and Lev Landau, Evert Verwey and Theodoor Overbeek. It is built on the assumption that the forces between two surfaces in a liquid can be regarded as the sum of Van der Waals and electrical double layer forces. The interaction energy between particles and surfaces can then be expressed as [56]

$$W(d) = W_{VdW}(d) + W_{edl}(d). \tag{2.18}$$

The Van der Walls force follows a power law and therefore it exceeds the finite double layer forces for small enough separations.

## 2.2 Transport of colloidal particles

### 2.2.1 Brownian Motion

The random movement of small particles in liquids and gases, which was discovered by the Scottish botanist Robert Brown in 1827, is called Brownian motion. It originates from collisions with atoms or molecules, which are excited to motion by heat.

In 1905 Einstein showed that the one-dimensional mean squared displacement (MSD) of such a particle in the $x$-direction and for a time interval $\Delta t$ can be expressed as [64]

$$\left\langle \Delta x^2(\Delta t) \right\rangle = \left\langle \frac{1}{N-1} \sum_{i=1}^{N-1} \left[x(t_i + \Delta t) - x(t_i)\right]^2 \right\rangle = 2D_0 \Delta t, \tag{2.19}$$

where $\langle ... \rangle$ signifies the ensemble average, $N$ is the number of observed positions per trajectory and $D_0$ is the diffusion coefficient. Furthermore, the bulk diffusion coefficient $D_0$ obeys the Stokes–Einstein equation

$$D_0 = \frac{k_B T}{6\pi\eta a}, \tag{2.20}$$

where $k_B$ is Boltzmann's constant, $T$ is the absolute temperature, and $\eta$ is the dynamic viscosity of the continuous medium. However, in many complex systems the diffusion does not show a linear dependence with $\Delta t$ and is often approximated by a power-law

$$\left\langle \Delta r^2(\Delta t) \right\rangle = 2nK_\alpha \Delta t^\alpha, \tag{2.21}$$

where $n$ indicates the number of spatial dimensions, $K_\alpha$ is a generalized diffusion coefficient and $\alpha$ is the anomalous diffusion exponent [65]. For $\alpha = 1$ the generalized diffusion coincides with the normal diffusion coefficient $D_0$ in Equation 2.19, but for $0 < \alpha < 1$ the diffusion is described as sub-diffusive and the diffusion coefficient becomes time dependent $D_{0,\alpha}(\Delta t) = K_\alpha \Delta t^{\alpha - 1}$.

### Confined lateral diffusion

The motion of a particle, which diffuses through a nanofluidic slit with two parallel plates, is hindered by hydrodynamical forces. Following the work of Eichmann *et al.* [66], we present the linear superposition (LSA) and the coherent superposition approximation (CSA) to calculate the hindered lateral diffusion in such a slit. A third approximation, the matched asymptotic expansion (MAE), is not considered here as it deviates only slightly from the LSA. The LSA presented here should not be confused with the LSA introduced to calculate the electrostatic interaction energy in Section 2.1.2.

The hydrodynamically hindered diffusion parallel to a single interface is conveniently given by a correction factor $f_{||1}$:

$$D_{||1}(h, a) = D_0 \, f_{||1}(h, a). \tag{2.22}$$

The correction factors are given in terms of the dimensionless particle height, $\omega = h/a$, for [67]

$$\begin{aligned}
&\omega > 1.1: \\
&f_{||1}(h,a) = 1 - \frac{9}{16}\omega^{-1} + \frac{1}{8}\omega^{-3} - \frac{45}{256}\omega^{-4} - \frac{1}{16}\omega^{-5} \\
&\qquad\qquad + 0.22206\omega^{-6} - 0.205216\omega^{-7} \qquad (2.23) \\
&\omega \leq 1.1: \\
&f_{||1}(h,a) = 1 - \frac{15/8}{\ln(\omega - 1)} \\
&\qquad\qquad + e^{1.80359(\omega-1)} + 0.319037(\omega - 1)^{0.2592} \qquad (2.24)
\end{aligned}$$

by Faxèn [68] and Goldman [69], respectively. A similar approach leads to the drag-reduced diffusion in a slit [70]:

$$D_{||2}\,(h,a,d) = D_0\, f_{||2}(h,a,d), \tag{2.25}$$

where $d$ is the gap distance of the confining walls. Oseen suggested the LSA[70]

$$f_{||2}^{\mathrm{LSA}}(h,a,d) = \left[f_{||1}(h,a)^{-1} + f_{||1}(d-h,a)^{-1} - 1\right]^{-1}, \tag{2.26}$$

where the drag of each wall is treated independently and the total force is given by the sum of the contributions.

Another expression, the CSA

$$\begin{aligned}
f_{||2}^{\mathrm{CSA}}(h,a,d) &= [1 + S_1 + S_2 - 2S_3]^{-1} \qquad (2.27) \\
S_1 &= \sum_{n=0}^{\infty} \left(f_{||1}(nd+h,a)^{-1} - 1\right) \\
S_2 &= \sum_{n=1}^{\infty} \left(f_{||1}(nd-h,a)^{-1} - 1\right) \\
S_3 &= \sum_{n=1}^{\infty} \left(f_{||1}(nd,a)^{-1} - 1\right)
\end{aligned}$$

includes multiple interactions from perturbations caused by pressure and velocity fields induced from each wall. The same interactions with the colloid are not included [71, 72].

### Rotational diffusion

It was Francis Perrin who first formulated the rotational diffusion about a single axis [73], the mean-square angular deviation for a time step $\Delta t$ is

$$\langle \alpha^2 \rangle = 2D_r \Delta t, \tag{2.28}$$

where $D_r$ is the rotational diffusion coefficient in radians$^2$/s. Also the rotational diffusion coefficient follows the Stokes-Einstein relation and for a sphere of radius $a$ it is given by

$$D_r = \frac{k_B T}{8\pi\eta a^3}. \tag{2.29}$$

The probability distribution of the orientation of a sphere decays with the first order of the spherical harmonics, the rotational relaxation time $\tau_r$ is thus given by

$$\tau_r = \frac{1}{2D_r}. \tag{2.30}$$

### 2.2.2 Brownian Motor

In this section we will show that the transport of the particles can be directed by breaking the symmetry of the potential landscape and adding non-equilibrium fluctuations [74]. Various models have been proposed that satisfy these requirements [75, 76].

One of these models is the “Rocking” Ratchet, which superposes the static sawtooth potential $W(x)$ with an externally unbiased fluctuating force $F$ [74, 75, 77] as depicted in Figure 2.3. The sawtooth potential can be described by an asymmetric triangular wave, e.g. the potential $W(x)$ shown in Figure 2.3 rises shallowly $\partial_x W_{\text{shallow}}$ and then falls steeply $\partial_x W_{\text{steep}}$. The rocking ratchet can be described as follows: (a) If no force is applied and the potential barrier height is larger than $> 5\,k_B T$, then the particles are trapped in the potential minimum. (b) If a fluctuating force $F \gtrsim \partial_x W_{\text{shallow}}$ is applied, the particles are capable of overcoming the restoring force of the shallow ramp. (c) If the same force is applied in the opposite direction and if this force is smaller then the restoring force of the steep ramp $|-F| \lesssim |\partial_x W_{\text{steep}}|$ then the event of particles moving backwards is still suppressed. Periodically switching between (b) and (c) leads to directed motion of the particles. The efficiency is strongly affected by the presence of thermal noise and depends on the amplitude and frequency of the periodic force $F$ and the barrier height. If the forcing is close to overcome the steep barrier the thermal noise reduces the efficiency, while for low and moderate forcing the temperature can increase the efficiency [74]. If the forcing is larger than the restoring force of

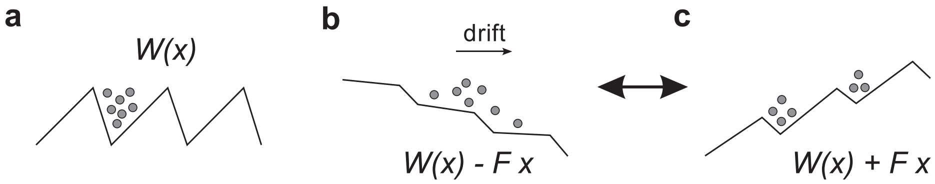

FIGURE 2.3: Schematic of the rocking Brownian ratchet. (a) Particles are trapped in an potential $W(x)$. (b) If a sufficiently high positive force is applied, the particles can overcome the potential barrier along the shallow slope, (c) while being blocked when the same force is applied in the opposite direction. Rocking the ratchet potential leads to directed motion.

the steep barrier the ratchet is overdriven; in this case the direction of motion can even be reversed simply by changing the applied frequency [78].

In contrast to Brownian motion, both the mean particle displacement $\langle \Delta x \rangle$ and the drift velocity $v$ of an ensemble of particles should not vanish in the case of directed motion. They are related by a time interval $\Delta t$ as

$$\langle \Delta x(\Delta t) \rangle = \left\langle \frac{1}{N-1} \sum_{i=1}^{N-1} \left[ x(t_i + \Delta t) - x(t_i) \right] \right\rangle = v \Delta t, \tag{2.31}$$

where $\langle ... \rangle$ signifies the ensemble average, $N$ is the number of observed positions per trajectory.

# 3 Experimental Setup

In the first section of this chapter, the nanofluidic confinement apparatus (NCA) is described. The NCA consists of two main components, the mechanical nanofluidic confinement and the optical detection setup, which are explained in Section 3.1.1 and Section 3.1.2, respectively. An overview of the control of the involved hardware is given in Section 3.1.3. Section 3.2 illustrates how the two confining walls of the NCA are fabricated and modified and it gives a description of the gold nanosphere colloid, which is used for most of the experiments.

Parts of this chapter have been adapted from the article "*In situ contrast calibration to determine the height of individual diffusing nanoparticles in a tunable confinement*" [79] written by me, Michael Skaug and Armin W. Knoll. The manuscript was published 2016 in *Journal of Applied Physics*. The mechanical part with the tunable confinement as well as the description of the cover-glass fabrication have been adapted from the article "*The Nanofluidic Confinement Apparatus: Studying confinement dependent nanoparticle behavior and diffusion*" by me, Felix Holzner and Armin W. Knoll. The manuscript is submitted to *The Journal of Chemical Physics*. For clarity some parts have been modified and written in a more general way to be valid for the entire thesis.

The design and setting up of the NCA was done by me. A first prototype of the setup already existed from Felix Holzner. Ute Drechsler, Steffen Reidt and Richard Stutz helped me with the fabrication of the cover-glass mesas. The evaporation of the metals for the electrodes was done by Meinrad Tschudy. The ellipsometry and Zeatasizer measurements were carried out by Marilyne Sousa and Songbo Ni, respectively.

## 3.1 Nanofluidic Confinement Apparatus

### 3.1.1 Tunable nanofluidic slit

A schematic of the cross section through the nanofluidic slit is shown in Figure 3.1 (a): A particle suspension is confined between the cover-glass (light gray)

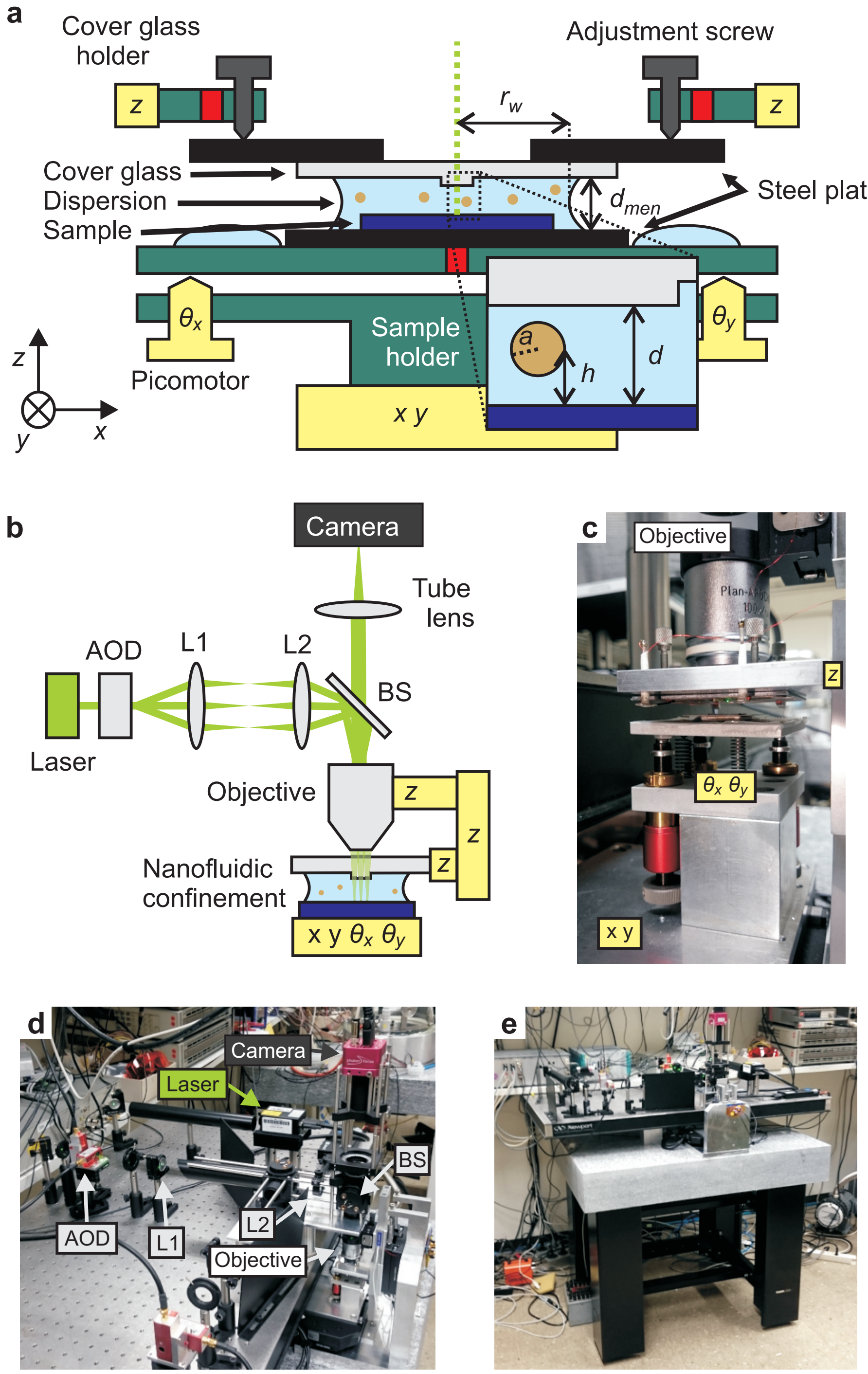

FIGURE 3.1: (a) Sketch of the vertical profile of the system, see text for details. The inset visualizes the nanofludic slit with gap distance $d$ confining a particle with radius $a$ at height $h$. (b) The optical setup consists of a laser, an acousto-optic deflector (AOD), and a telecentric system (L1 and L2) for scanned laser illumination of the sample through a beam splitter (BS) and an oil immersion objective with $\mathrm{NA} = 1.4$, $\mathrm{M} = 100x$. (c) Side view of the tunable confinement. (d,e) The detection setup is mounted above the nanofluidic slit on a breadboard, which sits on an active isolation frame.

and the sample (dark blue), which are glued with a cyanoacrylate adhesive to steel plates (black). Magnets (red) glued into aluminum holders (green) fix the position of the steel plates during an experiment. The magnetic fixation of the cover-glass allows to coarsely align the center of the mesa with respect to the optical axis of the objective (see Figure 3.1 (a,b)). Three adjustment screws are used to align the tilt of the cover-glass with respect to the focal plane of the objective and parallelization of the substrate to the cover-glass is done by three piezo linear actuators (Picomotor, Newport). The distance of the cover-glass and microscope objective relative to the substrate is controlled by two linear piezo-stages (100 $\mu$m, Nano-OP100, Mad City Labs) which are attached to a coarse positioning-stage (MT-84-50-LM, Feinmess Dresden GmbH).

A mesa is etched in the cover-glass such that the area outside the mesa is recessed by $\approx 50\,\mu$m (see Section 3.2.1). The mesa provides good optical access to the fluidic slit and ensures that the gap distance $d$ between the cover glass and sample (see inset of Figure 3.1 (a)) can be reduced until a colloid has intimate contact to both surfaces. At such a confinement only a few micro liters of a suspension are required and the surface area of the mesa $A_m \approx 0.02\,\mathrm{mm}^2$ is already much smaller than the wetted area of the cover-glass $A_w \approx 100\,\mathrm{mm}^2$. Thus the double layer repulsion and the Van der Waals attraction are negligible compared to surface tension forces that compress or extend the volume of water for a hydrophilic or hydrophobic surface, respectively. The Young-Laplace equation describes this so called capillary pressure, $\Delta p = \gamma \left( \frac{1}{R_1} + \frac{1}{R_2} \right)$, where $\gamma = 0.072\,\mathrm{N/m}$ is the surface tension of water and $R_1$ and $R_2$ are the principal radii of curvature. For small gap distances $d_{men}$ at the meniscus, the first principal radius can be approximated via the contact angle $\theta$ and the gap distance $R_1 \approx -\frac{d_{men}}{2\cos\theta}$ while the second is determined by the radius of the squeezed water drop $r_w$ (see Figure 3.1 (a)). For our nanofluidic slit the radius in the vertical plane is much smaller so that $\Delta p \approx \gamma \frac{1}{R_1} \approx -\gamma \left( \frac{2\cos\theta}{d_{men}} \right)$.

Typically, 20 – 30 $\mu$l of a colloid are used such that the suspension overflows the $\approx 1 \times 1\,\mathrm{cm}$ sized samples. Consequently, the distance at the meniscus $d_{men}$ is approximately $600\,\mu$m (sample thickness $550\,\mu$m), which results in a reduced Young-Laplace pressure and a higher stability of the system. A water reservoir next to the fluidic slit (Figure 3.1 (a)) reduces the evaporation of the droplet in the slit and enables a stable system for several hours.

The mechanically tunable confinement setup is mounted below the objective (see Figure 3.1 (c)), allowing for top-down illumination and imaging of the nanofluidic slit. The optical detection setup is mounted on a breadboard, which is jacked up by four aluminum blocks on a granite plate, as visualized in the photographs in Figure 3.1(d,e). In order to decouple the whole setup from mechanical vibrations the granite plate is mounted on an active isolation frame (Active Isolation, Thorlabs).

### 3.1.2 Interferometric Scattering Detection

A schematic illustration of a typical iSCAT setup [48, 49, 55] is sketched in Figure 3.1 (b). A continuous-wave laser (50 mW, $532.1 \pm 0.3$ nm, Samba, Cobolt) with a beam diameter of $\approx 0.7$ mm illuminates a selected sample area via raster scanning the focused laser beam by a two-axis acousto-optic deflector (AOD). Focusing and imaging are done using a 100x, 1.4 NA oil-immersion objective (Alpha Plan-Apochromat, Zeiss). A telecentric system consisting of two lenses with a focal distance of 15 cm, and a 50:50 beam splitter (10Q20BS.1, Newport) are used to image the AOD (DTSXY, AA Opto-Electronic) deflection plane onto the back focal plane of the objective. The reflected light is collected by the same objective and images are captured by a high frame rate camera (MV-D1024-160-CL-12, Photon Focus). Typically, the frame rate is limited by the data transfer for short exposure times $\tau_{\text{exp}}$. In order to achieve the maximal frame rate a small field of view is used which contains only the relevant features. If the sampling time is longer than the exposure time, a trigger delay $\tau_{\text{delay}}$ is needed to avoid frame drops. The total rate is given in frames per second $\text{FPS} = 1/(\tau_{\text{exp}} + \tau_{\text{delay}})$.

The deflection of the first order beam is caused by interaction of the laser beam with the acoustic wave inside the AOD. In order to generate an uniform illumination, the beam is scanned several times along the fast axis with a frequency of typically $100$ kHz. The slow axis is scanned with the same rate as the frames are acquired. The size of the illuminated area is limited by the maximum deflection angle of the AOD and the optical system e.g. $600 \times 600$ pixels, corresponding to an area of $65 \times 65\,\mu\text{m}^2$. The conversion factor of $0.108\,\mu$m per pixel has been measured with a calibration sample and is almost in exact agreement with the $10.6\,\mu$m pixel size and the 100x magnification of the objective.

During each image acquisition, the laser is typically raster scanned once along the slower y-axis to minimize the illumination time of the particles. The time a particle is illuminated can be estimated from the spot size of the laser and the spacing and duration of the faster scanned laser lines along the x-axis. The line scan duration $\tau_{\text{line}}$, the exposure time $\tau_{\text{exp}}$ and the length $y$ of slower axis determine the line spacing $\Delta y = y/(\tau_{\text{exp}}/\tau_{\text{line}})$. The time per line scan is typically $\tau_{\text{line}} = 10\,\mu$s. The laser beam diameter $w(z)$ can be estimated from the intensity distribution of a focused beam at the glass-air interface. A $1/\text{e}^2$ illumination spot size of $w \leq 2\,\mu$m is estimated from Gaussian fits to these intensity values at

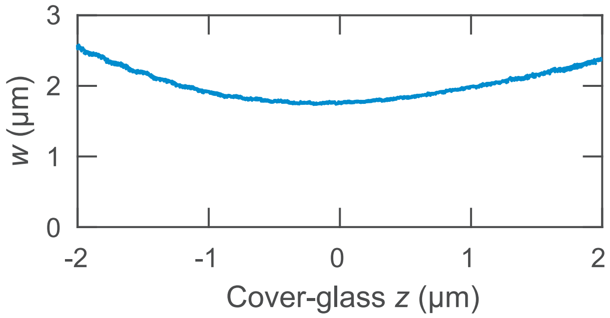

FIGURE 3.2: Diameter of the laser beam reflected at glass-air interface for various axial positions of the cover-glass.

various cover-glass positions (see Figure 3.2). The illumination time of a single scanned point can be approximated by $\tau_{\text{illu}} \approx \tau_{\text{line}}\, w/\Delta y$. For an even illumination the line spacing has to be smaller than the spot size of the Gaussian beam. Typically, the line spacing is $\lesssim 500\, nm$, which corresponds to an illumination time of $\tau_{\text{illu}} \gtrsim 40\, \mu\text{s}$. During $\tau_{\text{illu}}$ the diffusion of a e.g. 60 nm nanosphere (bulk diffusivity $D_p \approx 7 \mu\text{m}^2\text{s}^{-1}$) in one dimension is $\lesssim \sqrt{2 D_p \tau_{\text{illu}}} \approx 25\,\text{nm}$, which is small compared to the laser line spacing. Thus the image taken by the camera contains information about the position of the particle averaged over a duration of $\lesssim \tau_{\text{illu}}$.

Raster scanning the laser multiple times during the exposure of each image increases the illumination time but also reduces the background noise. In this case the illumination time is given by $\tau_{\text{illu}} = (\tau_{\text{exp}} + \tau_{\text{delay}})(\text{N}_{\text{scan}} - 1)/\text{N}_{\text{scan}}$, where $\text{N}_{\text{scan}} > 1$ is the number of scans [55].

### 3.1.3 Controlling the apparatus

The schematic in Figure 3.3 illustrates how the hardware of the setup is controlled. The definition of parameters, activation of processes and data recording is controlled and visualized with Matlab (Matlab R2014b, MathWorks). Some parameter changes e.g. the exposure time, trigger delay or targeted positions of the linear piezo stages are transmitted to an ADwin real-time system (ADwin Pro, Jäger GmbH). The system takes care that the illumination of the sample and the capturing of frames are synchronized and that the stepping of the piezo motors is done between the frames.

A 5 V trigger signal from the ADwin starts the recording of each frame on the camera. The camera is operated in a simultaneous readout mode, which means that a previous frame is captured by the frame grabber from the camera while a current frame is exposed. The images and their intrinsic time stamp are either

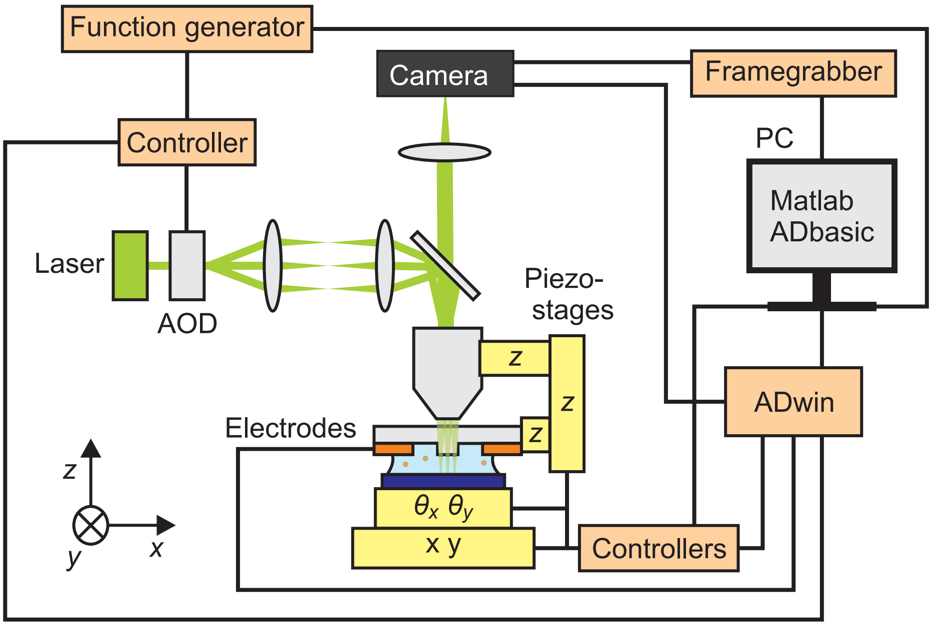

FIGURE 3.3: Schematic of the wiring and control of the setup. The details are described in the text.

written directly to a SSD drive or into the memory of the PC. The Matlab software extracts particular images with a frequency of 20 Hz and visualizes them in a live view at any time. The ADwin also triggers an arbitrary function generator (AFG3052C, Tektronix), which generates a $0 - 10\,\mathrm{V}$ sawtooth signal. The waveforms are used as inputs for the RF driver of the AODs. The waveform linearly and continuously sets the frequency of the RF output signal, which generates and modulates an acoustic wave in the AOD and thus deflects the beam. The size and position of the illuminated area is given by the amplitude and offset of the sawtooth signal, which are set by Matlab through a GPIB connection to the function generator. The intensity of the deflected beam is also set by RF output signal, which is controlled by a $0 - 5\,\mathrm{V}$ analog signal from the ADwin. Since the input impedance of the RF driver for the analog signal is $50\,\Omega$ a custom made current amplifier is used to deliver the high load.

The ADwin system runs an ADbasic program, which not only creates the trigger signal but also updates the 0–10 V input signal of the linear piezo-stage controller with the same frequency. Thus by changing the respective ADwin parameters the positions of the attached cover-glass and objective are set before the next frame is acquired. At the same time, the ADwin system can apply a potential of 0–10 V between two electrodes across the glass mesa. During an experiment the Adwin records all operated positions, applied voltages and the time of each event. Matlab captures and saves this data after the experiment. This allows to link the recorded frames with the piezo positions and the applied electrode voltages for further data analysis.

## 3.2 Sample preparation

The tunable nanofluidic slit consists of two confining walls. The upper wall is a modified cover-glass, where large parts of one surface are recessed and only a central area of the original surface is remaining. This glass mesa reduces the risk that surface impurities such as dust particles, deposited aggregates or a small tilt of the two walls hinder the approach of the two surfaces and it also allows to incorporate electrodes. The fabrication of this glass mesa is illustrated in Section 3.2.1.

The other surface is typically defined by a piece of a silicon wafer, which for most experiments is covered with a thermally responsive polyphthalaldehyde polymer (PPA). The patterning technique of this polymer film based on an AFM is described in Section 3.2.2.

### 3.2.1 Cover-glass

The fabrication process of the cover-glass mesa and electrodes is illustrated in Figure 3.4 (a-f) and consists of the following steps:

(a) First, the cover-glass glass (D263T borosilicate, UQG) was cleaned in a piranha solution ($H_2SO_4$:$H_2O_2$ 3:1) for 5 min.

(b) Layers of 30 nm Cr and 300 nm Au were sputtered onto the glass to avoid pin holes during the glass etching. A photoresist (AZ4533, MicroChemicals) was spin coated on top at 4000 rpm resulting in a 3 $\mu$m thick layer. In order to remove the remaining solvent a softbake was done at 110°C for 1 min.

(c) Parts of the resist were illuminated by UV light through a photomask and the exposed areas were removed in a diluted 3:1 developer (AZ400K, MicroChemicals) within $\approx 40$ s.

(d) A hardbake was performed at 160°C for 10 min to increase the stability of the resist. The metal layers were removed at the unprotected areas by wet etching (TechniEtch ACI2, MicroChemicals and TechniStrip Cr01, MicroChemicals) leaving behind a central metal-resist stack, which defined the position of the mesa. The area around the stack was etched for 75 s by concentrated hydrofluoric acid (49 % HF) to define the mesa. A mesa height

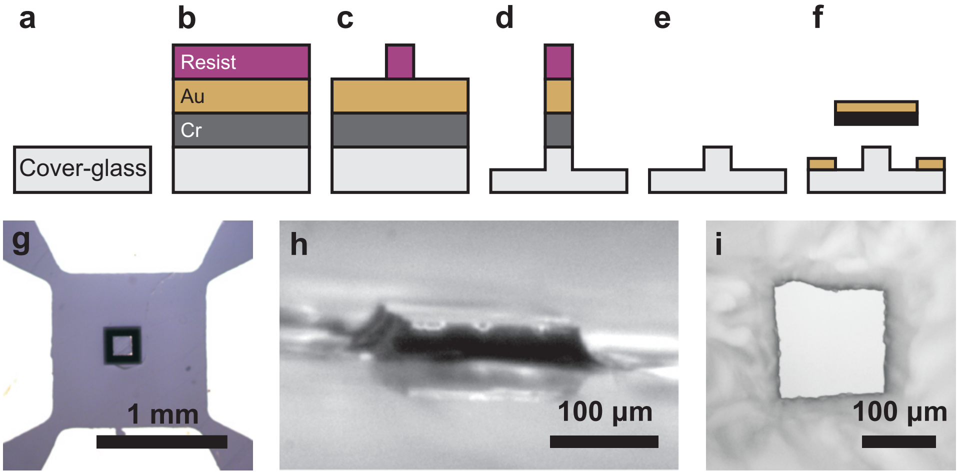

FIGURE 3.4: (a-e) The cover-glass mesa is fabricated by the following process steps: (b) Deposition of a Cr-Au hard mask and spin coating of a photoresist (c) Photolithography of the resist (d) Wet echting of the hard mask and cover-glass (e). (f) Removal of masking layer (f) Electrodes are patterned by evaporation through a shadow-mask. (g-i) Optical micrographs of a processed cover-glass. (g) Four electrodes are patterned around the central mesa. (h) Side and (i) top view of the glass mesa.

of 40-45 $\mu$m was measured with a profilometer (Dektak, Veeco). This corresponds to an etch rate of $\approx 36\,\mu$m/min, which was also observed by Zhu et al. [80]. The backside of the cover-glass was protected from HF by attaching this side with wax to a silicon wafer.

(e) The mesa was fabricated after removing the remaining masking layer by etching and the wax by a solvent (NMP, MicroChemicals).

(f) The electrodes were patterned by evaporating a 5 nm Cr layer, acting as adhesion promoter, and a 50 nm Au layer through a shadow-mask made from a 200 $\mu$m steel plate by laser cutting (1.4310, Lasercut).

Before usage the etched cover-glass is cleaned with a peel off polymer (Red First Contact, Photonic Cleaning Technologies) and for 20 s with either a helium plasma (Piezobrush, Relyon Plasma) or a oxygen and hydragon (5% $H_2$, 95% Ar) plasma at 200 W (GigaEtch 100-E, PVA TePla GmbH) and subsequently rinsed with deionized water.

The topographical surface quality of a cover-glass after cleaning is depicted in the atomic force microscope (AFM) image in Figure 3.5 (a). Figure 3.5 (b) shows an AFM image of the surface of the glass-mesa after the fabrication process. Besides small residues, the topography is almost not altered. The AFM measurements yield a root-mean-square (RMS) roughness of $S_q^{D263} = 0.26$ for the unprocessed cover-glass and $S_q^{mesa} = 0.39$ after the fabrication.

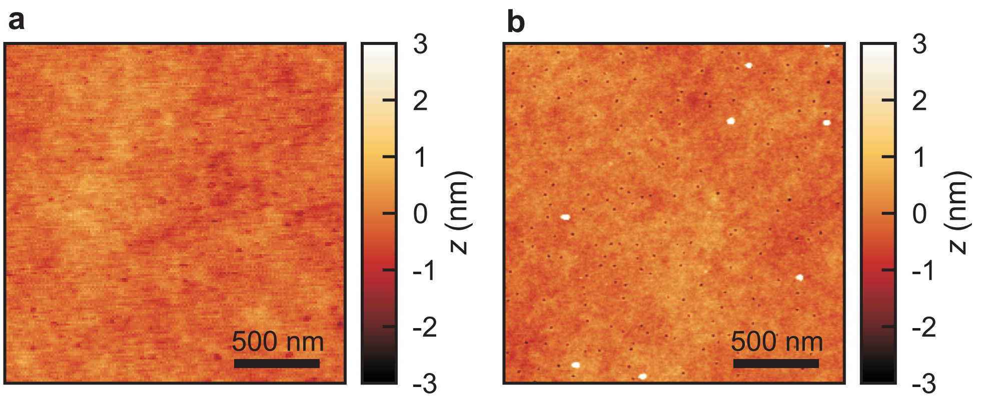

FIGURE 3.5: (a,b) AFM micrograph of a cleaned cover-glass (a) before and (b) after fabrication of a glass mesa.

### 3.2.2 Thermal Scanning Probe Lithography

Thermal Scanning Probe Lithography (tSPL) is an AFM based patterning technique, which has been developed at IBM Research - Zurich. The method uses heated tips to locally decompose and evaporate organic resists such such as molecular glass [83] or a thermally responsive polyphthalaldehyde polymer (PPA) [84]. The tip is heated by a resistive element, a low doped region of the silicon cantilever as visualized by the schematic in Figure 3.6 (a). By controlling the position of the tip arbitrary shapes can be carved out of the PPA film. The vertical position of the tip is controlled by an electric potential between the tip and the sample. The resulting attractive force is proportional to the patterning depth such that a 3D profile can be created in a single patterning run. The result of a written line can be inspected *in-situ* during the retrace motion of the cold tip in contact mode as depicted in Figure 3.6 (b). In contact the distance of the cantilever to the unpatterned polymer film is given by the length of the tip and depth of the written structure. This cantilever-polymer distance is measured by another micro-heater located in one of the side arms. The reading-heater is operated at a constant voltage. The closer the cantilever is to the substrate the more the reading-heater is cooled, which affects its resistance. Thus a height dependent temperature difference can be sensed with Angstrom precision by measuring the electric current [82]. The reference height of the unpatterned polymer film is measured at positions before and after the patterned 3D profile.

The cone shape of the cantilever tip is depicted in the SEM image in Figure 3.6 (c). The tips have a typical length of $500 - 700\,\mathrm{nm}$ with a tip radius of $5 \pm 2\,\mathrm{nm}$ [82],

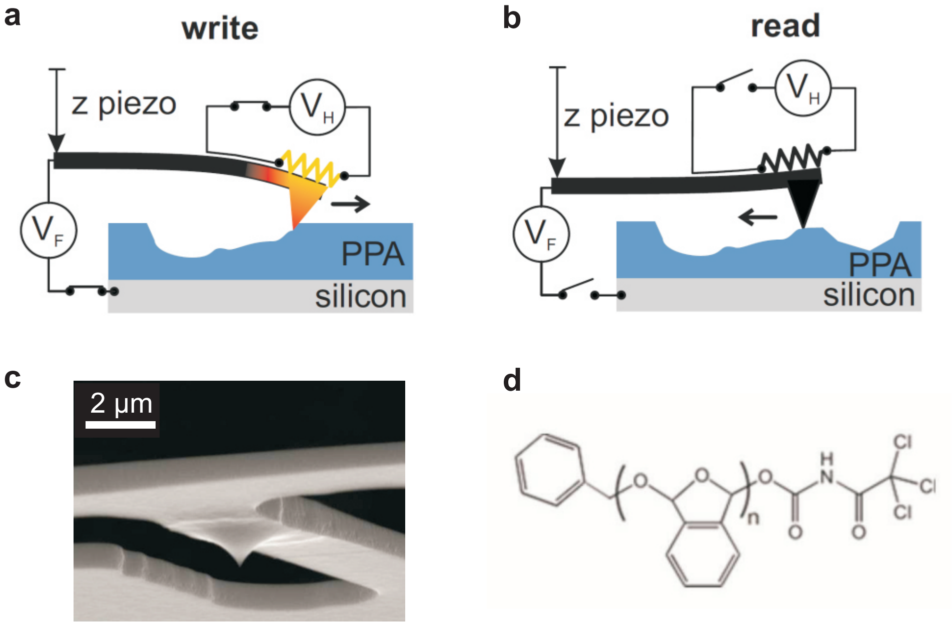

FIGURE 3.6: 3D patterning by tSPL. (a) Writing is done by applying an electric potential to a resistive region above the tip in the cantilever. The thus heated tip is pulled into contact by a voltage pulse $V_F$ at each write pixel location. The applied force is proportional to the patterning depth into the PPA. Adapted from [81]. (b) Reading is done by bringing the tip into contact with the patterned topography by a piezo. The written depth into the polymer film is measured by another micro-heater. The temperature of the tip in this mode is below the decomposition temperature of the PPA. Adapted from [81]. (c) SEM image of the tip below the mirco-heater. Adaped from [82]. (d) Molecular structure of the thermally responsive polyphthalaldehyde polymer (PPA). Adapted from [82].

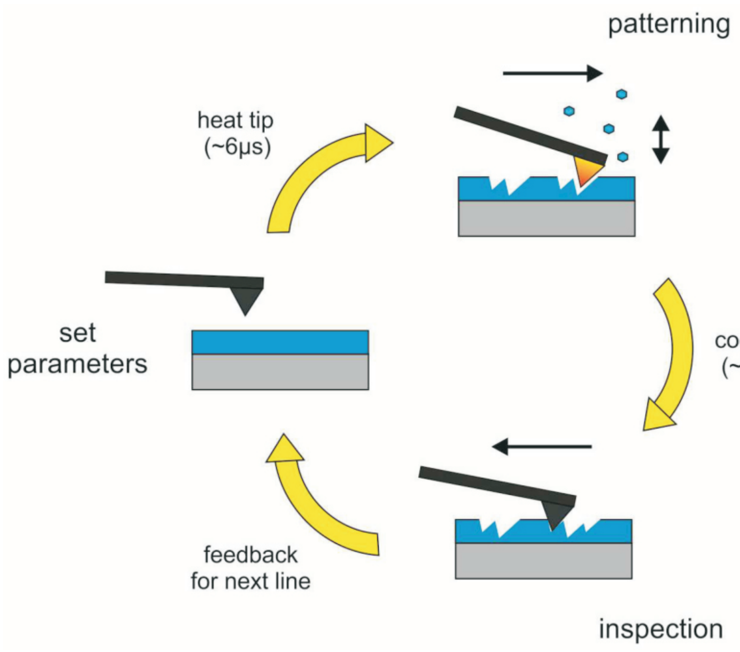

FIGURE 3.7: A cloosed-loop feedback is used to adjust the parameters such as temperature and applied force to compensate static errors. Starting with initial parameters a target 3D profile is written. After the tip is cooled down, the patterned profile is read back during the retrace. For each pixel the written and target pattern are compared. Depending on the deviation between both patterns the parameters are optimized for the next line. Adapted from [82].

which determines the dimension of the smallest void in the PPA film. The chemical structure of PPA, a so called SAD-polymer (Self-Amplified Depolymerization), is depicted in Figure 3.6 (d). A thermally triggered reaction leads to endothermic unzipping of the polymer chain into volatile monomers [82, 84].

The capability to write and investigate the 3D profile for each line allows the implementation of a cloosed-loop feedback which is illustrated in Figure 3.7. The first set of trial parameters such as temperature, force and pulse duration are defined by a static approach of the tip to the polymer. These parameters are used to write the first line of the pattern with a heated tip. Then, the tip turns around and cools down to room temperature. During the retrace motion the written topography is sampled by the tip. In case the deviation of the written and target pattern is above a certain threshold the parameters for writing the next line are optimized based on a Kalman algorithm [81].

The patterned sample can now be used in the nanofluidic confinement apparatus. We found that a PPA film spin coated on the native oxide of a silicon wafer gets undermined by water and forms small bubbles. This can be prevented by either dipping the silicon in HF before spin coating or by using a cross linking

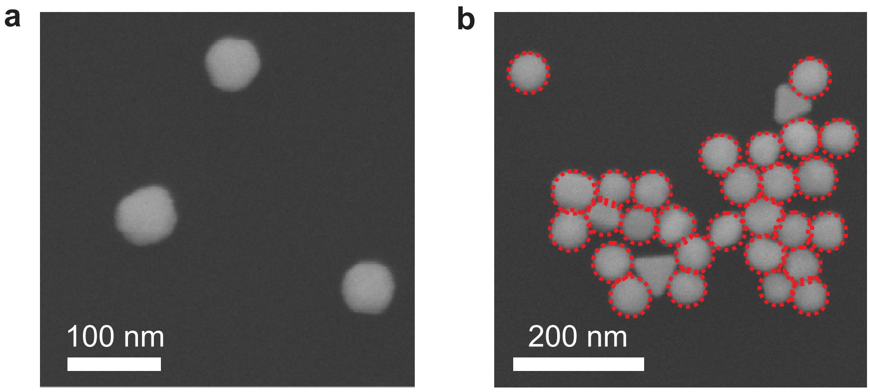

FIGURE 3.8: SEM images of deposited 60 nm Au nanoparticles. The average diameter of the spheres (red dashed lines) is $2a = 58.6 \pm 6.2$ nm.

polymer (HM8006, JSR) as a adhesion promoter. For most experiments a 52 nm thick HM film was spin coated onto a silicon sample. The thickness of the subsequent spin coated PPA layer was adjusted to meet the required optical path length for an optimal particle contrast. The thicknesses of both films were measured with an AFM. The refractive indices $n_{HM} = 1.67$ and $n_{PPA} = 1.59$ at 532 nm, were determined by ellipsometry. All four parameters are necessary to describe the optical response of the substrate (see Section 4.7).

### 3.2.3 Gold nanosphere colloid

The particle system chosen for most of the studies within this thesis is a colloid of citrate stabilized 60 nm Au nanospheres (BBI Solutions). There are three reasons for choosing this system for most of our measurements. First, the enhanced scattering cross section for light which couples to the surface plasmons of each particle. Second, the pure charge stabilization of the colloid, due to the negative surface charge of the citrate anions. Third, the relative low size and shape variation as shown in the exemplary SEM images in Figure 3.8. The nominal 60 nm gold spheres have been immobilized by droplet drying.

The manufacturer uses the Turkevich Method[85] for synthesis of the gold colloid. This standard method is based on the reduction of a chloroauric acid ($HAuCl_4$) with sodium citrate ($Na_3Cit$) in a aqueous solution at 100 °C [86]. The chloroauric acid solution is boiled and the added amount of preheated citrate solution determines the size distribution of the colloid [86]. The average particle diameter $2a$ and the particle density of the nominal 60 nm Au nanospheres is given in Table 3.1.

| | BBI | SEM | ZS (1:150) |
|---|---|---|---|
| $2a$ (nm) | $59.8 \pm 4.8$ | $58.6 \pm 6.2$ | 62.1 |
| $N_p$ (ml$^{-1}$) | $2.6 \times 10^{12}$ | | |
| $\zeta$ (mV) | | | -57.5 |
| $L$ ($\mu$Scm$^{-1}$) | | | 11.5 |
| pH | | | $6.8 \pm 0.2$ |

TABLE 3.1: The physical diameter $2a$ of the nominal 60 nm Au particles is given as specified by manufacturer (BBI) and measured by SEM. The number of particles $N_p$ is specified for the undiluted colloid. For measurements with the Zetasizer (ZS) the colloid was diluted 1:150 with ultrapure water (Millipore, $18.2\,\mathrm{M\Omega cm}$) to measure the hydrodynamic diameter $2a$, the zeta potential $\zeta$ and the specific conductance $L$. The pH was measured with a pH paper stripe.

The gold particles acquire a negative charge due to strongly adsorbed citrate ions, which is balanced by loosely bound sodium cations [87]. The screening of the surface potential, the Debye length is measured with a Zetasizer (Zetasizer Nano, Malvern Instruments). The apparatus calculates the zeta potential from the colloid's electrophoretic mobility, which can be determined by utilizing the Doppler effect of charged particles moving in an electric field. A laser beam scattered by the moving particles experiences a small shift in frequency, which can be measured as phase shift by superposition with a reference beam. The particles are typically measured in closed cells, where dissociation of surface ions leads to a charging of walls and mobile counter ions. The applied electric field induces a force on the particles but also on the ions in the solution, which leads to an electroosmotic flow of the liquid. To decouple the influence of the electroosmotic drag from the particle electrophoresis, either a clever measurement design or a independent measurement of both contributions is needed. The measured zeta potential as well as the specific conductance for a diluted colloid is given in Table 3.1.

The decay length of the zeta potential into the dispersion medium is characterized by the Debye length $\kappa^{-1}$, which can be determined by conductance measurements. Strong electrolytes completely dissociate in an aqueous solution [88]. The molar conductance $\Lambda_m$ of such a electrolyte follows the Kohlrausch's Law

$$\Lambda_m = \Lambda_m^0 - S\sqrt{c} \tag{3.1}$$

where $\Lambda_m^0$ is the limiting molar conductance, $S$ a constant and $c$ the molar concentration of molecule $m$. At sufficiently low concentrations the specific conductance $L$ becomes directly proportional to the concentration

$$L = \Lambda_m^0 c - S c^{3/2} \underset{c\to 0}{\approx} \Lambda_m^0 c. \tag{3.2}$$

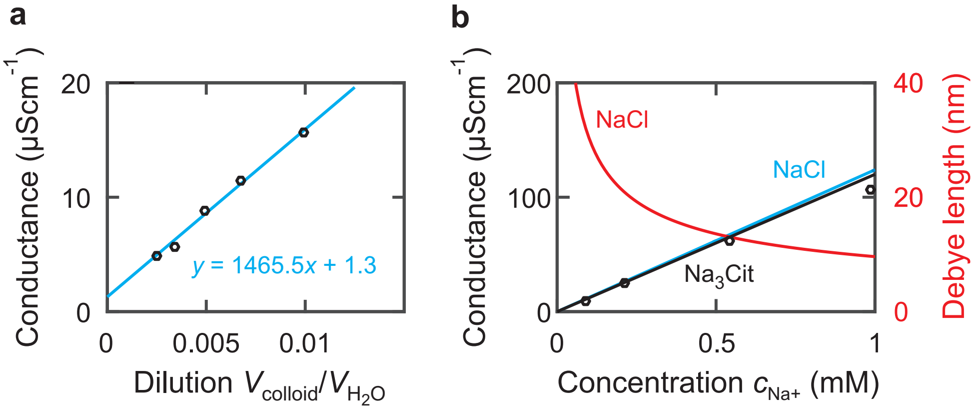

FIGURE 3.9: (a) The measured specific conductance $L$ of a citrate stabilized 60 nm Au colloid for different degrees of dilution (black circles) and a linear fit to the data. (b) The linear dependency of the conductance of sodium chloride (Equation (3.7)) and sodium citrate (Equation (3.8)) for low ionic concentration is depicted by the blue and black line, respectively. The approximations are in good agreement with experimental measured values, which are taken from literature [88]. Please note that the conductance is given in dependence of the cation concentration $c_{Na^+}$. The red line depicts the Debye length as a function of ionic concentration for a monovalent electrolyte.

Figure 3.9 (a) shows the measured conductance $L$ of the citrate stabilized 60 nm Au colloid for various degrees of dilution and a linear fit to the data. Due to the linear dependence we conclude that the electrolyte is dominated by the strong electrolytes sodium citrate and sodium chloride, which can be both present due to the reduction of chloroauric acid ($HAuCl_4$) by sodium citrate ($Na_3Cit$). The specific conductance $L$ is given by the sum of the ionic contributions

$$L = \frac{1}{1000} \sum_{j=1}^{n} |z_j| c_j \lambda_j . \tag{3.3}$$

The limiting conductances of sodium [88], citrate [88] and chlorine [89] are

$$\begin{aligned}
\lambda^0_{Na^+} &= 50.2\,\mathrm{Scm^2mol^{-1}}, & (3.4)\\
\lambda^0_{1/3Cit^{3-}} &= 72.2\,\mathrm{Scm^2mol^{-1}} \text{ and} & (3.5)\\
\lambda^0_{Cl^-} &= 76.4\,\mathrm{Scm^2mol^{-1}}. & (3.6)
\end{aligned}$$

Inserting these values in Equations (3.2) and (3.3) yields the specific conductance $L$ in dependence of a low counter-ion concentration ($c_{Na^+} << 1\,M$)

$$\begin{aligned}
L_{NaCl} &\approx (\lambda^0_{Na^+} + \lambda^0_{Cl^-})\, c_{Na^+} = 126.6\, c_{Na^+}\ \mu\mathrm{Scm^{-1}} & (3.7)\\
L_{Na_3Cit} &\approx (\lambda^0_{Na^+} + 3\,\frac{1}{3}\,\lambda^0_{1/3Cit^{3-}})\, c_{Na^+} = 122.2\, c_{Na^+}\ \mu\mathrm{Scm^{-1}}, & (3.8)
\end{aligned}$$

| Section | Experiment | Dilution | $\kappa_{\text{dilu}}^{-1}$ (nm) | $\kappa_{\text{exp}}^{-1}$ (nm) |
|---|---|---|---|---|
| 4.6 | height ($SiO_2$ - $SiO_2$) | 1:30 | 15.3 | 23.4 |
| 4.7 | height (D263 - PPA) | 1:10 | 8.9 | |
| 5.3 | diffusion | 1:10 | 8.9 | |
| 6.2 | ratchet | 1:18 | 11.9 | 13.5 (18.0) |
| 7.2 | assembly | 1:20 | 12.5 | (20.8) |

TABLE 3.2: Diluted Au 60 nm : $H_2O$ colloids were used in this thesis and the degree of dilution is used to estimate the Debye length $\kappa_{\text{dilu}}^{-1}$. In some experiments the Debye length $\kappa_{\text{exp}}^{-1}$ was also measured by an independent method. For the ratchet experiment two values are given, in brackets is the determined value, by assuming a particle position in thermal equilibrium. Numerical simulations have shown that this model is to simple and would provide a 25% to large Debye length (see Section 6.2.1). The value for the assembly experiment is determined by the decay of the trapping stiffness (see Section 7.2.2).

where $c_{Na^+}$ is in the units of $mM$. Figure 3.9 (b) shows the specific conductance for both electrolytes as well as measured conductance values for sodium citrate, which are taken from literature [88]. Both electrolytes scale almost equally with the cation concentration. However, the Debye length scales with the ionic strength $I = 1/2\sum_{i=1}^{n} c_i z_i^2$ given in the units of mM as

$$\kappa^{-1} = 9.6\,[\text{nm}]/\sqrt{I\,[1/\text{mM}]}. \tag{3.9}$$

The ionic strength for a 1:1 (1:3) electrolyte is $I = c$ ($I = 6c$) and the relation between concentration of added salt, cations and anions is given by $c = c_+ = c_-$ ($c = 1/3\,c_+ = c_{3-}$). This means that the ionic strength in dependence of the cation concentration $c_+$ is for 1:3 electrolyte double as strong as for an 1:1 electrolyte. Nevertheless, it is known that the negative charge of the gold particles arises from the adsorption of citrate ions [87]. We estimate the upper limit of the Debye length by assuming that the remaining electrolyte is dominated by the monovalent NaCl ions. At all events, this yields only a $\sqrt{2}$ larger Debye length compared to the case where all anions of the electrolyte are citrate ions.

For several experiments the colloid was diluted with ultrapure water (Millipore, $18.2\,\text{M}\Omega\text{cm}$) to reduce the ion concentration and obtain a particle density that was suitable for tracking. Table 3.2 summarizes the used dilutions and the Debye length calculated as described above.

### Plasmon heating

The wavelength of the laser (532 nm) used to illuminate the 60 nm gold spheres was close to the plasmon resonance of the particles, which lead to a large scattering cross section and thus provided a good contrast for imaging. However, the oscillation of the surface electrons also generated heat due to electron-phonon interactions. The temperature distribution around an optically excited nanoparticle can be described by a heat transfer equation. The details of the derivation can be found in literature [90, 91]. Here, we just like to mention that the size dependence of the temperature increase is governed by the total rate of generated heat and by the transfer of heat through the surface of the sphere. Consequently, the maximum temperature increase is proportional to

$$\Delta T_{max} \propto I_0 a^2, \tag{3.10}$$

where $I_0$ is the light flux and $a$ is the radius of the sphere. In our illumination setup we used a 50 mW laser; however, the AOD was typically operated in a regime where only a few percent of the intensity were deflected and used to illuminate a sample area of at least $20 \times 20\,\mu\mathrm{m}^2$. Also the optical elements in the light path e.g. the two lenses and the beamsplitter reduced the intensity, therefore we measured the power just before the light entered the objective. A power of less than $< 200\,\mu$W was measured at this position with a power meter (LaserCheck, Coherent). Consequently, a resulting light flux of less than $\leq 50\,\mathrm{W/cm}^2$ illuminated the 60 nm gold spheres, which resulted in a temperature increase of the particle surfaces well below $\Delta T_{max} < 0.1\,\mathrm{K}$ [91].

# 4 Method: Interferometry

In this chapter, a model is presented that allows both the determination of the gap distance in the nanofluidic slit and of the height of the particles. Based on the principle of interferometry information about the optical path length is gained from the sinusoidal background and particle signal.

The results of this chapter have been published in the article "*In situ contrast calibration to determine the height of individual diffusing nanoparticles in a tunable confinement*" [79] written by me, Michael Skaug and Armin W. Knoll. The manuscript was published 2016 in *Journal of Applied Physics*. The determination of the particle height above a film of PPA has been adapted from the article "*The Nanofluidic Confinement Apparatus: Studying confinement dependent nanoparticle behavior and diffusion*" [92] by me, Felix Holzner and Armin W. Knoll. The manuscript is submitted to *The Journal of Chemical Physics*. For clarity some parts have been modified and written in a more general way to be valid for the entire thesis.

The optical model described in this work has been developed by Armin Knoll and me. The evaporation of the $SiO_2$ was done by Meinrad Tschudy. The ellipsometry measurements were carried out by Marilyne Sousa. Most of the manuscript was written by me and Armin Knoll. A significant part of the introduction was written by Michael Skaug and he also revised the manuscript. Proofs-reading of the manuscript was done by Charlotte Bolliger and Michael Skaug. Madhavi Krishnan contributed with fruitful discussions.

## 4.1 Introduction

Optical detection techniques which are capable of tracking the 3D position of nano-objects are important to study the behavior of nanoparticles and molecules in nanofluidics [93], biological systems [94], porous materials [95] and confined reactions [96]. A variety of methods has been developed to track the 3D position of nanoparticles or molecules. Widefield methods, such as point-spread function engineering [97–99], holographic imaging [100], astigmatic imaging [101–103], total internal reflection microscopy (TIRM) [66, 104, 105], off-focus detection [106] and multifocal-plane detection [107–109], provide high-resolution 3D position detection. Most of these techniques are capable of tracking nanoparticles over the distance of several microns, only for TIRM the imaging range is restricted to a few hundred nanometers, due to the exponential decay of the evanescent field. Furthermore, lateral and axial localization accuracies below 10 nm are reported for most of these works. However, this is only achieved with long exposure times, which results in the acquisition of averaged and blurred particle images. Here, TRIM seems to have an advantage, due to the good background signal suppression sub microsecond exposure times have been reported [105]. The last parameter which is essential to resolve the dynamics of nanoparticles and molecules in fluidic environments is the maximum acquisition frame rate. Yet, due to photobleaching or the low signal from pure scattering the methods mentioned above seem to be not capable of resolving the motion of nanoparticles or molecules with acquisition rates well above 30 frames per second. In this regard the high sensitivity of the interference signal described in Section 1.2 provides a clear advantage. Krishnan *et al.* have measured the 3D positions of nano-objects with high spatial resolution and 1000 frames per second. They have demonstrated that the optical particle contrast can be calibrated by obtaining average intensity values of particles sticking to interfaces at known heights [54, 55]. The mean contrast of single trapped particles is then used to adapt this intensity scale to the individual particle level [55].

In this chapter we calibrate the contrast of individual nanoparticles *in-situ*. Our experimental NCA setup combines tunable confinement with iSCAT imaging. It allows us to track the three-dimensional position of single diffusing 60 nm gold nano-spheres with short illumination times.

In Sections 4.2 - 4.4 we provide a method to calculate how much light the multilayered nanofluidic slit reflects and the method is used to determine the separation of the confining surfaces. Section 4.5 describes how the images are processed in order to identify and track the nanoparticles. In Section 4.6, we develop a three-parameter optical model which describes the iSCAT contrast obtained for gold nano-spheres confined by two silicon oxide surfaces as a function of gap distance and particle height. The model is verified by using 380 particles immobilized at both confining surfaces using the known height as model input. Furthermore, we demonstrate that all three free model parameters can be obtained *in-situ* for individual diffusing nano-spheres from a single particle contrast measurement. The utility of this measurement is demonstrated in Section 4.6.4 by using the height distributions as input to a physical model and we determine the physical quantities describing the interaction of the spheres with the confining oxide surfaces. Lastly, the particle height for the gold spheres confined by the cover-glass and the polymer PPA is measured.

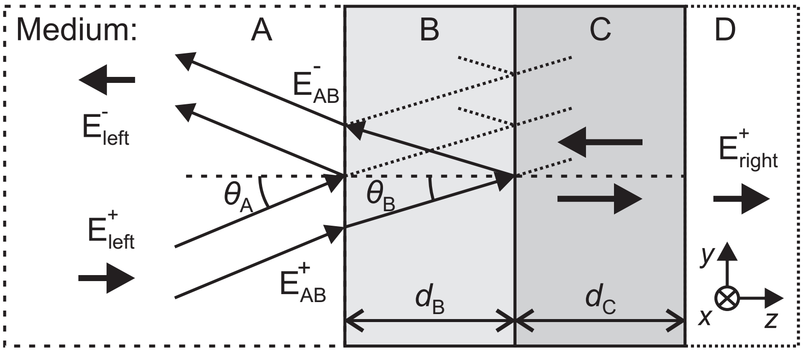

FIGURE 4.1: Propagation of light through a multi-layered media stack.

## 4.2 Transfer-matrix method

The reflectivity of a plan-parallel multi-layer stratified media stack is sketched in Figure 4.1 and can be modeled by employing the transfer-matrix method [110, 111]. Each interface of the stack is characterized by a reflection and a propagation part for the light entering the medium. The transfer-matrix of light entering from medium A and propagating through medium B to the next is calculated by

$$M_{\mathrm{AB}} = \frac{1}{t_{\mathrm{AB}}(\theta_{\mathrm{B}})} \begin{bmatrix} 1 & r_{\mathrm{AB}}(\theta_{\mathrm{B}}) \\ r_{\mathrm{AB}}(\theta_{\mathrm{B}}) & 1 \end{bmatrix} \begin{bmatrix} e^{ik_{\mathrm{B}}(\theta_{\mathrm{B}})d_{\mathrm{B}}} & 0 \\ 0 & e^{-ik_{\mathrm{B}}(\theta_{\mathrm{B}})d_{\mathrm{B}}} \end{bmatrix}, \tag{4.1}$$

where $t_{\mathrm{AB}}(\theta_{\mathrm{B}})$ and $r_{\mathrm{AB}}(\theta_{\mathrm{B}})$ are the transmission and reflection coefficients at the interface AB, $k_{\mathrm{B}}(\theta_{\mathrm{B}}) = 2\pi n_{\mathrm{B}} \cos(\theta_{\mathrm{B}})/\lambda$ is the z-component of the wave vector at incident angle $\theta_{\mathrm{B}}$ in medium B, and $d_{\mathrm{B}}$ is the thickness of layer B. The coefficients $t_{\mathrm{AB}}(\theta_{\mathrm{B}})$ and $r_{\mathrm{AB}}(\theta_{\mathrm{B}})$ are given by the Fresnel equations. The transfer-matrix $M_{\mathrm{AB}}$ gives the relation of light propagating in positive and negative z-direction at the interface AB and interface BC by

$$\begin{bmatrix} E^+_{\mathrm{AB}} \\ E^-_{\mathrm{AB}} \end{bmatrix} = M_{\mathrm{AB}} \begin{bmatrix} E^+_{\mathrm{BC}} \\ E^-_{\mathrm{BC}} \end{bmatrix}. \tag{4.2}$$

In the same way transfer-matrices can be determined for the other layers only for the last layer the propagation part has to be omitted. The total transfer matrix describing a layered stack e.g. with four media (see Figure 4.1) is then given by

$$M = M_{\mathrm{AB}} M_{\mathrm{BC}} M_{CD} \tag{4.3}$$

In case there is no incoming light from the right hand side ($E^-_{right} = 0$) the transmission and reflection coefficient can be obtained from the elements of the total transfer Matrix

$$t = \frac{E^+_{right}}{E^+_{left}} = \frac{1}{M_{11}} \tag{4.4}$$

$$r = \frac{E^-_{left}}{E^+_{left}} = \frac{M_{21}}{M_{11}}. \tag{4.5}$$

## 4.3 Effective incident angle of a focused laser beam

The previous section showed that the reflection coefficient of a multi-layered media stack depends on the incident angle $\theta$ (see Equation 4.1). Thus also light rays departing from normal incidence have to be considered when the stack is illuminated by the focused light of a microscope objective. The optical response of the system can be approximated by an effective incident angle $\theta_{eff}$, which speeds up numerical calculations considerably. This effective angle can be determined by comparing an experimental measured interference signal, which depends on the axial position of the cover-glass, with a simulated intensity pattern.

In order to use the cover-glass position as a reference, the piezo-stage has to be calibrated. Furthermore, for our nanofluidic slit changing the gap distance also leads to a change in the Young-Laplace pressure, such that the motion of the piezo and the cover-glass are not in 1:1 correspondence (see Section 3.1.1). Therefore, we performed the calibration and the measurement of the effective incident angle in a glass-air-silicon slit.

### Calibration of z-stage

The calibration was done by removing the objective, lenses and AOD from the setup (Figure 3.1 (a)). The collimated laser beam was reflected at the glass-air and air-silicon interfaces. The resulting interference signal was measured by the camera. A calibration factor of $z_{\text{cal}} = 0.984 \pm 0.001$ was obtained from the distance of interference extrema (the error is given by the standard error of the measurement). This value was confirmed by a second measurement, using a commercial interferometer (IDS3010, Attocube) on a silicon substrate mounted on the piezo stage.

### Interference of a focused laser beam by a glass-air-silicon slit

In our illumination scheme using a focused scanning laser beam, the incident light rays depart from normal incidence. As a result, the periodicity of the observed intensity modulations as a function of glass-silicon distance is greater than expected from a simple normal incident model. In order to tackle the problem we calculate the interference pattern observed using a high NA objective and compare it against the measured data.

We describe the laser beam by a paraxial Gaussian beam centrally incident on the back aperture of the objective. We follow the theory by Richards [112] describing the reflection of a focused optical field by a high NA objective. After reflection and refraction by the aplanatic optical lens the electric field distribution in the collimated farfield is given by [113],

$$E = -\pi E_0 e^{2ik\cos(\theta) z_0} \int_0^{\rho_{max}} e^{-\rho^2/w_0^2} \rho \left[ r_p(\theta) - r_s(\theta) \right] d\rho. \tag{4.6}$$

Where $\rho$ is the distance from the optical axis in cylindrical coordinates and $z_0$ is the distance between focus and interface. The Fresnel reflection coefficients $r_p(\theta)$ and $r_s(\theta)$ are functions of the incident angle $\theta$ in the focused beam. The schematic in Figure 4.2 (a) illustrates the sine law $\sin(\theta) = \rho/f$, which determines the relation of beam width $\rho$ and focal length $f$ of the objective. In order to arrive at the reflected field in the case of our glass-air-silicon system we use the transfer-matrix-method to calculate the reflection coefficient $r_p(\theta)$ and $r_s(\theta)$. The light intensity distribution is shown in Figure 4.2 (b) as a function of gap distance $d$, and $\theta$. As expected the gap distance modulates the overall light field. In angular direction we observe a maximum intensity at a finite divergence angle $\theta$ which is approximately independent of the gap distance $d$.

We approximate the signal of the scanned laser spot observed by the camera by the integrated intensity over all incident angles. An excellent fit (see Figure 4.2 (c)) to the measured data can be obtained using just two fit parameters, the Gaussian-beam width $w_0$, and the gap distance zero position $d_0$. The contact point at $d \approx 80\,\text{nm}$ fixes the absolute distance. The refractive indices of the stack $n_{\text{glass}} = 1.52$, $n_{\text{air}} = 1.00$ and $n_{Si} = 4.14$ are taken from literature. We obtain a beam width of 0.42 mm, giving rise to the strong underfilling of the objective and the fast decay of light intensities at increasing incident angles shown in Figure 4.2 (b).

The narrow angular distribution and the gap distance independence allows us to introduce an effective incident angle $\theta_{eff} = 5.9 \pm 0.1^\circ$ to describe the system [114]. We can use the effective angle to calculate the observed periodicity of

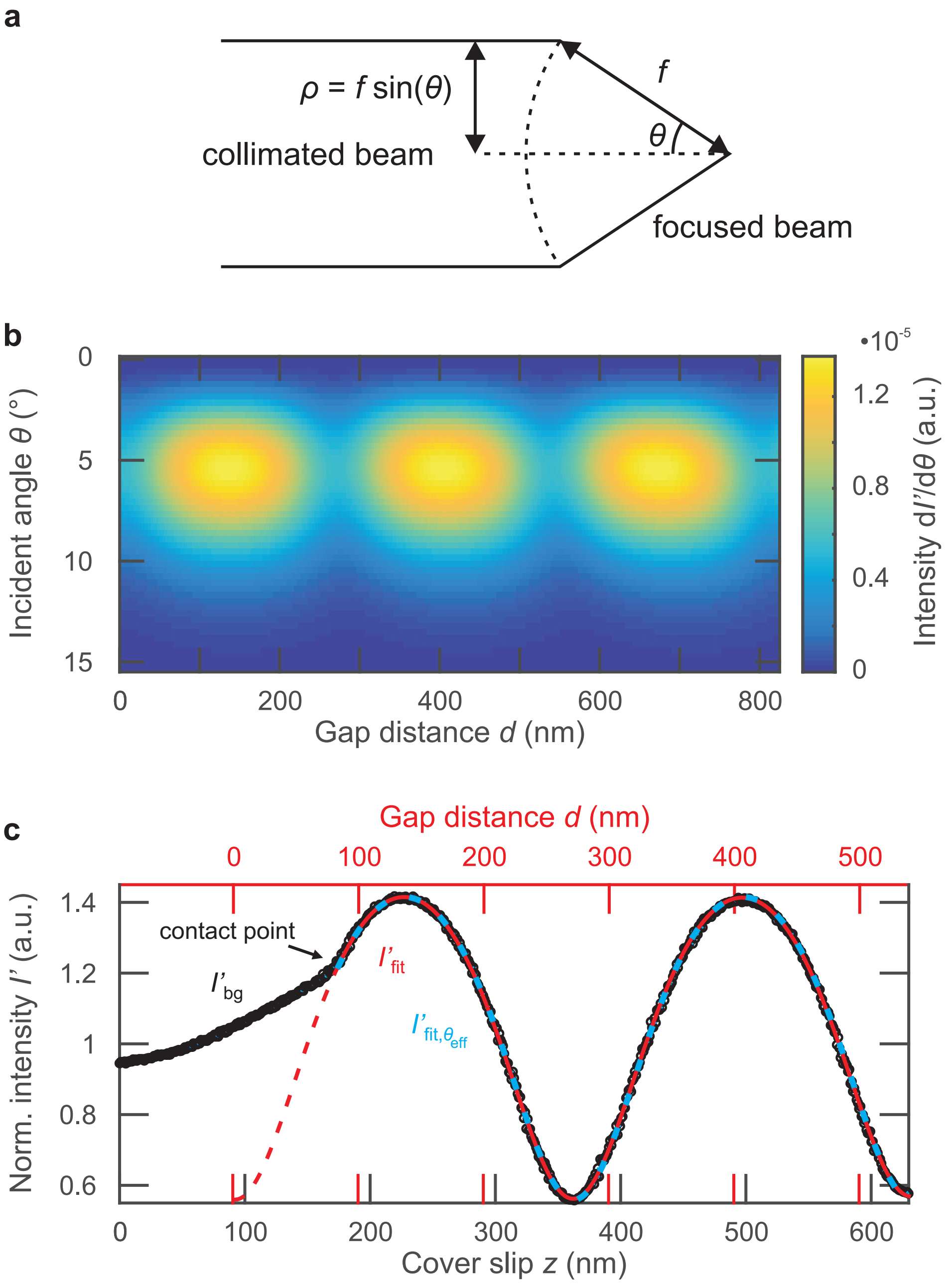

FIGURE 4.2: The dependence of the measured intensity on the incident angle due to focusing of a Gaussian beam on the measured intensity. (a) The sine law of geometrical optics. (b) Simulated intensity for varying gap distance of a glass-air-silicon nanoslit. The exponential decay for larger incident angles is caused by underfilling the objective with a Gaussian beam, while the integration of the azimuthal angle is weighting the intensity towards higher angles. (c) Measured signal from the background of a glass-air-silicon nanoslit (black) while moving the cover-glass along the optical axis. The dashed red line indicates a fit as a function of gap distance $d$ considering all incident angles. The dashed blue line is simulated with the same parameters but considering only the effective angle $\theta_{eff}$.

the interference pattern measured by the camera. We obtain an effective increase of the observed periodicity by $0.68\%$ in water as compared to normal incidence.

## 4.4 Parallelization and gap distance determination of the nanofluidic slit

The experiments described in this thesis require a high degree of parallelization of the two confining surfaces. This is necessary to prevent blockage of the mesa rim while approaching the two surfaces as well as to provide homogeneous conditions along the field of view. The parallelization of the surfaces was achieved by a measurement of the background interference signal in the four corners and center of the illuminated area (see Figure 4.3 (a)). From the relative phase shift of the respective median signals (see Figure 4.3 (b)) the tilt of the confining surfaces was determined. By tilting the substrate the phase difference was minimized using the position of the cross-correlation peak between the corner and the center signals. Generally, this led to a parallelization of less than 1 nm vertical deviation over a lateral distance of 10 $\mu$m.

The detected background interference signal of a nanofluidic slit like the one sketched in Figure 4.3 (c) can be described by two sources. One is the reflection of the light field from the glass surface $E_g$ and the other from the substrate $E_{sub}$. The total intensity is then given by

$$\begin{aligned} I_{bg} &= |E_{sub} + E_g|^2 \\ &= E_0^2 |r_{bg}|^2 = I_0 |r_{bg}|^2. \end{aligned} \tag{4.7}$$

For a tunable slit the background reflectivity $r_{bg}$ of a multi-layered stack (Equation 4.5) becomes a function of the gap distance

$$r_{bg}(d) = M_{21}(d)/M_{11}(d). \tag{4.8}$$

The gap distance $d$ in a nanofludic slit e.g. Figure 4.3 (c) is determined by matching the experimentally measured background intensity e.g. Figure 4.3 (d) with a simulated background interference signal using the transfer-matrix method (see Section 4.2) and the effective incident angle from the latter section. In order to compare the simulated and measured intensity both signals have to be normalized. The normalized background intensity is given by

$$I'_{bg}(d) = \frac{I_{bg}(d)}{\langle I_{bg} \rangle} = \frac{|r_{bg}(d)|^2}{\langle |r_{bg}|^2 \rangle}, \tag{4.9}$$

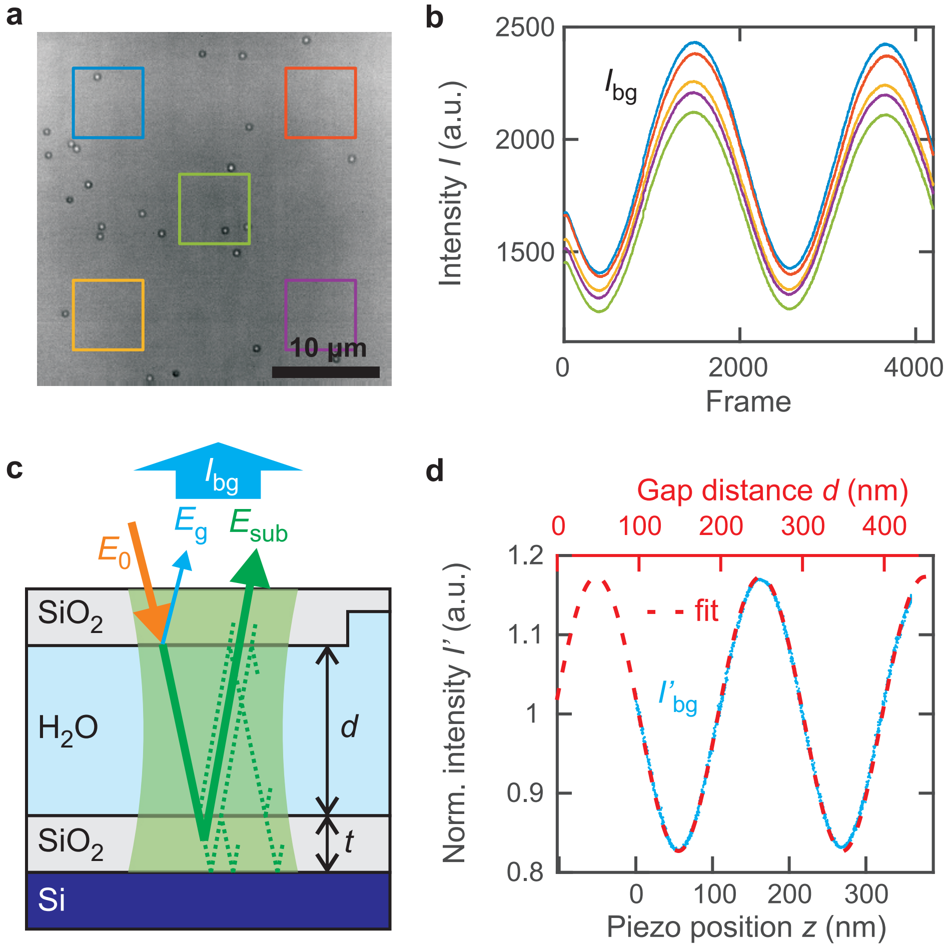

FIGURE 4.3: (a) Typical raw image of 60 nm Au nanospheres in the nanofluidic slit. (b) The averaged background intensity values in dependence of the axial position of the cover-glass holder are approximated by the median of the intensity values in the respective boxes in (a). (c) The background intensity is given by the square of the total field reflected by the nanofluidic slit (see Equation 4.7). The total field is the vector sum of the light reflected by the glass-water interface ($E_g$) and the light, which leaves the nanofluidic slit ($E_{sub}$) after multiple reflections (green dashed lines). (d) The recorded background intensity as a function of axial position of cover-glass holder. The dashed red line indicates a fit of Equation 4.9 to the normalized intensity values.

where the averaging is done over one period of the interference signal, i.e., a distance range of 200 nm due to the optical path length of 532 nm laser light in water.

### Gap distance in a symmetric $SiO_2$ - $H_2O$ - $SiO_2$ slit

Figure 4.3 (c) schematically illustrates our nanofludic slit with symmetric confining surfaces, which ensured that the same charge density was present on both surfaces. A $t = 51.0 \pm 0.5$ nm thick layer of $SiO_2$ was deposited by evaporation as well on the cover-glass mesa as on a silicon substrate. The thickness and the refractive index of silicon oxide $n_{ox} = 1.476 \pm 0.006$ were measured by ellipsometry. The effective incident angle $\theta_{eff}$ was determined using the refractive index of the cover-glass $n_{glass,D263} = 1.52$. We use Snell's law to propagate $\theta_{eff}$ into the dielectric layers and Fresnel's formulas to calculate the reflection and transmission coefficients. The refractive index of $n_{H_2O} = 1.33$ for water and $n_{Si} = 4.14$ for silicon are obtained from literature.

The dashed red line in Figure 4.3 (d) is a fit of Equation 4.9 to the data using two free parameters: a linear scaling factor c, and a relative offset $z_{offs}$ for the conversion of the z-axis to gap-distance values $d = cz + z_{offs}$. The scaling factor c is required because of pressure effects from the confined droplet between compliant cover-glass and substrate. We obtain c = 0.961, i.e., a deviation of about 4% from a 1:1 correspondence. For the results discussed in the following sections, we use the background intensity signal to obtain a calibrated measurement of the gap distance.

## 4.5 Image processing and particle tracking

Image capturing and analysis is a key part of video microscopy. The quality of the images is always limited by the noise, which is significant especially at short exposure times due to the limited signal. Noise can be divided into random noise, e.g., gaussian noise or shot-noise and fixed pattern noise (FPN). The FPN of a camera image consists usually of two contributions, a dark current offset and a difference in gain correction [115]. The pre-processing feature of the camera is used to compensate the FPN, by uploading a dark-image and a gray-image to the camera.

Figure 4.4 (a) shows a typical raw image of four spherical particles in the nanofluidic slit. The uneven background illumination originates from a non-linearity of the analog frequency control of the AOD driver. In case of immobilized particles,

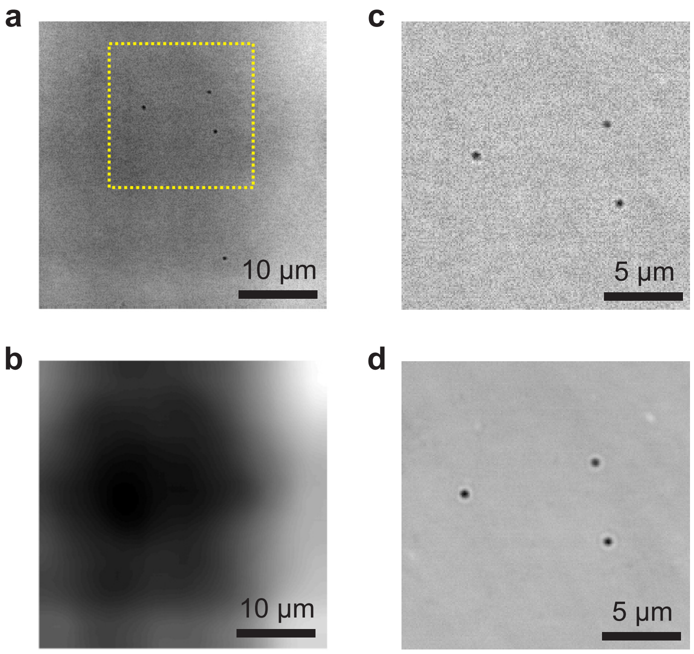

FIGURE 4.4: (a) Typical raw image of 60 nm diffusing Au nanospheres in the nanofluidic slit. (b) The difference in illumination is caused by the non-linear response of the AOD, which can be determined by applying a spatial median filter to each raw image. The effect can be corrected by normalizing the raw image with the background image. (c) The remaining contrast image contains the signal of the particles as well as some pixel noise. (d) Most of the noise has a fixed pattern, which can be corrected for moving particles by normalizing the raw images with a temporal averaged background intensity image.

the average is taken over the spatial neighborhood by applying a median average filter with a filter window of 30 x 30 pixels, much bigger than the observed particle size of 7 x 7 pixels as depicted in Figure 4.4 (b). The higher frequency content of the raw image, the particle signal as well as the remaining pixel noise are in the contrast image visualized in Figure 4.4 (c).

Radial symmetry-based tracking is used to identify the central lateral position of the nanosphere in the contrast image. This tracking algorithm yields accuracies near the theoretical limit, is fast in execution and detects any radially symmetric intensity distribution [116]. Here, in particular the latter is important to detect the position at interference conditions where the central contrast is zero and only a non-vanishing diffraction ring exists. We estimate a lateral localization accuracy of $\leq 5\,\text{nm}$ from the scatter of 35,000 detected positions from 7 immobilized destructive interfering particles with a signal to noise ratio (SNR) of $\approx 20$. This accuracy is in agreement with simulated particles[116] with a similar SNR.

Figure 4.4 (d) shows that for moving particles the remaining FPN of the background can be further reduced by normalizing the raw images with a temporal averaged background intensity image (see Equation 4.9). The temporal frame position as well as the temporal averaged background image is derived from least-square second-order polynomial fits to the extreme values of the periodic interference signal. The intensity values at pixel positions corresponding to tracked particle positions are excluded from the average. With this correction we measure a SNR of up to $\approx 50$, which corresponds to a sub $1.5\,\text{nm}$ localization accuracy[116].

The temporal frame positions of the minimum and maximum background interference values are used to piecewise match the experimentally measured and normalized background interference signal to the calculated intensities for the glass-water-silicon plan parallel system (see Equation (4.9)). As a result we obtain the conversion of frame time to gap distance $d$. The desired background intensity at the particle position is then obtained by interpolation at the respective gap distance $d$.

## 4.6 Particle height in a $SiO_2$ - $H_2O$ - $SiO_2$ slit

Similar to the determination of the gap distance from the background interference signal also the height of a particle can be derived from its intensity. The central particle intensity is determined by Gaussian fitting to the intensity values of the pixels in proximity of the particle, sorted by their radial distance to the sub-pixel center (see Section 4.5). The normalized measured intensity values of a

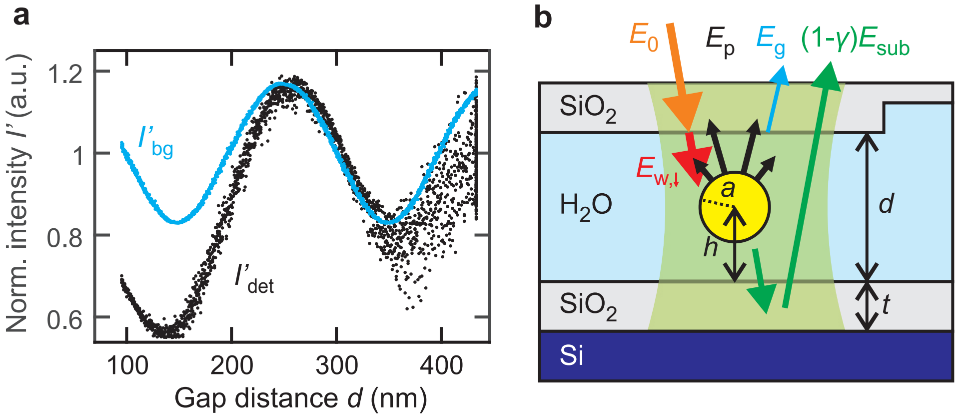

FIGURE 4.5: (a) Typical signal recorded from the background and from a diffusing nanoparticle as a function of gap distance $d$. (b) Model used for signal interpretation. The particle scatters and absorbs light, causing the background field to be reduced to ((1-$\gamma$) $E_{sub}$), see text for details. The particle reflection $E_p$ is modeled to be proportional to the field $E_{w,\downarrow}$ propagating towards the substrate in the water medium.

diffusing NP as a function of the gap distance is depicted in the black scatter plot in Figure 4.5 (a). The intensity of the normalized background is shown in blue.

### 4.6.1 Optical parametric model

From the data of the diffusing particle shown in Figure 4.5 (a), two critical aspects are immediately apparent: 1) The overall amplitude of the particle signal oscillations is roughly twice the amplitude of the background signal oscillations. 2) The particle intensity is less than the background intensity for most data points. These observations cannot be explained by the model often used for interpreting iSCAT intensity data in which the reflectivity of the glass surface is ignored [54, 55]:

$$I_{det} = |E_{ref} + E_p|^2 = I_0(|r_{ref}|^2 + |r_p|^2 + 2|r_{ref}r_p|cos\phi), \tag{4.10}$$

where $I_{det}$ is the detected intensity at the particle position and $\phi$ is the relative phase shift of the two interfering light fields from the reflective reference surface, $E_{ref}$, and the particle, $E_p$. Equation (4.10) predicts a particle intensity varying about a mean value $I_0(|r_p|^2 + |r_{ref}|^2)$, which is greater and not less than the background intensity $I_0|r_{ref}|^2$ and contradicts observation 2). Concerning observation 1), the background signal oscillations are of similar magnitude as the particle signal oscillations. This indicates that the fields originating from the glass and the particle reflections are of similar magnitude, and thus the glass reflection cannot be neglected.

Here we propose the following model as sketched in Figure 4.5 (b). For the detected interference signal, we consider three interfaces as sources for light reflection, i.e., at the substrate $E_{sub}$, at the particle $E_p$ and at the glass surface $E_g$. That is we have two reference surfaces, the glass and the substrate. As the particle is located above the substrate, we have to consider the effect of the presence of a particle on the reflected substrate field, $E_{sub}$, because the light has to pass the particle before it arrives at the substrate and on the way back to the camera. To estimate the significance of this effect, we consider the effective areas involved when imaging the particle. The optical resolution of the microscope is given by the diffraction limit to be $\approx 0.61\lambda/\mathrm{NA} \approx 250\,\mathrm{nm}$. As a particle image, we observe the interference signal of the light reflected from this area of the substrate with light scattered by the particle and the glass. Thus it is apparent that a $60\,\mathrm{nm}$ diameter Au particle scatters and absorbs a significant fraction of the relevant incoming light. This effect is even enhanced by the fact that the light interacts with a metallic particle close to its plasma frequency. We account for the reduced light intensity by introducing a parameter $\gamma$ describing the fraction of the incident field which is scattered or absorbed by the particle. As a consequence, the field emerging from the substrate at the particle location is reduced to $E_{s,p} = (1-\gamma)E_{sub}$. The fraction $\gamma$ of the light interacting with the particle is partially scattered by the particle, transmitted to and collected by the objective. We term this light $E_p = \gamma E'_p$, where we rescale the unknown magnitude of the particle reflection with $\gamma$. Then we can write:

$$\begin{aligned} I_{det} &\approx |(1-\gamma)\,E_{sub} + E_p + E_g|^2 \\ &= |(1-\gamma)\,(E_{sub} + E_g) + \gamma(E'_p + E_g)|^2 \qquad (4.11) \\ &= I_0|(1-\gamma)r_{bg} + \gamma r_{p,g}|^2, \qquad (4.12) \end{aligned}$$

where $r_{bg}$ is the reflection coefficient of the background far from a particle. It describes the multiple reflections of the light in the water medium, the transmission through the glass interface, and the interference with the light reflected by the glass-water interface. Because of the interference, $r_{bg}$ is now a function of the gap distance $d$. Also, $r_{p,g} = (E'_p + E_g)/E_0$ can be viewed as the reflection coefficient of the glass-particle system if only the light fraction $\gamma$ interacting with the particle is considered. It describes the light interacting with the particle and interfering with light reflected by the glass surface.

To complete our model, we still need to approximate the reflection coefficient for the glass-particle system, $r_{p,g}$. For this we need to compute the light field scattered by the particle. We assume that the amplitude of the scattered field is proportional to the amplitude of the incoming field within the nanofluidic gap, i.e. the wave propagating in the water medium towards the substrate, $E_{w,\downarrow}$, see

Figure 4.5 (b). The complex amplitudes of $E_{w,\downarrow}$ (and $E_{w,\uparrow}$) at the glass-water interface are determined from the transfer-matrix formalism as follows:

$$\begin{bmatrix} E_{w,\downarrow}(\theta_w) \\ E_{w,\uparrow}(\theta_w) \end{bmatrix} = \left( \frac{1}{t_{g,w}(\theta_w)} \begin{bmatrix} 1 & r_{g,w}(\theta_w) \\ r_{g,w}(\theta_w) & 1 \end{bmatrix} \right)^{-1} \begin{bmatrix} 1 \\ r_{bg}(\theta_w) \end{bmatrix} E_0. \quad (4.13)$$

The incoming field $E_{w,\downarrow}$ propagates a distance $(d-h)/\cos(\theta_w)$ towards the particle (centered at height $h$), is reflected according to a complex reflection coefficient $r_p$, propagates back to the glass interface, and is transmitted through the water-glass interface. We neglect any light transmitted through the particle and reflected by the substrate or forward-scattered light from the upward propagating wave $E_{w,\uparrow}$. The back-scattered light is emitted in several directions, transmitted through the glass interface, and arrives at the camera pixel, where it interferes with itself and with the light reflected from the glass surface. We incorporate all of the losses and phase shifts inherent in the path towards the camera in the complex scattering coefficient $r_p$ and thus obtain the following relation for the reflection coefficient of the particle-glass system:

$$r_{p,g} \approx r_g + E_{w,\downarrow}/E_0 e^{2ik_w[d-h]} p e^{i\phi_0}, \quad (4.14)$$

where we assign an amplitude $p$ and an accumulated scattering phase $\phi_0$ to the particle reflection coefficient $r_p$, and $k_w$ is the z-component of the wave vector incitent at an angle $\theta_w$ in water.

Equations (4.12), (4.8), and (4.14) describe the optical iSCAT signal of a particle in a nanofluidic gap. The excellent fit of the background intensity to the model for $I_{bg}$ allow us to retrieve all the values for the transmission and reflection coefficients concerning the glass and the substrate interference. In order to determine the particle height $h$ [Equation (4.14)] the remaining unknown parameters for describing the particle signal have to be specified, the fraction $\gamma$ of the incoming light interacting with the particle [Equation (4.12)], and the particle's scattering amplitude $p$ and the effective scattering phase $\phi_0$ [Equation (4.14)].

### 4.6.2 Model verification using immobilized particles

We tested the model derived in the preceding section by a measurement of $I_{det}$ and $I_{bg}$ for particles of radius $a = 30$ nm immobilized at the surface of the cover-glass and at the substrate-water interface (Figure 4.6 (a)), thus fixing the particle height, $h$, to $h = d - a$ and $h = a$, respectively. A total of 380 particle signals were analyzed, 241 attached at the cover-glass and 139 at the substrate. The particles were immobilized by droplet drying. The normalized raw particle signal $I'_{det} = I_{det}/\langle I_{bg}\rangle$ and the normalized contrast $I'_{ctr} = (I_{det} - I_{bg})/\langle I_{bg}\rangle$ of the particles are

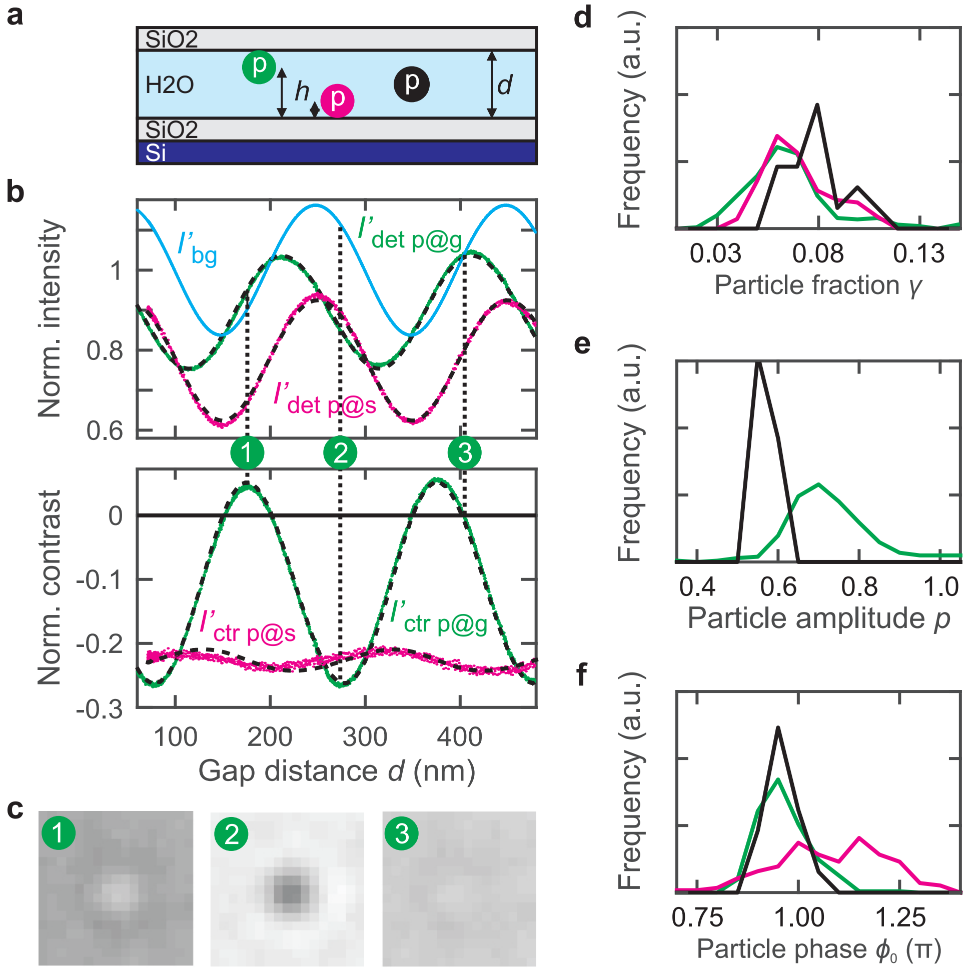

FIGURE 4.6: Verification of the optical model using particles fixed to the cover-glass and substrate. (a) Schematic of particles fixed to the cover-glass (green), to the substrate (magenta) or freely diffusing (black). (b) Examples for measured intensities (top) and contrast signals (bottom) for background and particle intensities for particles attached to the cover-glass (green) and the substrate (magenta). Dashed black lines represent fits according to the optical model. (c) Sample images for maximal positive, maximal negative and zero contrast. Tracking was possible through zero contrast because of the nonzero radial signal at zero center contrast. (d-f) Statistics for the optical parameters interaction fraction $\gamma$, intensity factor $p$ and phase $\phi_0$ describing the signal of all particles measured.

shown in Figure 4.6 (b) for two selected particles, one sticking to the substrate (magenta) and the other sticking to the glass (green). In addition, $I'_{bg}$ measured in the neighborhood of the particles is displayed in blue in Figure 4.6 (b).

We note that the signal for the particles fixed to the cover-glass was obtained by moving the objective in parallel with the cover-glass in order to keep the particles in focus. If we measured the signal with a fixed position of the objective we observed an additional increasing phase with displacement of the particle out of focus, likely due to an accumulated Gouy phase. The effect is described in Section 4.6.2 and was compensated for the measurement of the freely diffusing particles.

The dashed lines in Figure 4.6 (b) correspond to the best fit to the data according to our model. For particles fixed to the cover-glass, all three parameters were obtained from the fit. For particles sticking to the substrate, the raw signal is dominated by the reduced background signal $(1-\gamma)^2 I_{bg}$, evidenced by the vanishing relative phase of $I_{bg}$ and $I_{det}$. The particle signal adds to the substrate signal with a fixed phase relation because of the fixed distance between particle and substrate. Therefore for particles fixed to the substrate, the phase $\phi_0$ and amplitude $p$ could not be obtained simultaneously. Here we fixed $p$ to an average value of $p = 0.65$ as obtained from the other measurements and we used the particle scattering phase $\phi_0$ as fit parameter.

The histograms shown in Figure 4.6(d-f) represent the statistical distributions of the free parameters $\gamma$, $p$, and $\phi_S$, respectively, as obtained from the fit to a total of 380 particles. Histograms for particles immobilized on the cover-glass, on the substrate and freely diffusing (16 particles, evaluation see next section) are shown in green, magenta and black, respectively. We obtained histograms of similar width for all measurements. It is apparent that the values for the freely diffusing particles, in particular for $p$, are slightly shifted in comparison to those obtained obtained for the fixed particles. We attribute these deviations to the fact that during the drying process the interface between the particle and the cover-glass was filled with organic residues which have a higher refractive index than water, resulting in higher reflectivities. As mentioned above, for the particles fixed to the substrate, we had to fix $p$. Because the phase now has to adapt for the total signal change, the values obtained for $\phi_0$ have a much wider distribution than those obtained for particles fixed at the glass surface or the freely diffusing particles.

In summary, fits to all 380 particle signals could be obtained with high fidelity. The standard deviation of the fits to the intensity data $I_{det}$ (see Figure 4.6 (b) for the particles sticking to the cover-glass surface was $(7.9 \pm 2.9)\,10^{-3}$ and for the particles sticking to the substrate $(1.3 \pm 0.4)\,10^{-2}$ of the normalized intensity,

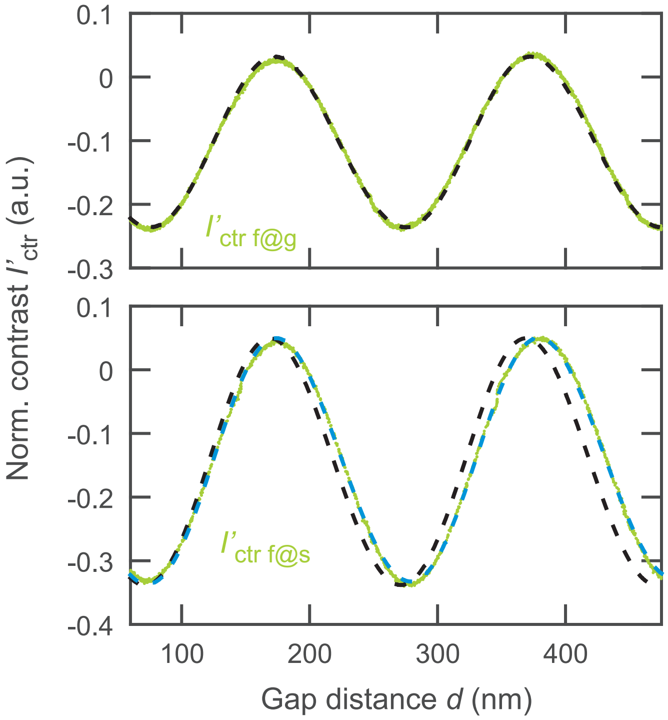

FIGURE 4.7: The effect of the focus position on the particle contrast. Examples of measured contrast signals for a particle attached to the cover glass (green). The dashed black lines represent fits according to our optical model without considering defocussing. In the upper plot the height of the objective is adjusted so that the particle at the cover glass stays in focus. In the lower graph the height of the objective is not changed so that a particle at the substrate stays in focus. The dashed blue line corresponds to a fit in which an additional linearly increasing phase shift is considered.

which quantifies the good agreement of the model to the data. In addition, the values obtained for fixed and moving particles are in good agreement for all particle sets investigated. We interpret the excellent agreement as a first indication of the validity of our model.

### Effect of focus position

Two experiments with particles fixed to the cover-glass are carried out to investigate the effect of the focus position. In the first measurement, the height of the cover-glass and the objective are moved in parallel with a fixed distance, and thus the sticking particles stay in focus as the gap distance changes. The contrast behavior of these particles (Figure 4.7 upper plot, green data) can be described by our model (dashed black line) without correction. In the second measurement, the focus is adjusted to a particle sticking at the substrate surface and the height of the objective is constant, while varying the gap distance and height of the investigated particle. The contrast oscillates for these particles (Figure 4.7 lower plot, green data) with a longer wavelength than in our model (dashed black line). This effect may originate from the Gouy phase and is phenomenologically addressed by adding a phase shift to the scattering phase in Equation (4.14) that linearly increases with the distance of the particle from the focus plane at the substrate $\Delta\phi = z_f \pi (h - a) n_{H_2O}/\lambda$. At a factor of $z_f = 0.117$, the simulated contrast (dashed blue line) coincides with the measured data. This effect is also considered in the next section for the suspended particles.

### 4.6.3 In-situ contrast calibration for diffusing nano-spheres

The measured contrast values $I'_{ctr}$ of a freely diffusing particle confined in the gap, recorded at varying gap distance $d$, are depicted as black scatter plot in Figure 4.8 (a). The data were recorded at 500 FPS and an illumination time of $\approx 100\,\mu$s, see Section 3.1.2. The normalized contrast values are contained in a well-defined range $-0.4 \leq I'_{ctr} \leq 0.05$, which we will use to determine the three unknown parameters $\gamma$, $p$, and $\phi_0$ on an individual particle level.

Using the optical model from Equations (4.12), (4.8), and (4.14), and using a set of trial parameters $\gamma$, $p$, and $\phi_0$, we calculate the range of expected particle contrasts for all possible heights within the gap, $a \leq h \leq d - a$. The minimum and maximum of the calculated contrasts define a theoretical envelope for possible particle contrasts observed experimentally. These extremal contrasts are depicted in Figure 4.8 (a) as green and blue lines. The fitting procedure involves optimizing the three parameters, $\gamma$, $p$, and $\phi_0$ such that the calculated envelope matches the range of measured contrasts in the experimental data. To characterize the deviation of the calculated envelope from the experimental data, we determined the contrast difference of the experimental data to the calculated envelope in a $50\,$nm wide band (blue and green areas in Figure 4.8 (a)). The plotted histograms of the resulting values are shown on the right-hand side of Figure 4.8 (a). The center position of the blue band was obtained from the position of maximal contrast after smoothing of the contrast data. Optimal values of $\gamma$, $p$, and $\phi_0$ were found by iteratively calculating the contrast envelope and histograms of the deviations until the peaks of the histograms were at zero. The optimized histograms and best fit envelope are shown in Figure 4.8 (a). This procedure was then repeated for each particle.

For an ideal noise-free measurement, the contrast histograms would comprise a sharp maximum feature given by the contrast envelope. In the measurements,

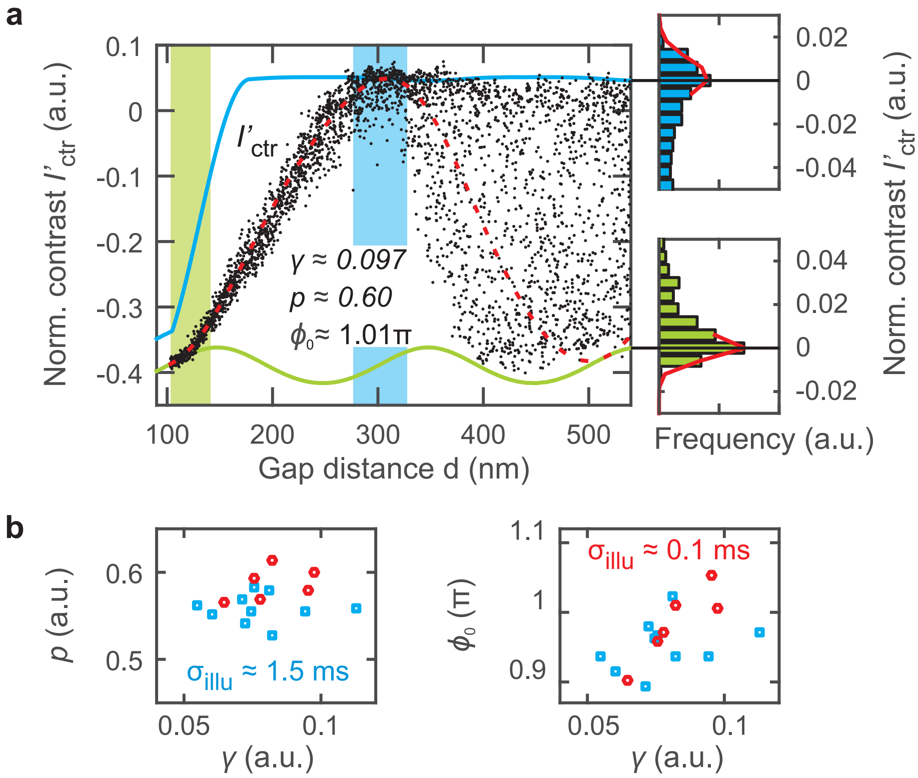

FIGURE 4.8: Contrast calibration for a diffusing particle in a $SiO_2$ - $H_2O$ - $SiO_2$ slit. (a) Measured contrast signal of a single diffusing particle and envelopes of the simulated maximum (blue) and minimum (green) particle contrast for varying gap distance $d$. The dashed red line illustrates the simulated contrast for a particle at mid-gap position. The histograms are calculated for the marked regions and show the frequency of observing a particle contrast relative to the contrast value given by the envelope. Owing to noise, contrast values outside the envelope are observed, which are characterized by Gaussian distributions (red lines) having widths of $\sigma = 0.0085$ and $\sigma = 0.0055$ for the top and the bottom envelope, respectively. (b) Correlations of the particle phase $\phi_0$ and the effective scattering amplitude $p$ with the fraction $\gamma$ for illumination times of $\approx 100\,\mu$s (red circles) and $1.5\,$ms (blue squares).

we find a Gaussian tail, indicated by the red lines in the histograms in Figure 4.8 (a). We attribute this broadening to both noise from laser and camera and the fact that the particles may exhibit a time-dependent scattering cross-section due to shape asymmetry. The width of the Gaussian tails was typically less than 0.01 normalized intensity, which corresponds to errors of less than 2 nm for intermediate contrast values. The error in optimizing the fit may be approximated by the bin width of the histograms, which here was 0.01 normalized intensity. This corresponds to an additional systematic height error of approximately 2 nm for intermediate contrast values.

We found that the contrast envelope was predominantly related to $p$ and $\gamma$. The phase $\phi_0$ corresponds to an apparent change in particle height and had little effect on the envelope for large $d$. However for small $d$, the possible values for $\phi_0$ are constrained to a narrow range because of the increasing confinement. Here we increased the confinement to roughly 90 nm, resulting in average distance of 15 nm from the particle surface to the confining interfaces. We prepared both surfaces with the same material, therefore we assume that the particle is located at the center of the gap, $h_c = d/2$ (see dashed red line in Figure 4.8 (a)) for strong confinement, e.g. within the green band shown in Figure 4.8 (a).

From the procedure described above, we obtain the parameters describing the optical response of the system for individual diffusing particles. This allows us to compare the parameters obtained for all individually diffusing particles. Figure 4.8 (b) shows the correlations of $\phi_0$ and $p$ with $\gamma$. The phase $\phi_0$ may be interpreted as the distance between the particle origin and the actual plane of light reflection. Because the particle radius $a$ and the skin depth of gold are of similar magnitude, an average phase of about $\pi$ is observed. For a smaller particle (smaller value of $\gamma$), the reference plane is shifted towards the substrate interface and therefore the particle exhibits a more negative phase. The reflection amplitude $p$ changes very little with the particle size, see Figure 4.8 (b), lower panel. This is expected because $p$ describes the reflectivity of the light fraction that interacts with the particle. The minor increase of $p$ with $\gamma$ may be explained by the fact that for larger particles the scattering to extinction ratio increases [117].

Once the optimal fit parameters have been obtained, the model can be used to calculate contrast values for given height values. The background of Figure 4.9 (a) and (b) shows this calculated signal as a function of gap distance using the fit parameters obtained for the respective particles. The 200 nm periodicity of the contrast with the particle height is due to the 400 nm wavelength of light in water. The additional signal from the glass interface modulates the contrast along the axis of the gap distance $d$, and also modulates the height values of extremal contrast by about 10 nm, see blue and green lines in Figure 4.9 (a). To

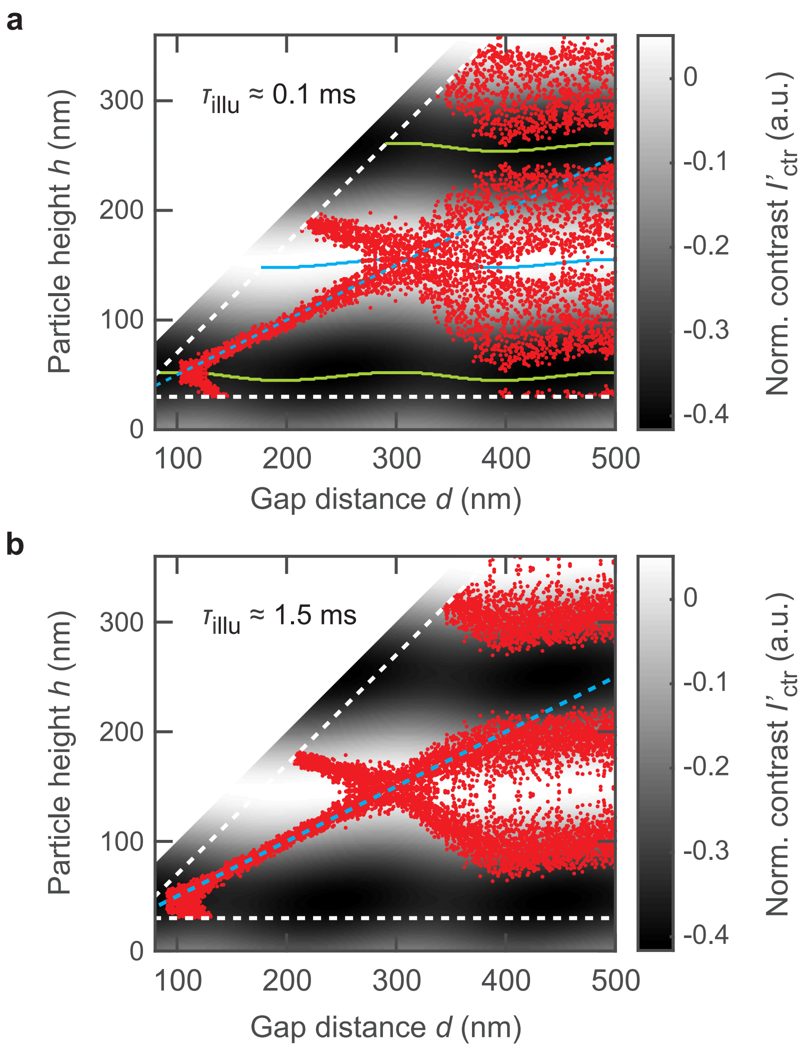

FIGURE 4.9: Measurement of the particle height in a $SiO_2$ - $H_2O$ - $SiO_2$ slit. (a,b) Attributed particle heights (red) obtained for illumination times of $\approx 100\,\mu$s in (a) and $1.5$ ms in (b). The gray-scale images visualize the simulated contrast for varying gap distance $d$ and particle height $h$. The blue and green lines denote the position of maximum and minimum simulated contrast, respectively. The height values are restricted to the physically possible values within the gap given by the finite particle radius (dashed white lines). The dashed blue line illustrates the position of the gap center.

obtain the height values for a measured contrast, we interpolated the calculated signal between the extremal values. Depending on the gap distance, this leads to single-valued or multi-valued results for the particle height. Contrast values measured outside the envelope function were set to the height values corresponding to extremal contrast.

The red data points in Figure 4.9 (a) and (b) display the height values obtained that correspond to the measured contrast data recorded with an illumination time of $\tau_{\text{illu}} \approx 100\mu\text{s}$ and $\tau_{\text{illu}} \approx 1.5\,\text{ms}$, respectively. Because of the periodicity of the intensity along the $h$-axis, often more than one solution exists for possible particle heights, e.g. for gap distances $d \geq 220\,\text{nm}$. Therefore multiple "mirror" branches appear, and it is not possible to determine a priori which solution branch is the physical one. Note that we plotted data points only if the heights are within the range of accessible heights for the particle given by the gap distance, i.e. $a \leq h \leq d - a$, see dashed white lines in Figure 4.9 (a) and (b). Consequently for gap distances of $120\,\text{nm} \lesssim d \lesssim 220\,\text{nm}$, the height data is single-valued and the corresponding branch can be interpreted as the physical branch. For this branch the heights are confined to a small band around the gap center denoted by the dashed blue line. In our system of a particle confined by symmetrically charged surfaces, this is precisely what is expected. Indeed, in the range $150\,\text{nm} < d < 250\,\text{nm}$, we determine an average standard deviation of the average measured particle height from the gap center of 2 nm for all 16 particles measured, which corroborates the validity of our model.

At gap distances of $d > 330\,\text{nm}$, the two measurements are distinctively different, with more confined bands of particle positions for the longer illumination time experiment shown in Figure 4.9 (b). At these gap distances, which are large compared to the Debye length of the system, the repulsive force from the surfaces is expected to become small (see also the next section). Therefore we expect a uniform distribution of possible height values along the h-axis around the gap center. This clearly is not the case in Figure 4.9 (b), where gaps with a width of $\approx 75\,\text{nm}$ develop around the extremal contrast positions. The long illumination time effectively averages the apparent particle contrast for the fast and practically unconfined moving particles. The maximum contrast for a particle with extended illumination time corresponds to an average contrast value as the particle diffuses through the extremal contrast region. A simple calculation yields that the contrast gap of $\approx 75\,\text{nm}$ observed in the experiment corresponds to a diffusion length of roughly $140\,\text{nm}$ or a normal diffusion coefficient of $D_{\perp} \approx 6\,\mu\text{m}^2/\text{s}$. This is consistent with a diffusion coefficient $D = (k_{\text{B}}T)/(6\pi\eta a) \approx 7.2\,\mu m^2/s$ and a diffusion length of $\Delta z = \sqrt{(2D\Delta t)} \approx 150\,\text{nm}$ for an integration time (illumination time) of $\Delta t = \tau_{\text{illu}} = 1.5$ ms as obtained for a freely moving particle using the

Stokes-Einstein-equation [64], and keeping in mind that the confinement slows down the diffusion [118]. Similarly from the contrast gaps of $\approx 25\,$nm visible in Figure 4.9 (a), one can infer a diffusion length of $40\,$nm or an illumination time of $150\,\mu$s, consistent with the experiment.

Clearly, a short illumination time is required to obtain a faithful distribution of particle heights, in particular at the extremal values of the particle contrast. On the other hand, for freely moving particles and short illumination times the measured heights for intermediate contrast values have high accuracy because here the contrast scales linearly with height. In the next section, we will use this fact to characterize the physical properties of the system.

### 4.6.4 Application: Study the particle surface interaction

In this section, we use the measured height distributions to obtain the physical parameters describing the interaction of the charged sphere confined between the like charged planes. The forces on the particles in the nanofluidic gap originate from the interaction of the charge and electrostatic double-layer potentials existing around the particle and close to the planes as described in Section 2.1.2.

Equations (2.12)-(2.16) describe the interaction energy of a sphere in nanofluidic confinement between similar planes. At the timescales investigated here, the system is in thermodynamic equilibrium and therefore the interaction energy give direct access to the occupation probabilities $p_{sim}(h)$ of a particle residing at height $h$ via the Boltzmann distribution:

$$p_{sim}(h) \propto e^{-W(h)/k_{\mathrm{B}}T}. \tag{4.15}$$

To compare Equation (4.15) with the experimental results, we obtain an experimental probability $p_{\exp}(h)$ from the $h(d)$ data shown in Figure 4.9 (a) by calculating normalized occupation histograms for $d$ and $h$ intervals of $4\,$nm. Because of the periodic nature of the particle contrast, we often cannot assign single-valued heights to a particular particle contrast. Instead, when we calculate $p_{\exp}$, we weigh all possible heights for a given contrast as a single measurement. As a result the "probability" $p_{\exp}(h)$ shown in the left column in Figure 4.10 (a) does not add up to unity for a given gap distance, $d$, but rather to the average number of possible $h$-solutions for each contrast. However, the procedure ensures that the probability for the physical branch of $h$-values can be compared with the model calculations shown in the right column in Figure 4.10 (a) titled "$p_{sim}(h)$". For fitting the model to the data we generate a simulated map of particle height "probabilities" including the unphysical height positions for a given particle contrast. For this we simply mirror the simulated particle probabilities $p_{sim}(h)$ at

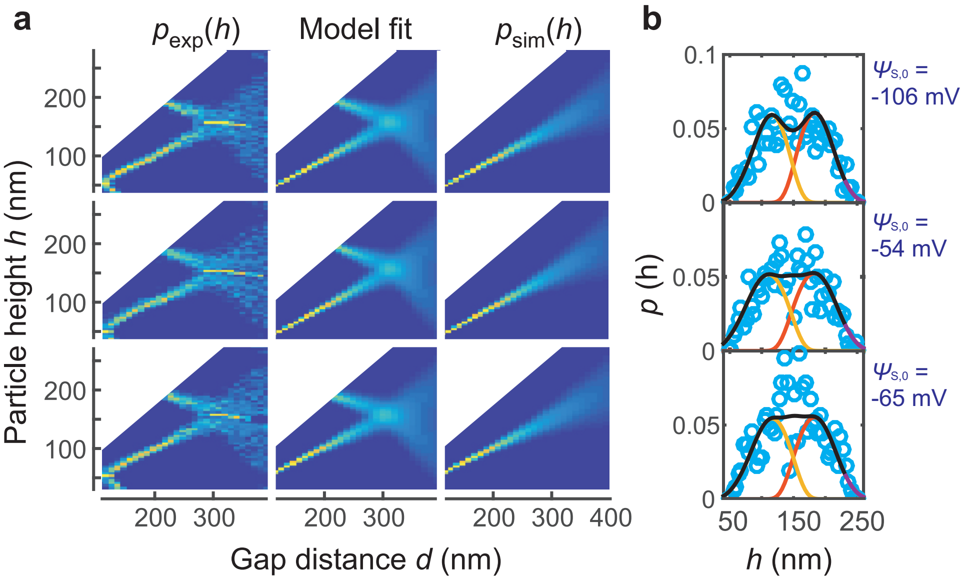

FIGURE 4.10: Fit to a physical model based on the linear superposition approximation (LSA). (a) Comparison of experiment and simulation for three particles. Shown are experimentally obtained occupation probabilities $p_{\mathrm{exp}}$ and model fit results including (Model fit) and excluding ($p_{sim}(h)$) the unphysical height positions for a given particle contrast. (b) Measured histograms (blue circles) and fit results (lines) averaged in the range of gap distances of $350\,\mathrm{nm} < d < 400\,\mathrm{nm}$. The simulated probability $p_{sim}$ is shown in red, the mirrored probability in yellow and the sum of both in black.

the experimentally determined height values of maximum particle contrast. The result of this procedure is shown in Figure 4.10 (a) in the middle column.

The fits were performed using a non-linear least square fit method in the range of gap distances from 240 to 400 nm. The range was restricted to minimize errors from the very narrow distributions for $d < 240\,\mathrm{nm}$, where the width of the distributions is comparable to the diffusion length during illumination. The surface potential of the silicon oxide interfaces was approximated from literature [60] to be $\psi_{P,0} = -67\,\mathrm{mV}$. We resort to a two step fitting procedure to enhance the convergence of the fits. In a first step we fixed the surface potential $\psi_{S,0}$ for all spherical particles to the experimentally measured zeta potential $\psi_\zeta = -58\,\mathrm{mV}$. Under this condition we obtained a Debye length of $\kappa^{-1} = 23.4 \pm 0.1\,\mathrm{nm}$ from a global fit to all particles. We like to point out that the Debye length determined by conductivity measurements is roughly 35% smaller (see Table 3.2). One reason might be the finite illumination time, which leads to a narrower measured particle distributions and thus a longer Debye lenght. However, for a more sophisticated analysis further measurements at different illumination times are required, which should be compared with Brownian dynamic simulations [105].

In a second step we fixed the Debye length $\kappa^{-1} = 23.4$ and used the individual particle potentials as fit parameters. The obtained values of $\psi_{S,0} = -106 \pm 8, -54 \pm 4$, and $-65 \pm 5\,\mathrm{meV}$ and the corresponding simulation data are shown in Figure 4.10 (a) and (b) from top to bottom.

Average cross-sections through $p_{sim}(h)$ and $p_{\exp}(h)$ for a gap distance range of $350 - 400\,\mathrm{nm}$ are show in Figure 4.10 (b). The simulated result is shown as red line. The mirrored and the summed signals are shown in yellow and black, respectively. There is good agreement of fit and data for a distance $h(d) - h_{mirr} > 20\,\mathrm{nm}$, as expected from the diffusion length within the illumination interval of $\approx 40\,\mathrm{nm}$.

The quality of the agreement with the LSA approximation further validates our optical model. The quantities obtained for the physical parameters are in accordance with the expected values, and the surface potentials for the individual particles could be obtained.

## 4.7 Particle height in a SiO$_2$ (D263) - H$_2$O - PPA slit

The open setup permits the use of several samples and coatings. In the later sections we will pattern the thermally responsive polyphthalaldehyde polymer (PPA) to shape the potential landscape experienced by the particles. Therefore particle height measurements of particles confined between the cover-glass and polymer are of particular interest. The height for an individually diffusing particle is determined by its contrast using the same optical model as described in Section 4.6.1, but instead of a single layer of $SiO_2$ a spin coated double layer of polymers (HM and PPA) has to be considered. A 175 nm thick PPA film was spin coated on top of a 52 nm thick cross-linking polymer (see Section 3.2.2) for further details and measured refractive indices). The scatter plot in Figure 4.11 (a) depicts the experimentally measured and normalized contrast of a diffusing 60 nm Au particle for varying gap distance $d$ between the confining cover-glass (D263) and the PPA surface.

The iterative method, as described in detail in Section 4.6.3, optimizes the parameters $\gamma$, $p$ and $\phi_0$ iteratively until the modeled extremal contrast values (blue and green line in Figure 4.8 (a)) for the range of possible particle heights ($a \leq h \leq d - a$) best define the envelope for the measured contrast values (black symbols). The dashed red line illustrates the calculated contrast of a particle positioned in the middle of the gap.

Three regions can be identified concerning the width of the contrast distribution at a given gap distance. For gap distances between $150\,\mathrm{nm} < d < 300\,\mathrm{nm}$ the width of the contrast distribution decreases the more the particle is confined by the electrical double layers of the walls. Thus we consider differences in particle height as the dominant origin of contrast variation. For smaller gap distances the width stays constant until there is almost no distribution in the third region for $\lesssim 65$ nm. While the first distribution and the third look similar for other particles the spread in the second region varies. We interpret the behavior in this region to be dominated by the shape of the particles, which is depicted in the SEM image in Figure 3.8 (b). Rotation of asymmetric shaped particles can be the cause of these intensity fluctuations, if the illumination time is not much longer than the rotational relaxation time. The particle illumination time in this experiment was $\tau_{\mathrm{illu}} \lesssim 40\,\mu$s as explained in detail in Section 3.1.2. For the 60 nm gold spheres, using Equations (2.29) and (2.30), we estimate an unhindered relaxation time of $\tau_r \approx 70\,\mu$s. In the next chapter we will show that the lateral diffusion is hindered for the observed interval of gap distances and the same effect is also expected for the rotational diffusion. This would further delay the rotational relaxation time; thus the illumination time is shorter then the rotational relaxation time. Consequently, contrast fluctuations due to rotation are not fully averaged during the time of illumination. The contrast fluctuation abruptly stops once the particle becomes immobilized on one of the confining surfaces (see inset in Figure 4.11 (a)).

The contrast modeled as a function of gap distance $d$ and particle height $h$ is shown as the grayscale background in Figure 4.11 (b). To obtain the height values (blue dots) for a measured contrast we use the simulated values for a given gap

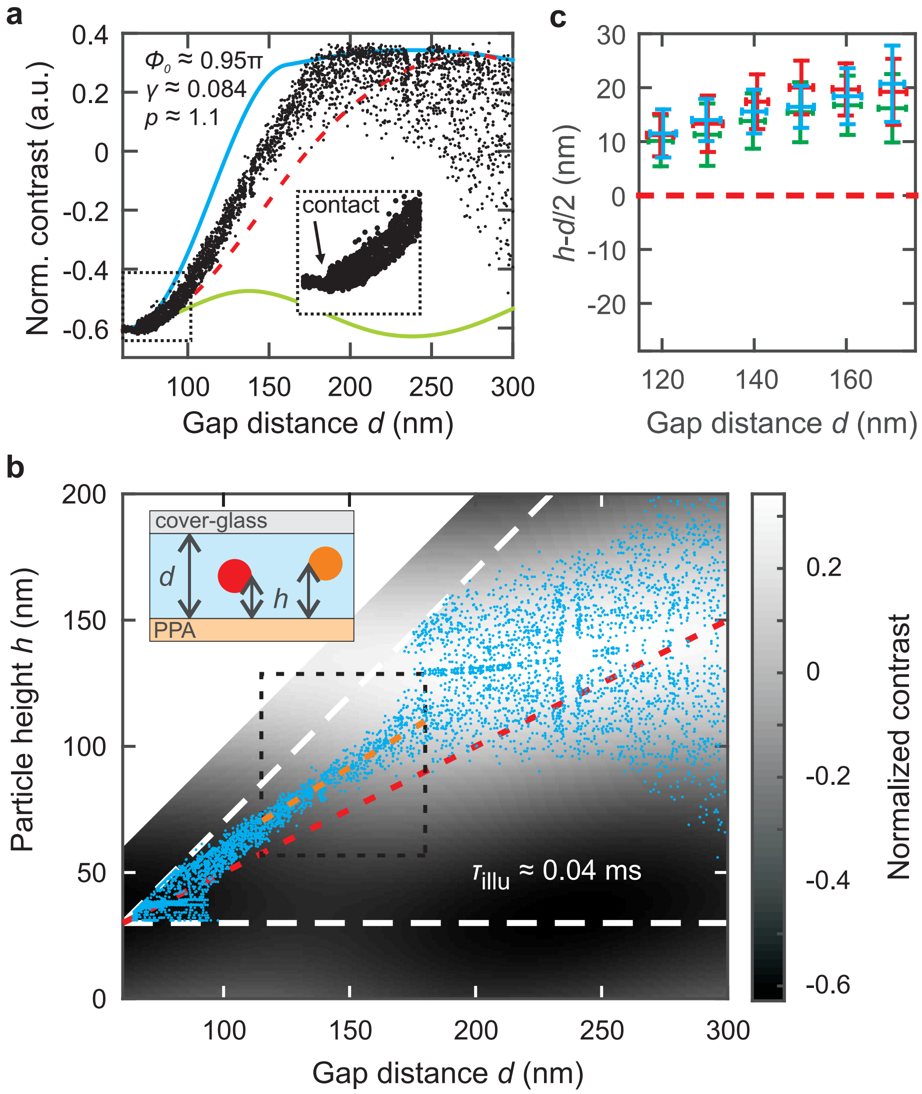

FIGURE 4.11: Measurement of the particle height in a $SiO_2$ (D263) - $H_2O$ - PPA slit. (a) Contrast signal of a 60 nm Au sphere (black dots), a simulated particle in the middle of the gap (dashed red line) and envelopes of simulated maximum (blue line) and minimum (green line) contrast for varying gap distances. The inset highlights the region where the particle is adsorbed on one of the confining surfaces. (b) Attributed particle heights (blue) are obtained by matching the measured (see panel a) and simulated contrast values (gray-scale image). The confining surfaces and the particle radius restrict the possible values (dashed white lines). The dashed red and orange curves indicate the height values corresponding to the center of the gap and to $h = 0.61d$, respectively. The inset schematically shows two 60 nm particles at height $h$ in the nanofluidic slit with gap distance $d = 150$ nm (to scale). (c) The averaged difference in particle height from the middle of the gap for the particle positions inside the dashed black box in panel b. The error bars are determined by the standard deviation of the measured gap distances and particle heights.

distance as a lookup table. The short illumination time of $\lesssim 40\,\mu$s is essential to measure almost instantaneous particle heights [105] and to obtain reliable height-distribution data. The periodicity of the contrast signal with particle height leads to either one or multiple possible solutions for the particle height. In the single-value range of $115\,\mathrm{nm} \leq d \leq 175\,\mathrm{nm}$ we determined the averaged deviation of particle height $h - d/2$ for three particles (see Figure 4.11 (c)). The deviation of the particle height from the gap center is always positive.

Physically, the average height of the negatively charged particles is determined by the relative repulsion of the particles from the like charged confining surfaces. A height above the center of the gap indicates a higher charge on the polymer surface, which does not contain sites that could dissociate. However, it is known that hydrophobic surfaces often attain a negative charge, most likely due to the preferential absorption of oxianions [119].

## 4.8 Conclusion

A new versatile setup for investigating the behavior of nano-objects in a tunable confinement between two surfaces has been developed. The interferometric detection setup allows us not only to detect the nano-objects with high sensitivity, but also to determine the 3D particle position and the wall separation *in situ* with nanometer spatial and millisecond temporal precision.

We have established a parametric model to describe the contrast measured by iSCAT imaging of individual particles in a tunable nanofluidic gap. The model describes the gap-height dependent signals detected from particles immobilized at the confining surfaces and obtained from individual diffusing particles with a consistent set of parameters. For the freely diffusing particles, the parameters are extracted from a measurement of the particle and background signal as a function of the nanofluidic gap distance. Two of the parameters are obtained from the envelope of the intensities recorded. The third parameter, i.e., the particle scattering phase, $\phi_0$, is obtained at small separations when the confinement of the particle is restricted to a height range of just a few nanometers.

As a result, the particle contrast is calibrated *in-situ* and the model parameters are obtained without further calibrations. In a range of gap distances the parameters can directly be mapped to a unique particle height via the model. Because of the periodic particle contrast as a function of particle height multiple solutions exist at larger gap distances of $d > 250\,\mathrm{nm}$. The accuracy of the height measurement is given by the accuracy of the gap-distance measurement, the errors in the parameter determination, and by the intensity fluctuations. We estimate an accuracy for the gap-distance measurement of $\lesssim 2\,\mathrm{nm}$ from the accuracy of the z-calibration and the laser noise. The error arising from the uncertainty in $\phi_0$ can be estimated from the statistics of the confined particle distribution to $\lesssim 4\,\mathrm{nm}$. The errors due to the parameters $\gamma$ and $p$, and from the intensity fluctuations can be estimated from the precision of matching the model envelope to the recorded data to a statistical error of $\approx 2\,\mathrm{nm}$ and a systematic error of about $\approx 2\,\mathrm{nm}$ at intermediate particle contrast values. Thus we estimate that absolute heights of the $60\,\mathrm{nm}$ gold spheres can be measured in the single valued contrast regions with an accuracy of $\approx 10\,\mathrm{nm}$ and a precision of $\approx 2\,\mathrm{nm}$ at intermediate contrast values. Naturally, the error increases significantly at the extremal values of the contrast signal.

We apply the measured particle height distribution to obtain the physical parameters of the system describing the interactions between particle and surfaces. For this we calculate the height probability distribution for the individual particles, which are directly connected to the free energy of the system. Here, the short illumination time of $\tau_{\mathrm{illu}} \lesssim 100\,\mu\mathrm{s}$ achieved by a single-pass laser scan per frame is critical to arrive at meaningful height values. Thus, the NCA allows us to observe the narrowing of the particle height distribution at increasing confinement. Consequently, the physical parameters of the system are obtained, i.e., the Debye length, and the surface potentials. Their values are in agreement with the values obtained from measurements of the mean zeta potential and literature values of the $SiO_2$ surface potential.

In another experiment we used the tool to measure the height and diffusion of $60\,\mathrm{nm}$ gold spheres as a function of absolute gap distance between the coverglass and PPA surface. We find that the particles localize more closely to the glass interface indicating a higher charge of the polymer surface.

# 5 Brownian motion of confined nanoparticles

The aim of the experimental work presented in this chapter is to investigate the diffusion of charged nanoparticles confined by two planar surfaces as a function of gap distance.

Large parts of this chapter are adapted from the article *"The Nanofluidic Confinement Apparatus: Studying confinement dependent nanoparticle behavior and diffusion"* [92] by me, Felix Holzner and Armin W. Knoll. The manuscript is submitted to *The Journal of Chemical Physics*.

All the experiments and the analysis of the data was done by me. Armin Knoll gave me valuable tips for the analysis and presentation of the results. The manuscript was written by me with the help of Armin Knoll. The manuscript was revised by Felix Holzner and proof-read by Charlotte Bolliger and Christian Schwemmer. Madhavi Krishnan contributed with fruitful discussions.

## 5.1 Introduction

A fundamental understanding of the motion of micro- and nano-scaled objects in nanofluidic confinement is important for many biological and technical processes such as the anomalous diffusion in cellular environments [94, 120], the delivery of drugs [121], the formation of colloidal crystals [122, 123], particle sorting [124], and directed self-assembly [125].

Nanofluidic systems in general are characterized by spatial distances in at least one dimension of less than 100 nm. This distance range interferes with several natural length scales of particle-surface interactions [93], such as the electrostatic interactions. The electrostatic interactions between charged objects and surfaces in a nanofluidic system decay approximately exponentially with separation and a characteristic length scale termed Debye length [126]. Experimentally, the gap-distance-dependent forces between two curved surfaces were studied in microrheology experiments [127, 128] and in detail using the surface force apparatus [56]. However, so far, most nanofluidic experiments involving confined particles have been performed using static surfaces and fixed geometries, which do not allow the degree of confinement to be varied *in situ*.

Recently it was demonstrated that the gap-distance-dependent electrostatic forces can be exploited to achieve geometry-induced trapping and manipulation of charged nanoparticles and vesicles in nanofluidic systems [54]. In a follow-up experiment, it was shown that crucial information on the trapping potential can be gained by using an AFM-type system and a micro-capillary to adjust the gap distance [129].

Another example of a strongly gap-dependent behavior is the lateral diffusion of particles in a nanofludic gap. In microfluidic systems, it has been shown that the theoretical predictions of hydrodynamically hindered diffusion are in agreement with the measured diffusivity of microparticles [72, 130]. However, in nanofluidic systems, a $50 - 70\,\%$ lower diffusion is observed when geometrical dimensions approach the Debye screening length [66, 103, 131]. The mechanisms that have been proposed to explain the increased hindrance are anomalous viscosity [131], anomalous diffusion [103] and an electroviscous effect [66].

Here, we will use the NCA to measure the gap distance dependent diffusion of nanospheres, which is enabled by the adjustability and detectability of the surface separation presented in the last chapter. Furthermore, in Section 5.2 it is demonstrated that, the setup is also capable of providing a constant gap distance, which is essential for measuring diffusion a particular gap distance. In Section 5.3 the lateral diffusion of $60\,\mathrm{nm}$ charged Au nanospheres as a function of confinement between the cover-glass and PPA surface is analyzed. We find a strong monotonic decay of the diffusion constant with decreasing gap distance. This result cannot be explained by pure hydrodynamic effects, including the asymmetric vertical position of the particles in the gap determined in Section 4.7. Instead we attribute it to an electroviscous effect. For strong confinement of less than $120\,\mathrm{nm}$ gap distance, we detect an onset of sub-diffusion which can be correlated to a motion of the particles along high-gap-distance paths.

## 5.2 Measurement and stability of the gap distance

The diffusion of confined particles can be studied by measuring their displacement as a function of time. In order to assign to each measurement an exact gap

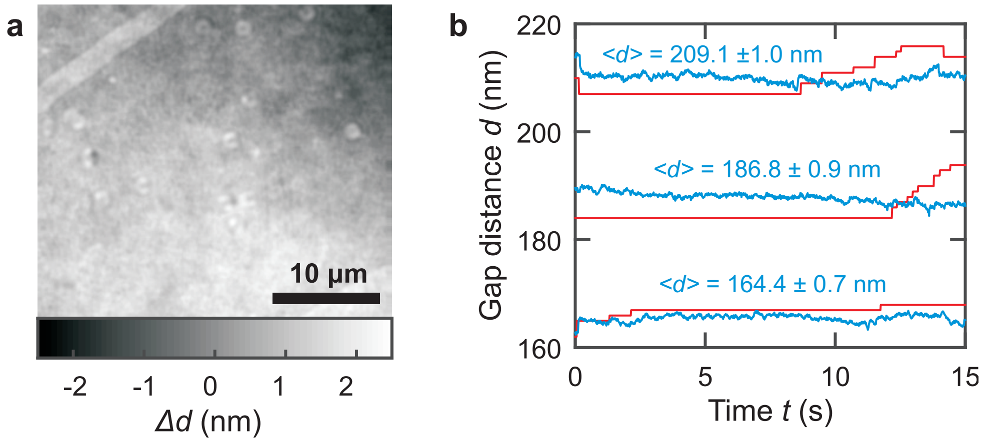

FIGURE 5.1: (a) Effective gap distance variation $\Delta d$ in the nanofluidic slit obtained from the local variation in optical path difference. (b) The height of the cover-glass (red) is adjusted by a feedback loop to ensure a constant gap distance (blue) during experiments.

distance it is important that the lateral and temporal gap distance variations are small. The parallelization and determination of local gap distance is done by using the method described in Section 4.4.

The substrate used in this chapter consist of a 175 nm thick PPA film, which was spin coated onto a silicon sample covered with a 52 nm thick layer of a cross-linking polymer to increase the adhesion (for details see Section 3.2.2). The thicknesses were measured with AFM. The refractive indices $n_{HM} = 1.67$ and $n_{PPA} = 1.59$ were measured by ellipsometry. The optical path difference between cover-glass and substrate varies because of the inherent surface roughness of the contributing interfaces. This fact leads to a varying phase shift of the interference signal pixel by pixel. AFM measurements yield the following root-mean-square (RMS) roughnesses: $S_q^{\mathrm{D263}} \approx 0.4$ nm for the cover-glass, $S_q^{\mathrm{PPA}} \approx 0.3$ nm for the polymer surface and $S_q^{\mathrm{Si}} \approx 0.2$ nm for the silicon wafer. Since the silicon wafer is relatively flat and the refractive indices of polymer and glass are similar we approximate that all the phase differences originate from a roughness in the cover glass. The conversion from the phase shift to the gap distance is performed using the optical model mentioned in Section 4.4, using the thickness and refractive indices of the polymer layers mentioned above. The resulting gap distance image Figure 5.1 (a) reveals a remnant tilt between the two confining surfaces, which could be corrected further. Without this correction, we achieve a height difference of 3 nm over a distance of 30 $\mu$m. The standard deviation of the plane corrected gap distance image is $S_q^{\Delta d} \approx 0.6$ nm, which is consistent with the measured surface roughness values.

We will now analyze the temporal mechanical stability of the NCA. During the measurements described in the subsequent sections, thermal drift and pressure changes may lead to a deflection of the relatively compliant cover-glass. These deflections are compensated by implementing a closed-loop feedback system that registers changes in the background interference intensity and adjusts the height of the cover-glass to keep the intensity constant at a frequency of 20 Hz. The performance of the feedback-loop is illustrated in Figure 5.1 (b), where 15 s of stability data were acquired for three different gap distances. For each gap distance, the observed accuracy was 1 nm or better. This duration is already sufficient for measuring the lateral confined diffusion, but the system has been tested to keep the confinement constant for several hours.

## 5.3 Confined lateral diffusion of nanospheres

In this section the lateral diffusion coefficient of 60 nm gold spheres is determined by measuring the mean squared displacement (MSD) of the particles as described by Equation (2.19). Due to diffraction, it is not easy to identify the correct positions of two or more particles in close proximity. Therefore, we set the concentration of the colloid such that for gap distances $d$ between 200 – 300 nm, on average $23 \pm 5$ particles per frame are detected, whereas for higher confinements with $d \lesssim 200$ nm only $8 \pm 3$ particles are detected. The high frame rate (800 FPS) nevertheless provides a sampling of 60,000 up to 300,000 particle positions for each 15 s measurement. The particle illumination time in this experiment was $\tau_{\text{illu}} \lesssim 40\,\mu$s as explained in detail in Section 3.1.2.

For each gap distance $d$, we obtain the one-dimensional (1D) time and ensemble averaged MSD for a range of time steps $\Delta t$ from $1.25 \leq \Delta t \leq 31.25$ ms (see Figure 5.2 (a)). A strong decrease of the diffusivity with decreasing gap distance is apparent. Fits of Equation (2.21) to the MSD in the $x$- and $y$-directions are given as solid lines. The fit parameter $\alpha$ indicating sub-diffusion for $\alpha < 1$ is shown in Figure 5.2 (b). At a confinement $d < 120$ nm, a scale-dependent diffusion coefficient is observed. This effect has been attributed to the presence of lateral obstacles preventing a free diffusion of the particles [132]. In our case however, these obstacles are either induced by local charge inhomogeneities or by the roughness of the confining walls.

We use a simplified picture of a sphere confined by two like charged surfaces as described in Section 2.1.2 to assess this hypothesis. In Equation 2.15 the overall electrostatic interaction energy of a sphere between two walls is obtained by the sum of the interaction energies to each wall. Assuming a surface potential of the sphere of $-58$ mV (see Section 3.2.3) and a surface potential of the walls of $-67$ mV as determined for silicon oxide by Behrens *et al.* [60], we obtain a change

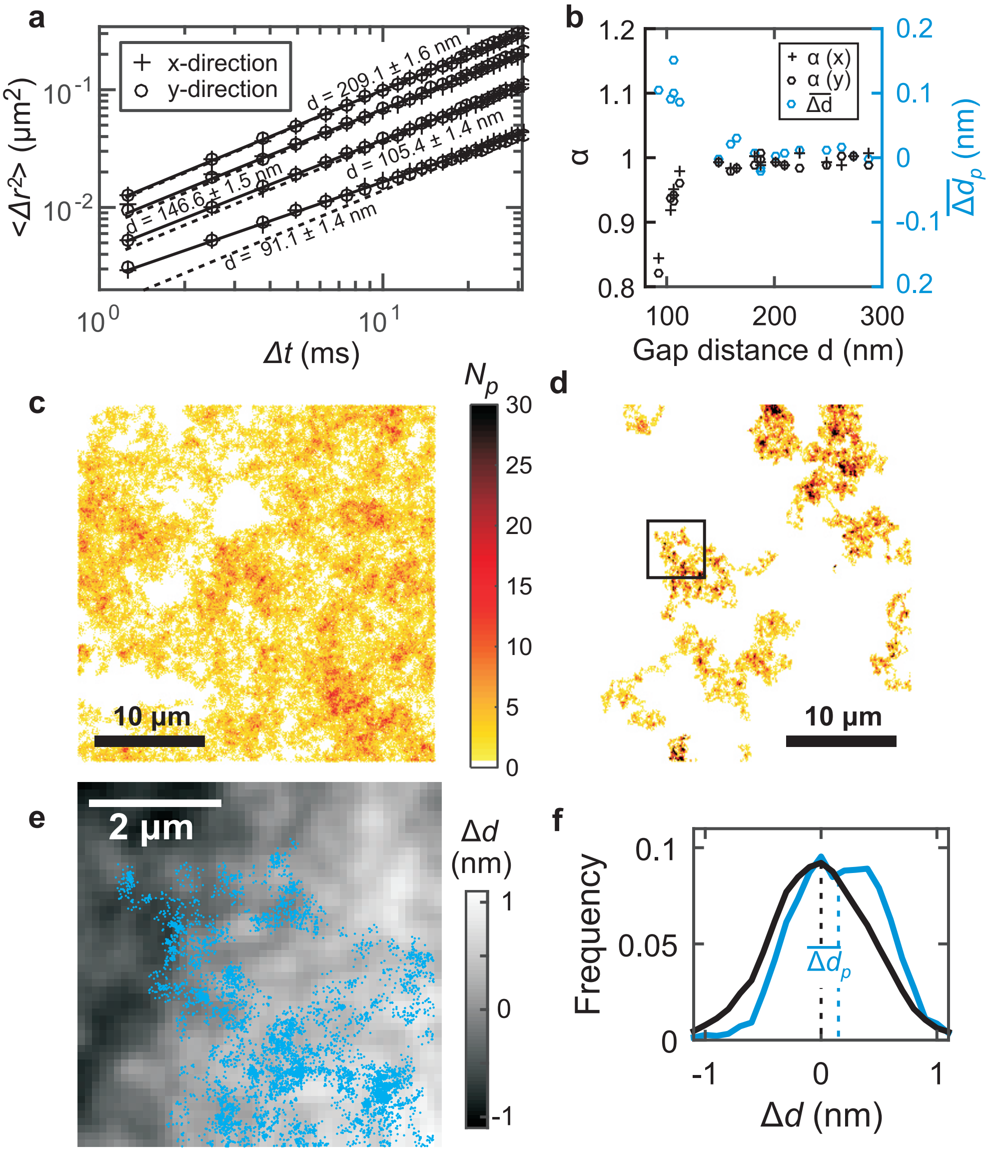

FIGURE 5.2: (a) Measurements of the lateral MSD in the $x$- and $y$-direction at four different gap distances $d$. The solid and the dashed lines indicate fits of Equation (2.21) to the data for anomalous and normal diffusion, respectively. (b) The parameter $\alpha$ indicates the degree of normal diffusion $\alpha = 1$ and sub-diffusion $\alpha < 1$ (black symbols). An average value of the $\overline{\Delta d_p} > 0$ (see panel f) indicates that particles avoid narrow gap regions (blue circles). (c,d) Number of detected particles $N_p$ in a $100\,\mathrm{nm}$ grid during a $15\,\mathrm{s}$ measurement at an average gap distance of (c) $d = 210.0 \pm 1.0\,\mathrm{nm}$ and (d) $d = 105.9 \pm 1.0\,\mathrm{nm}$. (e) Gap distance modulation $\Delta d$ and detected particle positions (blue dots) for the area indicated by the black box in panel d. (f) Histograms of the gap distance modulation (black line) and for the locations of the gap distance modulation sampled by the particles (blue line).

in interaction energy of $\approx 0.8\,k_BT$ at a gap distance of $120\,$nm and a gap distance modulation of $1\,$nm. The simple model corroborates the interpretation that the observed RMS roughness of the glass of 0.4 nm provides significant energy barriers for diffusion. We note, however that the same effect could be induced by a charge modulation of the surface potential (or correspondingly the surface charge) by $\approx 5\%$.

To further investigate the origin of the obstacles we analyzed the time-averaged lateral particle distribution and its correlation to the measured locally resolved gap distance variation $\Delta d$ (see Figure 5.1 (a)). To obtain a measure for the particle distribution, we divide the field of view into a $100\,$nm grid and count the total number of particles visiting each grid section for all frames. The resulting histograms are visualized as "heatmaps" in Figure 5.2 (c,d) for an average gap distance of (c) $d = 209.1 \pm 1.0\,$nm and (d) $d = 105.4 \pm 1.0\,$nm. The particles are quasi uniformly distributed over the entire field of view for the larger separation and are more localized in the narrower slit.

In order to correlate the detected particle trajectories with the gap distance modulation $\Delta d$, see Figure 5.1 (a), we have to compensate for the tilt in the gap distance map. Therefore, we divide the map into squares of $5 \times 5\,\mu$m$^2$ size, roughly corresponding to the 1D diffusion length during the measurement of $r_{\text{diff}} \approx 5\,\mu$m, and correct for the offset in local gap distance modulation $\Delta d$ for each square. For example, Figure 5.2 (e) shows $\Delta d$ and the positions of a single diffusing particle (blue dots) for the square given by the box in Figure 5.2 (d). According to this trace the particle samples certain locations of the $\Delta d$ map and we term the range of sampled values $\Delta d_p$. The average histograms of $\Delta d$ and $\Delta d_p$ for all squares are shown in Figure 5.2 (f) as black and blue lines, respectively. Clearly, the particles prefer to be located at a position having a larger gap distance. To obtain a qualitative measure of the strength of this effect, we determined the distance of the center of mass of the two histograms $\overline{\Delta d_p}$ for all measured gap distances, see Figure 5.2 (f). The result is given in Figure 5.2 (b) by the blue circles. For gap distances below $d = 120\,$nm, a significant shift of the particle position into high-gap-distance positions is apparent. This behavior is qualitatively similar to the onset of sub-diffusion measured for the MSD. Therefore, we conclude that the sub-diffusion is indeed caused by the fact that the particles start to avoid regions with narrower gap distances.

Finally, we turn to the central result, the gap-distance-dependent lateral diffusion coefficient $D_{||2}(d)$, which is depicted in Figure 5.3. The predicted diffusion coefficients accounting for hydrodynamic hindrance from two walls are also shown for the LSA [Equation (2.26) (solid lines)] and CSA [Equation (2.27) (dashed lines)].

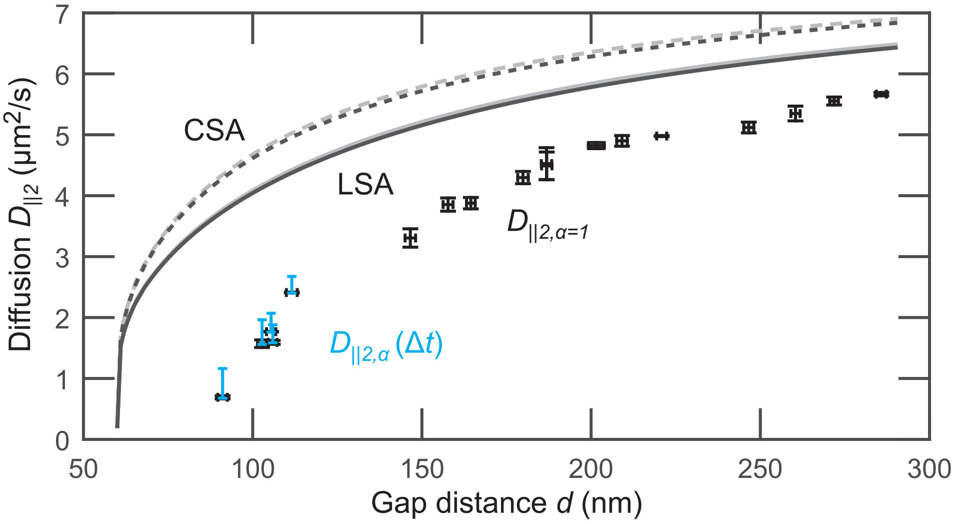

FIGURE 5.3: Lateral diffusion coefficient for varying gap distance in a nanofludic slit. The error in $D_{||2}$ and $d$ are determined by the standard deviation of $D_{||2}$ in x and y direction and the standard deviation of $d$, respectively. The time dependent diffusion coefficient $D_{||2,\alpha}(\Delta t)$ is plotted for the time steps $\Delta t = 1.25\,\text{ms}$ and $31.25\,\text{ms}$ by the light and dark blue lines, respectively. Theoretically predicted diffusion coefficients by LSA (solid lines, Equation 2.26) and CSA (dashed lines, Equation 2.27) are shown for an average particle height at $h = 0.5d$ (gray) and $h = 0.61d$ (black).

According to Equation (2.22)-(2.27), the height $h$ of the particles influences the magnitude of the hindered diffusion. To quantify the effect, we will determine the height for an individually diffusing particle from its contrast. The average relative height of three individual particles is almost constant at $h/d = (0.61 \pm 0.02)$.

Both approximations were calculated for a particle diffusing at a measured height $h = 0.61d$ (black) and in the middle of the slit $h = 0.5d$ (gray). The asymmetric height leads to merely $1.5\%$ lower diffusion constants and cannot explain the $20 - 50\,\%$ lower diffusivity measured. We also exclude that the localization due to surface roughness is the predominant factor for this reduction, because pronounced sub-diffusion is only observed for gap distances of $d < 120\,\text{nm}$.

In bulk, the electroviscous effect is attributed to the surface charge of the particles and leads to an increased effective viscosity and thus to a reduction in particle diffusion [133]. A similar mechanism should also play a role in a nanofluidic system, in particular when a particle is close to a charged wall. Whereas diffusion measurements for uncharged particles [72] and for particles in electrolyte with higher ionic concentration [105] are in agreement with predictions that consider only a hydrodynamically hindered drag, there is considerable evidence of an increased drag of charged particles near charged walls in a weak electrolyte [66, 134]. In a similar experimental configuration Eichmann *et al.* [66] measured a $\approx 30\,\%$ ($\approx 55\,\%$) lower lateral diffusion coefficient for $60\,\text{nm}$ ($100\,\text{nm}$) gold nanospheres with a relative radius of $\kappa a \approx 0.9$ ($\kappa a \approx 2.1$) and a relative glass-particle distance of $\kappa h - \kappa a \approx 4.5$ ($\kappa h - \kappa a \approx 3.6$). These values are in agreement with the $\approx 45\,\%$ lower diffusion we measure for $\kappa a \approx 3.4$ and $\kappa h - \kappa a \approx 4$.

## 5.4 Conclusion

In this chapter we have measured the diffusion of $60\,\text{nm}$ gold spheres as a function of absolute gap distance between the cover-glass and PPA surface. A diffraction limited resolved map of the sub-nanometer-resolved gap distance can be obtained from the background signal. We find that sub-diffusion becomes significant at gap distances below $d = 120\,\text{nm}$. We demonstrate that this scale dependent diffusion is correlated to particle trajectories that avoid regions of narrow gap distances caused by the surface roughness of the confining surfaces. The measured lateral diffusion coefficients are $20 - 50\,\%$ lower than predicted by purely hydro-dynamical hindrance, also when taking their asymmetric position in the gap into account. Similarly, the observed scale dependent diffusion cannot account for the effect because it is only significant for small gap distances. We conclude that electro-viscous effects are the main cause for the observed reduction in diffusivity. Our measurements provide a detailed information on the gap-distance-dependent particle diffusion, which may form the basis for testing theories describing the electro-viscous effect. In general, the results shown here demonstrate the versatility of the tool which allows one to measure nanoparticle behavior as a function of confinement in remarkable detail.

# 6 Nanofluidic Brownian Motors

In this chapter, we will demonstrate that nanoparticles can be transported along quasi 1D transport paths by employing a rocked Brownian motor.

Parts of this chapter are adapted from the article "*Nanofluidic Brownian Motors*" by Michael J. Skaug, me, Colin D. Rawlings, Christian Schwemmer and Armin W. Knoll. The manuscript is not yet submitted.

The tSPL patterning of the ratchets was done collaboratively by Armin Knoll, Colin Rawlings, and me. Most of the experiments and the tracking of the particles were carried out by me and with the support of Christian Schwemmer. The code for the drift analysis of the experiments was written in large parts by Armin, Michael J. Skaug and in small parts by me. Christian Schwemmer and Colin Rawlings provided analytical and finite element (FEM) simulations of the drift speed and the interaction potential, respectively. A first draft of the manuscript was written by Michael J. Skaug and is currently continued by Armin Knoll.

## 6.1 Introduction

The controlled transport of nano-scaled objects through nanofluidic systems has potential applications in concentrating and sorting of particles and molecules, control of chemical reactions, or drug delivery and discovery [93, 135, 136].

Brownian motors have demonstrated efficient transport of colloidal particles up to the point of benefiting from thermal motion [137]. Ingredients of such a Brownian motor are a spatially asymmetric potential landscape and an external driving force to bring the system out of equilibrium. Experimentally, most of the Brownian motors have been demonstrated with the concept of periodically switching an asymmetric potential on and off [138–141]. However, this so called flashing ratchet typically allows only drift speeds of a few microns per second, since the drift is limited by the diffusion of the particles. Two orders of magnitude larger drift velocities have been reached for 3 $\mu$m sized particles by applying an oscillating driving force [77]. The authors claim that the necessary asymmetric potential is created by an dielectrophoretic effect and that the oscillating electric field tilts this potential at the same time due to

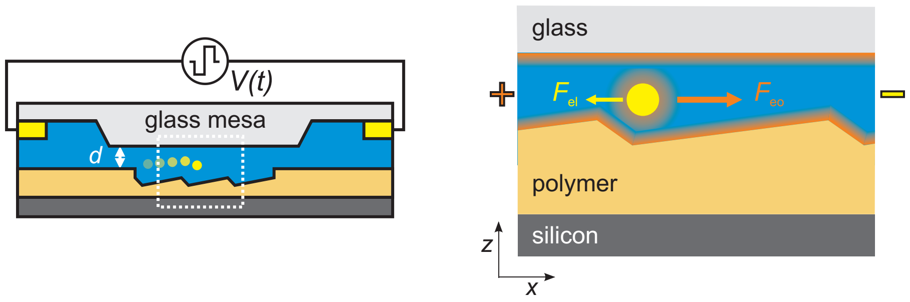

FIGURE 6.1: Brownian motor realized by rocking a topographically defined ratchet. Schematic cross sections of a 60 nm gold sphere in a nanoflidic slit confined by a glass surface and a polymer surface with a ratchet topography. The particle experiences a spatially asymmetric potential landscape, due to the electrostatic interactions of the counter ions (depicted in orange) from the particle and the like charged surfaces. A square wave potential $V(t)$ is applied between two electrodes to drive the system out of equilibrium, which exerts an electro-osmotic force via the ions in the diffuse layer ($F_{eo}$) and an electrophoretic force on the surface charge of the particle ($F_{el}$). For our system the counteracting forces are dominated by the electro-osmotic force. Please note that only the right panel is true to scale.

electrophoresis. Yet, the break down of the drift at high frequencies is not fully understood and restricts the accessible drift speeds. A complete understanding of the involved potentials is of essential importance; otherwise one can draw the conclusion that an observed transport process is caused by a ratchet effect although it was only convection [142].

In our implementation we exploit the well understood electrostatic interaction potential between charged 60 nm gold-nanospheres and the like charged confining surfaces in a nanofluidic slit (see Section 2.1.2). The schematic in Figure 6.1 depicts such a sphere confined in our NCA by the cover-glass and a $\approx$ 200 nm thick polymer layer. Please note that the left schematic is not true to scale, the glass mesa and the patterned ratchets have a typical width of $\approx 150\,\mu$m and $\approx 10\,\mu$m, respectively. A static asymmetric potential landscape is shaped by patterning a 3D ratchet topography into the PPA film using thermal scanning probe lithography (tSPL, see Section 3.2.2). The interaction potential can be fine tuned *in-situ* by changing the gap distance $d$ between the cover-glass and the polymer film. The repulsive forces acting on the particles are increased with increasing overlap of the double layers between the particle and the confining surfaces. In order to bring the system out of equilibrium a zero mean AC electric field is applied via electrodes, which are separated by $\approx$ 1.2 mm (see Figure 3.4). The electric field exerts an electro-osmotic force $F_{eo}$ on the particle via the counter-ions in the diffuse layer in one direction and an electrophoretic force $F_{el}$ on the surface charge of the particle in the other direction. At low frequencies we observed that the negative charged particles move towards the negative charged electrode, from which we conclude that the electro-osmotic force is dominating the electrophoretic force.

In Section 6.2 both, the asymmetric ratchet potential and the drift velocity are analyzed for linear ratchets in dependence of confinement distance, field strength and frequency. In Section 6.3, we demonstrate that the particles can also follow curved transport paths along arbitrary directions and that the transport direction can be reversed by simply changing the applied driving frequency.

## 6.2 Linear transport paths

Figure 6.2 (a) shows the topography of four linear ratchets, which are patterned into a PPA film. The ratchets r1 and r3 are designed to transport the particles in positive x-direction, while ratchets r2 and r4 should transport them in the opposite direction. Small reservoirs connect the two ratchet types, such that the particles will move in a loop. The ratchets are recessed by $\approx 50\,\text{nm}$, such that an energy barrier prevents the particles from leaving the transport paths. For each ratchet the cross-section averaged over all teeth is shown in Figure 6.2 (b). On average, the ratchets have a depth modulation of 40 nm and a width of 300 nm. The periodicity of the ratchets is 550 nm with an asymmetry of approximately 20:80.

### 6.2.1 Asymmetric potential landscape

A droplet of $\approx 30\,\mu\text{l}$ of a 1:18 diluted 60 nm gold colloid was placed on the patterned PPA film. Based on the degree of dilution and conductivity measurements presented in Section 3.2.3, we estimate a Debye length of $\kappa^{-1} \approx 12\,\text{nm}$. The gap distance between the PPA surface and the cover-glass was then adjusted to $\approx 150\,\text{nm}$. Under such conditions, the distance between the confining surfaces and the surface of a particle is only a few times $\kappa^{-1}$, which prevents the particles from escaping from the recessed structure but allows them to overcome the potential barrier of the ratchets within a few seconds. We waited until all particles diffused either out of the field of view or to our recessed structures before we recorded a sequence of images at a frame rate of 1000 FPS for 20 s. The overlaid color plot in Figure 6.2 (a) shows a heat map of detected particle positions in a grid of $10\,\text{nm}^2$. Because of the short particle illumination time of less then $40\,\mu\text{s}$ the particles' diffusion length during the illumination is on average less than $< 20\,\text{nm}$ (see confined lateral diffusion in Section 5.3). Therefore, the

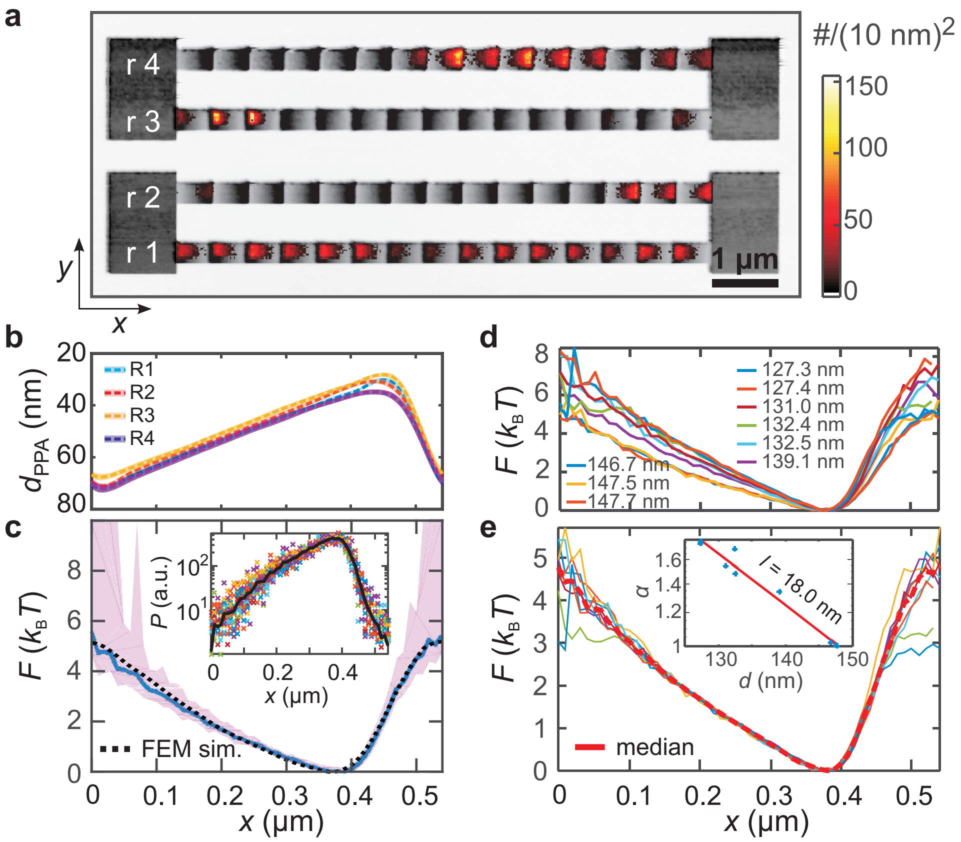

FIGURE 6.2: (a) Scanning probe topography image of four ratchets connected by four reservoirs patterned into the PPA surface by tSPL. The number of detected particles per $10\,\mathrm{nm}^2$ is overlaid in color. The particle distribution was measured within 20 s while no voltage was applied ($|V| = 0$). (b) Averaged cross-section of a ratchet tooth for the four ratchets. In order to compare the profiles, the ratchets r2 and r4 are plotted in reverse direction $d_{PPA}(-x)$. (c) The average 1D free energy $F$ (blue line) is determined by using the the Boltzmann relation $F(x) = -k_B T \ln P(x)$. The average empirical probability distribution $P(x)$ (black line in the inset), which is the average of normalized and overlayed histograms for each ratchet-tooth in (a). The shaded region marks the standard deviation of the free energy. (d) The average free energies at various gap distances are (e) scaled such that they all collapse onto a master curve (dashed red line). The scaling parameter $\alpha$ decays exponentially ($l = 18.0\,\mathrm{nm}$) with the gap distance.

detected particle positions can be used to determine empirical probability profiles by averaging the histograms across the y-direction. For a large number of trials does the empirical probability distribution converge to the true probability distribution $P$. In each frame on average 5 out of 6 particles are located in a ratchet and one is located in a reservoir, which makes in total $\approx 100,000$ particle positions in a ratchet. Since the topography of the ratchets varies only marginal, we break the profiles at the periodic potential barriers into segments and overlay the histograms using cross-correlation. The result is shown in the inset of Figure 6.2 (c), where the average is denoted by the black line. We estimate the average particle free energy $F(x)$ in the ratchet potential as depicted by the blue line in Figure 6.2 (c) by using the Boltzmann distribution

$$P(x) \propto \mathrm{e}^{-F(x)/k_B T} \tag{6.1}$$

and the average empirical probability distribution. The shaded region around the curve marks the free energy obtained from the $1\sigma$ standard deviation of empirical probability distributions for the individual ratchet segments.

Experimentally, the empirical probability distribution was measured at various gap distances for a similar number of particle positions. Even at the tightest used confinement ($d = 127\,\mathrm{nm}$), particles were still capable of overcoming the potential barriers of the ratchet, but the transition rate was much lower. The measured free energy profiles are shown in Figure 6.2 (c), which all have a similar shape.

The similarity becomes apparent when we take a look at the plane-sphere-plane interaction energy in Equation (2.15) and assume that the particle is in thermal equilibrium i.e. located in the middle of the gap. Then the ratio of the interaction energies for two gap distances is given by $W_{PSP}(d_1)/W_{PSP}(d_2) = \mathrm{e}^{-\kappa d_1/2}/\mathrm{e}^{-\kappa d_2/2}$. A simple calculation for asymmetric surfaces, also assuming that the particle is located at the energetic minimum, yields the same linear dependency

$$\log\left(W_{PSP'}(d_1)/W_{PSP'}(d_2)\right) = -\kappa\frac{d_1 - d_2}{2} + \mathrm{const}, \tag{6.2}$$

where the constant only depends on the effective surface potentials of the particle and the two surfaces. Therefore, we determine a master curve from the averaged free energy profiles and scale the individual profiles until they best match this master curve, as depicted by the colored and red lines in Figure 6.2 (d), respectively. From the scatter of the scaling parameters for various gap distances, as shown in the inset, we observe a exponential decay with the gap distance with a decay length of $l \approx 18.0\,\mathrm{nm}$. However, FEM simulations have shown that an assumed particle position in thermal equilibrium cannot be used to determine the

Debye length. To get the full lateral probability distribution one has to integrate the occupied positions along the z-axis. For surface potentials of $\psi \approx 60\,\mathrm{mV}$ and an input Debye length of $\kappa_{real}^{-1} = 15\,\mathrm{nm}$ the simple model would provide a $\approx 25\,\%$ larger Debye length. This would also partially explain the deviation from the Debye length estimated by conductivity measurements in Table 3.2.

### 6.2.2 Fluctuating forcing

In the last section, we observed that the 60 nm gold spheres confined at a gap distance $125\,\mathrm{nm} \lesssim d \lesssim 150\,\mathrm{nm}$ were capable of overcoming the asymmetric potential barriers within several seconds, but the mean particle drift without a periodic fluctuating force was zero. Yet, with an applied unbiased ±3 V square wave potential at a frequency of 10 Hz the particles move as depicted by the two time dependent trajectories in Figure 6.3 (a). The black arrows point in the usual ratchet direction (climbing the shallow slope), which is in the same direction as the effective motion of the two particles. Within less than a second the two particles have moved counter clockwise back to the starting reservoir. Despite of the speed, there is a small backward motion of the particles indicated by the white arrows, which reduces the total drift velocity $v$. Intuitively, one could expect that the net velocity of the particles can be increased by either increasing the height of the potential barriers or fluctuating the driving force with a higher frequency, but due to thermal noise this is not the case as indicated by Figure 6.3 (b, c). Neither a reduction of the gap distance $d$, which increases the height of the potential barriers (see Section 6.2.1), nor an increase in frequency (green empty circles) increases the average drift of the ratchets. We used the particle trajectories of 15 s long measurements and estimated the absolute particle drift in x-direction $|v_x|$ by a linear fit of Equation (2.31) to the mean displacements $\langle \Delta x \rangle$ of particle positions within the ratchets for time steps $\Delta t = t_2 - t_1$ between 1 ms and 200 ms.

The drift in Figure 6.3 (b) seems to saturate and is probably close to a maximum around $d \approx 150\,\mathrm{nm}$, since it should approach zero for very large and small gap distances. The last parameter which strongly affects the drift speed is the amount of applied fluctuating force. To avoid the risk of overdriving the ratchet at an applied potential of 4 V and 5 V, we first reduce the gap distance to $\approx 130\,\mathrm{nm}$ and measure three sets of drift speed versus frequency as depicted by the gray filled circles in Figure 6.3 (c). Comparison of the three sets indicates that the maximum drift speed is shifted towards higher frequencies with increasing applied forcing. The largest measured drift is almost $50\,\mu\mathrm{m/s}$ at a forcing of 5 V and 35 Hz.

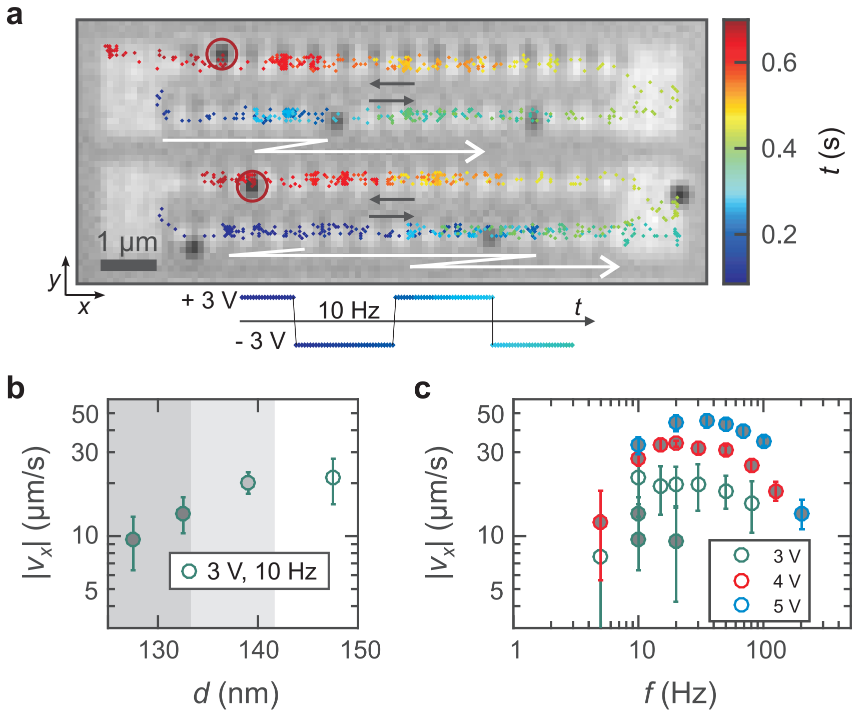

FIGURE 6.3: (a) The iSCAT image shows both the 60 nm gold particles and the topography of the ratchet and the reservoirs at a gap distance of $d \approx 148$ nm. The colored dots depict the detected positions of the two particles marked by the red circles over time $t$, while driving the ratchet with an applied 10 Hz AC 3 V electrostatic potential in x-direction. The net particle motion follows the direction dictated by the ratchets as depicted by the white and black arrows, respectively. (b) The mean absolute drift velocity $|v|$ of the particles versus gap distance $d$, averaged for the four ratchets. (c) Drift velocity as a function of driving frequency for different gap distances and applied voltages. The shading of the gray filled circles has the same meaning as in (b); dark gray filled circles were measured at a gap distance between 125 nm $\lesssim d \lesssim$ 133 nm whereas circles with a white filling were measured at 142 nm $\lesssim d \lesssim$ 150 nm. (b, c) The error bars are the standard deviation of the drift speeds measured for the four ratchets.

## 6.3 Curved transport paths

In the last section we showed that the ability of 3D patterning the ratchet provides us the freedom to design tracks along which the particles are guided. In this section, we will demonstrate that these tracks can be curved almost arbitrarily and that the drift direction can be reversed by switching to very fast driving frequencies as predicted by theory [78].

The gray scale images in Figure 6.4 (a) shows the topography of several curved ratchets, which form the letters IBM and are patterned into a PPA film. The typical cross section of a ratchet is shown in Figure 6.4 (b). In Figure 6.4 (a) the scatter of colored dots is overlayed, which depicts the spatio-temporal distribution of 60 nm gold spheres, while driving the ratchet at a gap distance of $d \approx 140$ nm. For clarity, only the longest trajectories per ratchet are shown and they end when either the particle has completed an entire loop or the tracking algorithm looses a particle. This happens in case a particle contrast is below a certain threshold or the point spread functions of two particles have a significant overlap. The starting position of each trajectory and the direction of particle motion is indicated by the colored arrows. All particles move along the usual ratchet direction (black arrows), while applying a $\pm 3$ V square wave potential with a frequency of 30 Hz in the x-direction and the same signal, but phase delayed by 90° in the y-direction as shown in Figure 6.4 (c). The phase shift leads to a diagonal electro-osmotic force, which rotates counter clock wise in the x-y plane as depicted by the black arrows. Apparently, a driving force rotated by 45° is sufficient to drive the particles forward (climbing the shallow slope) in either x- or y-direction, while the backward motion (climbing the steep slope) is still sufficiently suppressed when the electro-osmotic force acts in the diagonal backwards direction. The influence of the counter clock wise rotation of the driving force becomes obvious when taking a closer look at the particle positions in proximity of the curved black arrows in Figure 6.4 (a). A larger spacing of the particle positions indicates a faster drift, which can be observed when the curvature of the transport path is also counter clock wise.

A completely different particle transport behavior can be observed when the frequency is increased to 500 Hz as shown in Figure 6.4 (d). Although most trajectories are shown for a similar or longer duration as in Figure 6.4 (a) the transported distances are much shorter. In the cases where the particles have traveled a significant distance only a motion in the reverse ratchet direction is observed as indicated by the colored and black arrows, respectively.

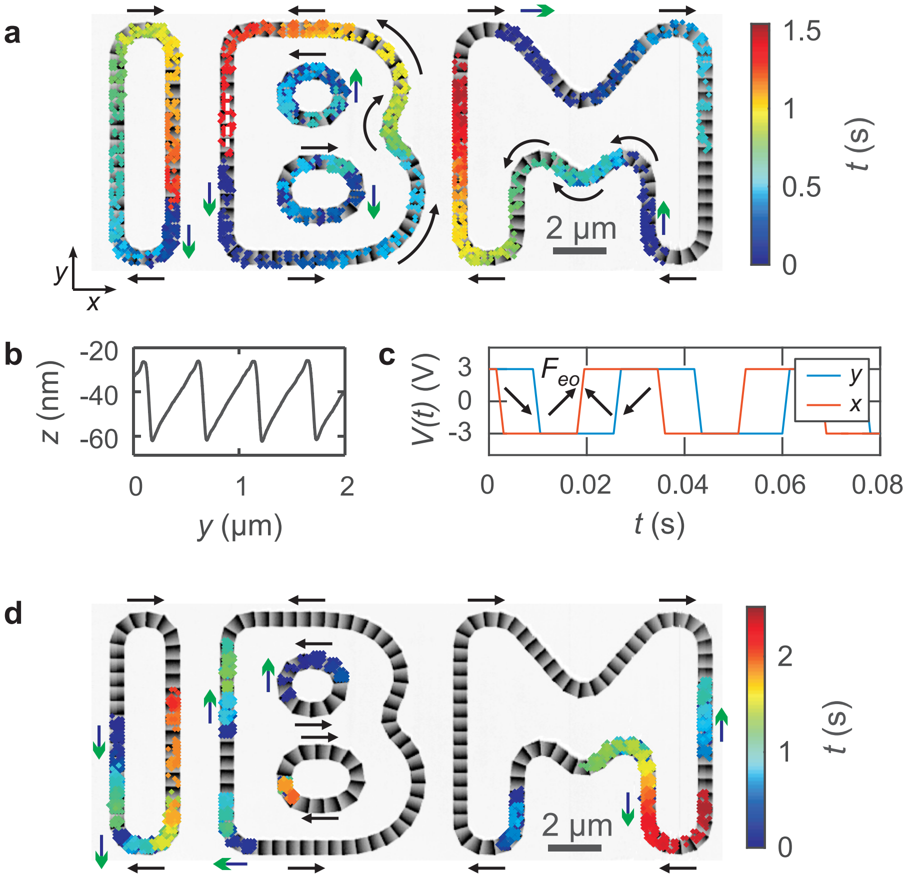

FIGURE 6.4: (a, d) Detected particle positions are depicted by colored dots, which are overlayed with the measured topography of several curved transport paths. Each trajectory starts at the time $t = 0\,\mathrm{s}$ and the color changes with the elapsed time. The trajectories end when the tracking algorithm looses a particle or when the particle has moved an entire loop. The black arrows indicate the usual direction while driving the ratchet and the colored arrows indicate the direction of mean particle current for several trajectories. The ratchets are driven by applying a squared wave potential in x- and y-direction with a phase difference of 90° at a gap distance of $d \approx 140\,\mathrm{nm}$. The applied potentials are (a) $\pm 3\,\mathrm{V}$ at $30\,\mathrm{Hz}$ and (d) $\pm 3\,\mathrm{V}$ at $500\,\mathrm{Hz}$. (b) Cross-section of the ratchet measured along the dashed white line in panel (a). (c) The applied $30\,\mathrm{Hz}$ potentials to drive the ratchet in panel (a). The electro-osmotic flow of the counter-ions in the electrolyte drags the particles in the x-y-direction indicated by the black arrows for the coordinate system shown in (a).

## 6.4 Conclusion

In this chapter we have demonstrated the first controlled transport of nanoparticles by means of a nanofluidic rocking ratchet. The patterning of the surface topography, which translates under confinement into an asymmetric static energy landscape has a big advantage compared to existing approaches, which rely on optical or dielectrophoretic forces, since those forces scale unfavorably with the volume of the particles and additionally require a constant energy input.

Furthermore, we were able to measure the induced gap distance dependent asymmetric ratchet potential due to the high spatial and temporal resolution of our detection system and we were able to estimate the screening of the interaction energy. We identify the electro-osmotic force as the dominant part of the driving force. The oscillating electric field induced a plug flow, which drove the particles in the ratchet, but on average no fluid was displaced. The particles can be transported and concentrated at a particular location and osmotic pressure of the particles is the only force which tries to redistribute the particles. For linear transport paths we characterize how the drift velocity depends on gap distance, applied potential and frequency. In our experiments, we observe a net drift of up to $50\,\mu$m/s along a direction dictated by the ratchet geometry. At the measured gap distances the particle drift is decreasing for frequencies in $\gtrsim 50\,$Hz and it is shown that the direction of particle drift can be reversed using an fluctuating force of $\approx\ 500\,$Hz. Also the transport of nanospheres along ratchets curved into arbitrary directions is demonstrated by applying a rotating electrical field.

# 7 Particle assembly by tunable confinement

The aim of the experimental work presented in this chapter is to confine the motion of diffusing nanoparticles and to assemble them at particular locations with high spatial resolution.

The tSPL patterning of the traps has been done by Colin Rawlings, Armin Knoll and me. The data acquisition of the assembly of the 60 nm gold spheres was done by Christian Schwemmer and me. All the other experiments as well as the data analysis was performed by me. The InAs nanowires were grown by Heinz Schmid. Ute Drechsler, Steffen Reidt and Meinrad Tschudy helped me with the fabrication of the electrodes.

## 7.1 Introduction

In the introduction of this thesis several synthesized nanoparticles with beneficial properties were mentioned and it was pointed out that their assembly would affect the fields of electronics, chemistry and biology. Furthermore, several assembly techniques were reviewed in Section 1.1 and we observed that the methods which provide a high control over the placement of individual particles handle the particles in solution, and provide independent trapping and deposition steps. Therefore, we will take a closer look at the different technical approaches to trap nanometer sized objects, which are apart from assembly also interesting since they enable biological and chemical studies of particles, cells and molecules under controlled and well defined conditions [143].

Very common are trapping methods, which utilize optical or dielectrophoretic forces to trap particles and molecules. Both methods have demonstrated their utility in a number of experiments, e.g. optical traps have been used to observe the unfolding of single proteins [144] or semi-conducting nanowires have been separated from metallic ones due to their dielectric contrast [145].

Recently, it was demonstrated that geometry induced electrostatic trapping is capable of confining nanoscale gold particles [54, 146] with a diameter down to

10 nm [129] or vesicles of 50 nm diameter [54]. Trapping was achieved by exploiting the repulsive force between the like charged particle and two confining surfaces, where a topographical recess defines a potential well. This modulation was achieved by either etching a topographical recess into a layer of silicon dioxide [54, 146] or by using a nanopipette [129]. The high temporal resolution of iSCAT enabled the measurement of potential profiles and revealed a trapping barrier of several $k_B T$ for 100 nm gold spheres in 100 nm deep pockets within a 200 nm nanofluidic slit at low ionic concentration. Furthermore, a confinement of the orientation of nanorods was observed in elongated traps [147], which lead to the demonstration of a fluid-phase bit switchable by electrical or optical fields [148].

Here, we pattern the recessed trapping structures into the polymer PPA by tSPL with nanometer precision and in 3D, which provides us more flexibility in shaping the trapping potential. Furthermore, we can tune the trapping potential *in-situ* by adjusting the gap distance. We demonstrate that by reducing the gap distance the trapping stiffness increases and that at sufficiently small separations the particles jump into adhesive contact with the polymer surface due to Van der Waals attraction. The combination of a high precision tunable nanofluidic slit with a high sensitive iSCAT detection system, enables us to follow the entire assembly process in unprecedented detail. Furthermore, our implementation of two parallel surfaces enables us to trap and deposit several particles in parallel, which is important for high throughput investigations and assemblies. Finally, the usage of a thermally decomposable polymer, which reproduces the topography of a buried structure and which can be evaporated after the deposition, enables the placement of nanoparticles on different substrates or on existing obstacles.

In Section 7.2.1 60 nm Au spheres are concentrated at an assembly site, using the principle of our rocking ratchet described in the last chapter. The electrostatic trapping is characterized in detail for the spheres in Section 7.2.2 and in Section 7.2.3 we demonstrate precise deposition at targeted locations. The assembly of larger spheres with a diameter of 150 nm is shown in Section 7.3. The aligned placement of gold nanorods is demonstrated in Section 7.4. In Section 7.5 a second silver nanorod is placed vertically aligned on top of a first deposited nanorod. Finally, in Section 7.6 InAs nanowires are aligned by elongated traps and placed across two electrodes in order to connect them.

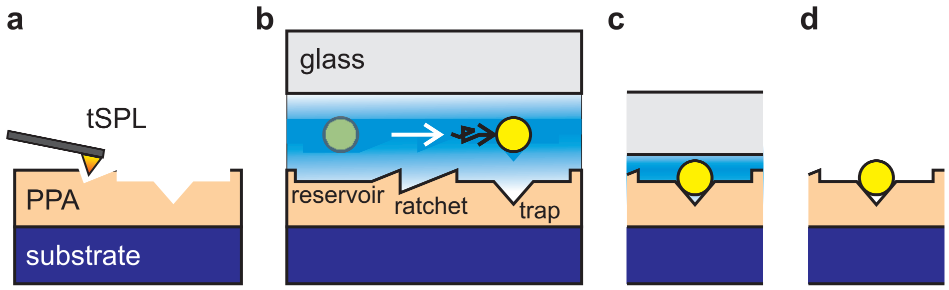

FIGURE 7.1: Process flow of nanoparticle assembly by nanofluidic confinement. (a) A topography is patterned into a PPA film by thermal scanning probe lithography (tSPL). (b) The double layer repulsion allows the trapping of a particle above a hole in the PPA film. Particles are transported by a rocked Brownian ratchet (white arrow) from a reservoir to a assembly site. The final position above a topographical trap are reached by diffusion (black arrow). (c) The top surface is lowered until the particle goes into adhesive contact with the trap. (d) The Van der Waals force keeps the particle at the desired location and the suspension can be removed, without changing the position of the assembled particle.

## 7.2 Parallel assembly of 60 nm gold spheres

In this section we will demonstrate the trapping and assembly of several 60 nm gold spheres into a plasmonic nanostructure. For the fabrication of complex nanostructures, consisting of a large quantity of objects it is important to have a parallel assembly process instead of a serial pick and place method. Krishnan et al. have demonstrated the geometry induced electrostatic trapping of a large number of 80 nm gold spheres in an array of $SiO_2$ recessed cylindrical traps [54]. The traps were spaced on a lattice by 500 nm and had a diameter of 200 nm. In principle the size of the array could be arbitrarily extended as long as enough particles flow past the array of traps and the drag force was smaller than the trapping force.

Here, topographical traps are carved out of a PPA film by tSPL as depicted by the schematic in Figure 7.1 (a). Unfortunately, the implementation of a pressure driven flow is not easy to realize in our open tunable system. However, in Chapter 6 we have demonstrated that we can transport nanoparticles very efficiently with our realization of a rocked Brownian ratchet. Figure 7.1 (b) illustrates the transport of a particle from a reservoir to the assembly site with such a ratchet. Inside the recessed box of the assembly site the particle diffuses until it finds the position of a target trap. The trapping potential of a trap can be tuned with the gap distance such that it can overcome the randomizing Brownian motion.

For immobilization we need to further reduce the gap distance until the Van der Walls forces pull the particle into adhesive contact as shown in Figure 7.1 (c). In our experience this typically requires very short distances between the particle and the confining surfaces, which means that the distance between the bottom of the trap and the cover-glass can not be much larger than the diameter of the particle. However, shallower recessed traps and reservoirs require shorter gap distances until the particles are trapped. This leads to less particles confined under the glass mesa (less volume) and the diffusion of the particles is hindered (see Section 5.3), which eventually reduces the efficiency of collecting particles in the reservoirs. The solution to this problem is to pattern deeper reservoirs, which can trap particles at larger gap distances, and to use ratchets, which can transport the particles to the assembly site.

### 7.2.1 Increasing the concentration at the assembly site

Figure 7.2 (a) shows the written and imaged topography of a PPA film, which we used to arrange 60 nm gold spheres to form the letters IBM. The reservoir areas (inside the blue boxes) were patterned $\approx 75\,\text{nm}$ deep into a polymer film and were capable of trapping particles at a gap distance between the cover-glass and the unpatterned polymer surface of $\approx 160\,\text{nm}$, while the diffusivity of particles outside the patterned region was still $\approx 4\,\mu\text{m}^2/\text{s}$ in one dimension (see Figure 5.3). Nevertheless, the electrical double layer repulsion prevented particles from entering the confined space between the glass-mesa and the polymer surface. While dwelling at this separation for a few minutes, all particles which were confined below the glass mesa either diffused out of the slit or were concentrated in the reservoirs as shown by the five diffusing particles marked by the green circles in Figure 7.3 (a).

The assembly site is inside the red box in Figure 7.2 (a). A magnified and rescaled image of the topography of this region is shown in Figure 7.2 (b). The average depth of the assembly site is recessed by $\approx 23\,\text{nm}$ as indicated by the dashed black line and the red profile in Figure 7.2 (d). Inside this box 35 traps form the letters IBM. The targeted position of these traps is at intersection points of a 200 nm spaced grid and their additional depth is $\geq 10\,\text{nm}$. The sketch in Figure 7.2 (c) illustrates the confinement dependent topographical trapping. The gap distance $d_{\text{IBM}}$ between the cover-glass and the recessed PPA surface in the assembly site is used to characterize the confinement dependent trapping behavior.

In order to deliver the particles from the deeper written reservoirs to the shallower assembly site, the Brownian ratchets inside the green box in Figure 7.2 (a)

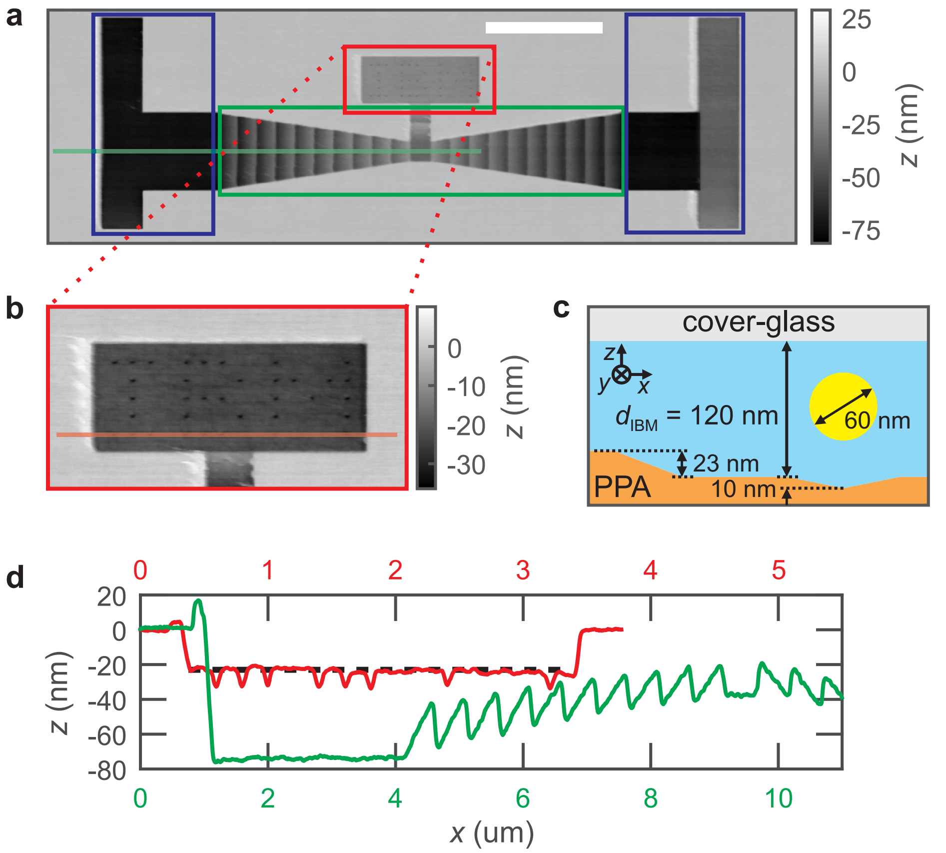

FIGURE 7.2: (a) The topography is imaged and patterned by tSPL. The aim of the recessed areas inside the blue boxes is to trap nanospheres at a larger gap distance. The particles are then transported by the ratchets inside the the green box to the assembly site, which is marked by the red box. (b) The assembly site has a depth of $\approx$ 23 nm with 35 traps. The traps are recessed by another $\approx$ 10 nm and form the letters IBM. The scale bar is 3 $\mu$m. (c) A true to scale sketch of a 60 nm Au sphere, which is trapped in a 10 nm deep conical recess at a glass-PPA separation next to the trap of $d_{\text{IBM}} = 120$ nm. (d) Cross-sectional profile along the green and red lines shown in (a) and (b), respectively.

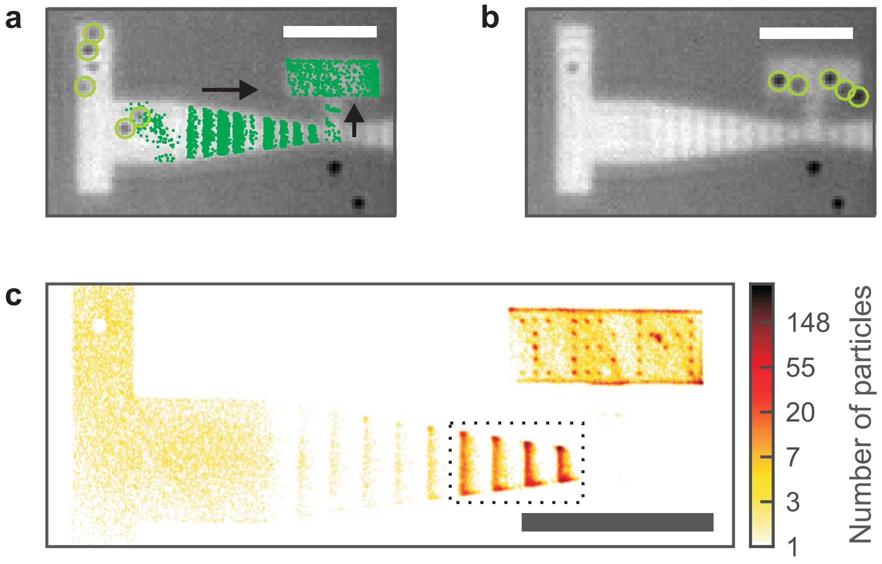

FIGURE 7.3: Transport of 60 nm spheres to the assembly site. (a) Five diffusive particles, marked by green circles, are trapped in the reservoir at a constant gap distance between the cover-glass and the unpatterned PPA surface of $\approx 112$ nm. The unmarked particles are attached to the polymer surface. The green dots indicate detected particle locations of one particle, while applying a 50 Hz square wave potential of $|V| = 6$ V, which leads to directed motion in the direction of the black arrows. (b) The five mobile particles are concentrated at the assembly site. (c) The "heatmap" shows how often a 20 nm grid field is sampled by a particle during transport to the assembly site. (a-c) The scale bar is 3 $\mu$m.

were used. The ratchets allowed gradually moving the particles from the reservoir, where the repulsive interaction was low, to the assembly site, which had a higher repulsive interaction potential. Effective transport was guaranteed by the design of the ratchet amplitude, which became constantly smaller with increasing offset as depicted by the green line in Figure 7.2 (d). In order to actually operate the ratchet i.e., to bring the system out of equilibrium, a 50 Hz square wave potential of $|V| = 6\,\mathrm{V}$ was applied. This led to directed particle transport as indicated by the green dots in Figure 7.3 (a). While the confinement between the cover-glass and the unpatterned PPA surface was kept at a separation of $112.2 \pm 0.5\,\mathrm{nm}$ all mobile particles were transported to the assembly site as shown in Figure 7.3 (b).

The particle distribution for the entire transport is illustrated in Figure 7.3 (c). The so called "heatmap" counts the number of detected particles within a 20 nm grid field. Inside the black dotted box are the parts of the ratchet, which were sampled by the particles the most, which also means that they resided there the longest. The efficiency in a future experiment could be further improved, by either reducing the amplitude of the last ratchet teeth, or by increasing the amplitude of the other teeth and operating the ratchet at a larger gap distance or stronger forcing.

Interestingly, the particle density in proximity of the IBM traps was increased, although they were displaced by the oscillating electrical field. Hence, the particles could also be used as highly sensitive probes to scan a topography. The influence of the topographical potential landscape of the IBM traps will be discussed in detail in the next section.

### 7.2.2 Geometry induced electrostatic trapping

Particle trapping is an interplay between the surface topography and the electrostatic interaction between the particles and the surfaces. As an example Figure 7.4 (a) shows the particle density at a gap distance of $d_{\mathrm{IBM}} \approx 120.2\,\mathrm{nm}$ with no applied electrical field. It can be clearly seen that the particle density was highest at the IBM traps. Furthermore, in contrast to the case with an applied field (see Figure 7.3 (c)), the increased probability of detecting a particle close to the rim of the assembly box has vanished.

We used radial symmetry-based tracking to identify the center of the particles [116]. The tracking algorithm determines the minimum of parallel lines to a gradient at any point. For a radially symmetric intensity distribution, the mean distance-squared between gradient lines and determined center is 0. In a noisy, pixelated image, these intersections will not be exact, but

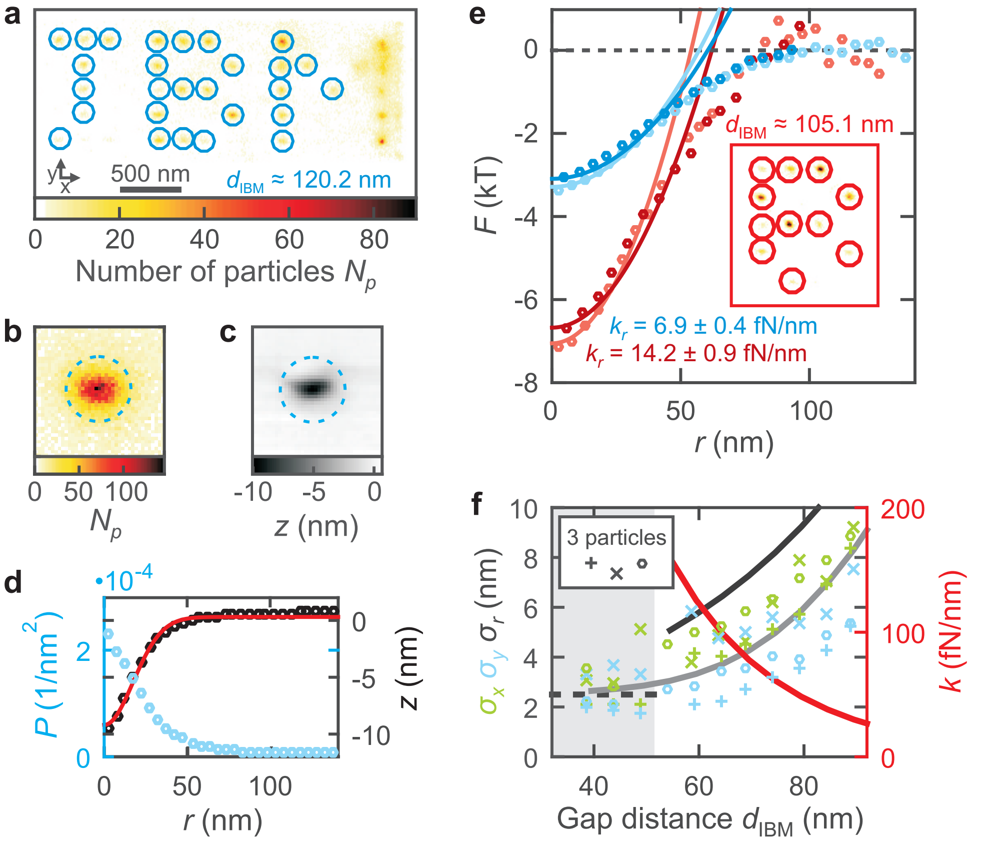

FIGURE 7.4: Geometry induced electrostatic trapping. (a) Number of detected particles $N_p$ in a 10 nm grid field within ≈ 13,000 frames at a constant gap distance. (b) The average particle distribution in a 5 nm grid determined by the sum of the distributions marked by the blue circles in (a). (b,c) The diameter of the dashed blue line is 100 nm. (c) Average topography of the trap defining the letters IBM in Figure 7.2 (b). (d) The averaged empirical probability histogram of detecting a particle in a trap as a function of radial distance to the center is indicated by the light blue circles. The dependency of the average topography to the trap center is depicted by the black circles. The width of the Gaussian fit is $\sigma_z \approx 17$ nm (red line). (e) Radial free energies $F(r)$ averaged over the particle and trap ensemble at a gap distance of $d_{\text{IBM}} \approx 120.2$ nm (blue) and $d_{\text{IBM}} \approx 105.1$ nm (red). The brighter circles are determined via the Boltzmann relation $F(r) = -k_B T \ln P(r)$ using the measured empirical probability distributions. The darker circles are corrected for detection noise and motion blur. The inset shows the particle distribution as in (a), but at a gap distance of $d_{\text{IBM}} \approx 105.1$ nm. (f) The green and blue symbols depict the standard deviations of measured particle positions in $x$- any $y$-direction, respectively. The gray line is an expected standard deviation of radial displacement, based on the measured values in (e), and the black line is corrected for motion blur and detection noise. In the gray region the particles are already immobilized. The dashed black line indicates an averaged lateral localization accuracy of $\sigma_{r,\,\text{noise}} \approx 2.5$ nm. The expected trap stiffness is depicted by the red line and decays by $k_r \approx 1.96\ \exp(-0.048\, d_{\text{IBM}})$ pN/nm.

nevertheless a center can be determined which minimizes this value. In case the overlap of the contrast profiles is too large ($\lesssim$ 200 nm) the distribution has typically a more elliptical shape and a center between both particles is detected. For such a contrast distribution, the minimal value for the mean distance-squared is also increased. Only particle positions with an average accuracy below 0.1 pixels were accepted. This provided a reasonable compromise between culling the averaged location of multiple particles and keeping most of the single particle locations.

Figure 7.4 (a) shows the particle distribution within 13 s at a gap distance $d_{\mathrm{IBM}} \approx 120.2\,\mathrm{nm}$. We like to point out that during the entire time on average 3 out of 5 particles were located close to the traps at the right hand side of the letter M, which was most likely caused by the slightly more recessed topography at the right hand side of the assembly site (see red profile in Figure 7.2 (d)). This led to an increased probability of detecting the average position of multiple particles, as a consequence the particle distributions around the traps at the right hand side of the letter M seem to be more smeared out compared to the other distributions. Therefore, for the further analysis only detected particle locations to the left hand side and above a certain threshold are considered as depicted by the blue circles in Figure 7.4 (a). The centers of these distributions are determined by radial symmetry-based tracking [116]. The particle positions within $\pm 100\,\mathrm{nm}$ in x- and y-direction to the center of each particle distribution are used to create an accumulated particle distribution of the ensemble of detected particles and sampled traps. Figure 7.4 (b) shows the resulting histogram with a grid size of 5 nm.

Similarly, an average trap topography is calculated by means of overlaying and interpolating the individual trap geometries using cross-correlation. The result is depicted in Figure 7.4 (c). The average trap is slightly wider in the x-dimension than in the y-dimension, which is probably caused by an asymmetric writing process. The same asymmetry can also be observed in the particle distribution in Figure 7.4 (b). Nevertheless, the asymmetry is small and therefore we use the particle distribution to calculate an empirical probability histogram of detecting a particle as a function of radial distance to the center of the distribution as shown by the light blue circles in Figure 7.4 (d). The particle distributions are averaged azimuthally and normalized such that $\int 2\pi r P(r)\,\mathrm{d}r = 1$. The black circles depict the averaged radial topography profile. The width of a Gaussian fit (red line) to the data is $\sigma_z = (17.3 \pm 0.5)\,\mathrm{nm}$.

The radial distance dependent trapping energy can be derived from the probability density $P(r)$ according to the Boltzmann relation by $F(r)/k_B T = -\ln(P(r))$, where $k_B$ is the Boltzmann constant and $T$ is the absolute temperature. The free energy $F$ is shown in Figure 7.4 (e) by the light blue circles for a confinement of $d_{\mathrm{IBM}} \approx 120.2\,\mathrm{nm}$ and by the light red circles for a gap distance of $d_{\mathrm{IBM}} \approx 105.1\,\mathrm{nm}$. The inset in Figure 7.4 (e) shows the particle distribution for the letter B at a gap distance of $d_{\mathrm{IBM}} \approx 105.1\,\mathrm{nm}$.

Close to a potential minimum the harmonic oscillator provides a good approximation for any potential energy function. Therefore, we fit the potential energy of a linear spring $U(r) = \frac{1}{2}k_r r^2$ to the measured free energy values, which have a radial distance of less than $r < 40\,\mathrm{nm}$. The trapping stiffnesses of the fits are $k_r = (8.3 \pm 0.5)\,\mathrm{fN/nm}$ and $k_r = (19.9 \pm 1.3)\,\mathrm{fN/nm}$ as depicted by the light blue and light red line, respectively.

However, the measurements of the trapping energy and stiffness are affected by the motion blur of the particles, due to the finite particle illumination time [149]. In the following paragraph we will present a method how this effect can be taken into account:
The variance of positions $\sigma_r^2$, of a particle undergoing Brownian motion in such a parabolic potential, can be determined due to the equipartition theorem as [149]

$$\sigma_r^2 = \frac{k_B T}{k_r}. \tag{7.1}$$

For a direct measurement of the instantaneous particle positions the illumination time of the particles $\tau_{\mathrm{illu}}$ has to be much smaller than their relaxation time

$$\tau_{\mathrm{rel}} = \gamma / k_r, \tag{7.2}$$

where $\gamma = 3\pi\eta a$ is the drag coefficient for a sphere of diameter $a$ in a solution of viscosity $\eta = 1\,\mathrm{mPa\,s}$. For larger illumination times an averaged blurred position is detected, which leads to a narrower particle distribution and thus smaller measured variance $\sigma_{r,\,\mathrm{meas}}^2 \leq \sigma_r^2$. The experimentally detected particles are illuminated by raster scanning a field of $\approx 40 \times 40\,\mu\mathrm{m}^2$ once with a $2\,\mu\mathrm{m}$ wide Gaussian beam within an exposure time of $\tau_{exp} = 1\,\mathrm{ms}$ and a line duration of $10\,\mu\mathrm{s}$. This corresponds to a laser line spacing of 400 nm and a particle illumination time of $\tau_{\mathrm{illu}} \lesssim 50\,\mu\mathrm{s}$ as explained in detail in Section 3.1.2. A motion blur and detection noise corrected measurement of the particle variance $\sigma_r^2$ can be obtained by [149]

$$\sigma_r^2 = \left(\sigma_{r,\,\mathrm{meas}}^2 - \sigma_{r,\,\mathrm{noise}}^2\right) / \left(\frac{2}{\tau_{\mathrm{illu}}/\tau_{\mathrm{rel}}} - \frac{2}{\left(\tau_{\mathrm{illu}}/\tau_{\mathrm{rel}}\right)^2}\left(1 - e^{-\tau_{\mathrm{illu}}/\tau_{\mathrm{rel}}}\right)\right), \tag{7.3}$$

where $\sigma_{r,\,\mathrm{meas}}^2$ and $\sigma_{r,\,\mathrm{noise}}^2$ are the variance of particle positions without correction and caused by detection noise,respectively.

| $d_{\mathrm{IBM}}$ | 120.2 nm | 105.1 nm |
|---|---|---|
| $F(0)$ | $(-3.1 \pm 0.2)\,k_BT$ | $(-6.7 \pm 0.4)\,k_BT$ |
| $\Delta W_{edl}$ | $-6.5\,k_BT$ | $-12\,k_BT$ |
| $\sigma_r$ | $(24.3 \pm 1.4)$ nm | $(17.0 \pm 1.1)$ nm |
| $k_r$ | $(6.9 \pm 0.4)$ fN/nm | $(14.2 \pm 0.9)$ fN/nm |
| $\tau_{\mathrm{rel}}$ | $(81 \pm 5)\,\mu$s | $(40 \pm 3)\,\mu$s |

TABLE 7.1: The "blur- and noise-free" values for the trapping energy $F(0)$, the standard deviation of particle positions $\sigma_r$, the trapping stiffness $k_r$ and the relaxation time $\tau_{\mathrm{rel}}$. The electrostatic interaction energy for a sphere with a surface potential $\psi_{S,0} = -58$ mV confined by two parallel plates with surface potential $\psi_{P,0} = -67$ mV can be calculated by Equation 2.15. $\Delta W_{edl}$ is difference in energy between two such systems, where system 1 has a gap distance of $d_{\mathrm{IBM}}$ and system 2 has $d_{\mathrm{IBM}} + 5$ nm.

With the Equations (7.1) – (7.3) we can make a first estimation of the motion blurred relaxation time and thus calculate an updated variance of particle positions. Then we can re-calculate the trapping stiffness and the relaxation time. We iteratively optimize the variance of particle positions $\sigma_r^2$, the radial trapping stiffness $k_r$ and the relaxation time $\tau_{\mathrm{rel}}$. After a few iterations the values saturate to the motion blur and detection noise corrected values. For the noise correction a standard deviation of $\sigma_{r,\,\mathrm{noise}} \approx 2.5$ nm was used. This value is measured for immobilized particles as depicted by the black dashed line in Figure 7.4 (f)). We like to point out that this value is still in agreement with the estimated optimal detection precision of $\leq 1.5$ nm determined in Section 4.5, since here, the interference condition was not optimized to give the best contrast while the particles are immobilized.

The motion blur and detection noise corrected free energies are shown by the darker colors in Figure 7.4 (e)). In order to clarify the energy a particles gains when it is trapped, we have shifted all energies such that the average energy outside of the area of influence ($r > 90$ nm) is zero. The "blur- and noise-free" values for the trapping energy $F(0)$, the standard deviation of particle positions $\sigma_r$, the trapping stiffness $k_r$ and the relaxation time $\tau_{\mathrm{rel}}$ are shown for both gap distances in Table 7.1. Already the reduction of the particle-wall-distance by a quarter has lead to a doubling of potential energy. The repulsive forces on the particle in the trap originate from the electrostatic double layer potentials, which are described in detail in Section 2.1.2. The Equations (2.12) – (2.16) describe the interaction energy of a particle confined by two planes. In order to estimate the trapping energy we make a rough simplification and assume that the interaction energy for the particle in the trap is similar to a case where a flat polymer surface is recessed by half the deepest trap depth (5 nm). Furthermore, we use the same surface potential for the polymer surface as for the silicon oxide surface $\psi_{P,0} =$

$-67\,\mathrm{mV}$ [60], we set the surface potential of the particle $\psi_{S,0}$ to the measured zeta potential $\psi_\zeta = -58\,\mathrm{mV}$ (see Table 3.1) and we use the Debye length $\kappa = 12.5\,\mathrm{nm}$, which was determined by conductivity measurements (see Table 3.2). The resulting differences in interaction energy $\Delta W_{edl}$ are also shown in Table 7.1. The calculated values are approximately twice as large as the measured value, which is reasonable for the rough estimation we have done.

The need for motion blur correction becomes obvious when comparing the corrected and uncorrected trapping stiffnesses at a gap distance of $d_{\mathrm{IBM}} \approx 105\,\mathrm{nm}$. The corrected trapping stiffness is reduced by more then 25 %, although the relaxation time $\tau_{\mathrm{rel}} \approx 40\,\mu\mathrm{s}$ and the illumination time $\tau_{\mathrm{illu}} \lesssim 50\,\mu\mathrm{s}$ are almost equal.

An exponential decay of the trapping stiffness $k_r$ with the confinement $d$ was already observed by Tae Kim et al. [129]. They measured the trapping behavior of 60 nm gold spheres in a nanopipette and observed a good agreement with a simulated decay of $k_r \propto \exp(-0.04d)$. Motivated by this observation we also assumed an exponential decay, i.e. $k_r = A\exp(-B\,d_{IBM})$. The parameters $A \approx 1.96\,\mathrm{pN/nm}$ and $B \approx 0.048\,1/\mathrm{nm}$ are calculated by using the corrected trapping stiffnesses at a gap distance of $d \approx 105.1\,\mathrm{nm}$ and $d \approx 120.2\,\mathrm{nm}$ (see Figure 7.4 (e)). Similar to the ratchet experiment the decay length $l = 20.8\,\mathrm{nm}$ is characterized by the Debye length (see Section 6.2.1 and Table 3.2). The decay of trapping stiffness is depicted by the red line in Figure 7.4 (f). This relationship together with Equations (7.1) – (7.3) also allows us to calculate the expected standard deviation of particle positions with and without blur correction for various gap distances shown by the black and gray line, respectively. Clearly, the measured standard deviations of particle positions in the x- and y-direction as represented by the green and blue symbols are in good agreement with the expected values. Only three particles are considered, since their nearest neighbor distance during the assembly process was more than 500 nm. This avoids an influence on the particle localization caused by an overlap of the point spread functions. Nevertheless, the exponential dependency between trapping stiffness and confinement for our particle trap system is validated.

The three particles in Figure 7.4 (f) show a systematically increased standard deviation in the x-direction compared to the y-direction. This is likely due to the asymmetry in the topography we already observed for an average trap (see Figure 7.4 (c)). Furthermore, in Figure 7.4 (f) no standard deviations of particle positions are shown, which would contain a mix of mobile and immobilized particle positions. The white and light gray regions show the standard deviation for mobile and immobilized particles, respectively. In the next section we see that the particle intensity can be used to determine the exact point of immobilization, which slightly varies from particle to particle.

| | | 1 | 2 | 3 | 4 |
|---|---|---|---|---|---|
| $\phi_0$ | $(\pi)$ | 0.86 | 0.87 | 0.84 | 0.86 |
| $\gamma$ | (a.u.) | 0.13 | 0.12 | 0.11 | 0.12 |
| $p$ | (a.u.) | 0.74 | 0.95 | 0.82 | 0.66 |

TABLE 7.2: Optical fit parameters of the four particles in Figure 7.5 (b), where $\gamma$ is the fraction of the incoming light interacting with the particle, $p$ is the scattering amplitude of particle and $\phi_0$ defines the effective scattering phase.

### 7.2.3 Assembly of 60 nm gold spheres

In Section 4.7 the particle height of 60 nm Au spheres confined between PPA and the cover-glass surfaces was measured and we observed an average particle height above the middle of the gap. In those experiments a 52 nm thick film of HM and 175 nm of PPA were spin coated on a silicon wafer to provide a good sensitivity of the particle height for gap distances of 115 nm $\leq d \leq$ 175 nm, but less sensitivity and multiple height solutions for gap distances below 100 nm. For the experiments described in this section, the thickness of the PPA layer at the assembly site was adjusted to 149 nm, such that the particles provided a good contrast during the trapping and to allow a distinct attribution of particle heights during the assembly ($\lesssim d_{IBM} \lesssim$ 70 nm). The measured and normalized contrast values of a single diffusing particle for varying gap distances $d_{\mathrm{IBM}}$ are shown by the black scatter plot in Figure 7.5 (a), where the black arrows indicate the direction of displacement of the cover-glass during the measurement. Starting at a confinement of $d_{\mathrm{IBM}} \approx 90$ nm the particle sampled, with varying height, the contrast values between $-0.5 \lesssim I'_{ctr} \lesssim -0.45$. The first schematic on the right hand side of Figure 7.5 (a) is scaled to illustrate this situation. The more the gap distance is reduced, the narrower the width of the contrast distributions gets, until it abruptly jumps to a higher and almost constant value for several gap distances. After reaching this point, the contrast fluctuations have a similar width as measured for immobilized particles (see Figure 4.6 (b)). At a gap distance of $d_{\mathrm{IBM}} \approx 35$ nm the motion of the cover-glass is reversed and for $d > 40$ nm a hysteresis in the measured contrast is observed. The contrast modulation during the retraction of the cover-glass (yellow region) is similar to the one measured for particles immobilized on a oxide covered silicon sample (see magenta dots in the lower panel of Figure 4.6 (b)). The contrast change in the blue region in Figure 7.5 (a) deviates from this modulation and we interpret this reversible process as follows: The particle is first pressed into the PPA by the cover-glass and then the elastically compressed polymer lifts it up again, when the cover-glass is retracted.

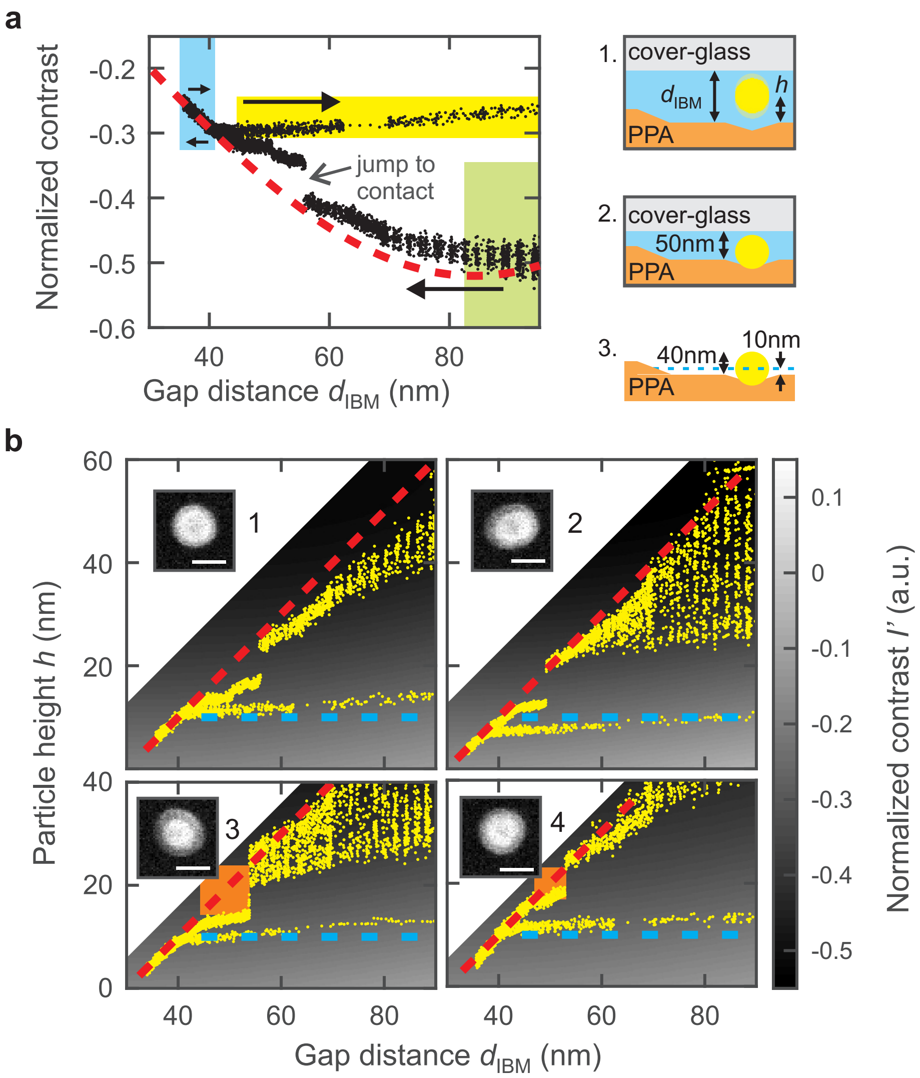

FIGURE 7.5: Particle deposition. (a) Normalized contrast (black scatter plot) of a single trapped particle for varying gap distances. The black arrows indicate if the cover-glass approaches the PPA layer or if it is retracted. The simulated contrast envelope (dashed red line) is defined by the measured minimal and maximal contrast in the green and blue region, respectively. At a gap distance of $d_{\mathrm{IBM}} \approx 53\,\mathrm{nm}$ the contrast makes a jump and then stays almost constant, while the cover-glass position is lowered. The contrast signal has a hysteresis after the particle was in contact with both surfaces (blue region) and the contrast is only slightly modulated while retracting the cover-glass (yellow region). The right insets illustrate the measured particle height $h$ for several gap distances $d_{\mathrm{IBM}}$. (b) Attributed particle heights (yellow dots) are obtained by matching the measured contrast and simulated contrast values (gray-scale background image). The four panels show the attributed heights for four different particles. The insets show SEM images of the particles with 60 nm scale bars. The orange regions show the maximum distance the particles can jump from a position close to the cover-glass into the PPA trap.

Usually we determine the parameters $\gamma$, $p$ and $\phi_0$, which characterize the relationship of particle height and contrast, by fitting envelopes to the measured maximum and minimum particle contrast values. However, at a confinement where one could measure the maximum contrast, particles are not trapped anymore by the recessed geometry of the assembly site. Therefore, the contrast values in the blue and green region in Figure 7.5 (a) are used and the parameters are iteratively optimized until the contrast envelope (dashed red line) best defines the envelope of minimal and maximal contrast in the green and blue region, respectively. The particle heights in the blue region are fixed to be in contact with the cover-glass. The determined fit parameters for four particles are shown in Table 7.2. These parameters are used to model the contrast as shown by the gray-scale background images in Figure 7.5 (b) for various gap distances $d_{\mathrm{IBM}}$. The height values of the yellow dots are obtained by looking for the best agreement between measured and simulated contrast value at a particular gap distance. For the gap distances $d_{\mathrm{IBM}} \lesssim 80\,\mathrm{nm}$ only single valued height solutions are considered; other solutions are rejected due to the physical boundaries of the cover-glass and the PPA surface.

As already described in Section 4.7, we suspect that the rotation of asymmetrically shaped particles leads to a fluctuation of particle contrast and thus an increased scatter of attributed height values. The insets in Figure 7.5 (b) show SEM images of the deposited particles. Note that the polymer layers have affected the image quality (see high resolution images taken on a conductive silicon sample in Figure 3.8). The SEM image of the particle 2 shows that the particle is elongated. This could explain the much narrower scatter of particle heights, while the particle was suspended, at gap distances around $d_{\mathrm{IBM}} \lesssim 60\,\mathrm{nm}$ and the larger spread at higher gap distances. In Figure 7.4 (c) we have shown that the topography of an average trap was slightly wider in the x-direction, which is in agreement with the orientation of the elongated particle. The asymmetry of the trap prevented the particle from rotating in the xy-plane at smaller gap distances. At $d_{\mathrm{IBM}} \gtrsim 70\,\mathrm{nm}$ the particle started to rotate, which changed the scattering cross-section depending on the alignment with respect to the polarization of the illuminating light; thus the width of the distribution of attributed height values is increased. Particle 1 seems to be more spherical than the particles 3 and 4, which could explain the obtained height values above the dashed red lines in Figure 7.5 (b) and the much broader scatter of heights for particle 3.

For particle 3 the shift of contrast translates into a jump distance to contact between 5 and 9 nm, if particle heights above the determined cover-glass position are omitted. While the cover-glass was further approached, the contrast and thus the assigned particle height stayed constant for $\approx 9\,\mathrm{nm}$ (see width of orange regions in Figure 7.5 (b3)). The difference in gap distance, is also an indicator that the particle heights above the dashed red line have to be omitted; the distance is an upper limit for the difference in particle height e.g. jumping from a position close to the cover-glass to the bottom of the trap. The second schematic on the right hand side of Figure 7.5 (a) illustrates this situation.

The overlap of the point spread functions of a particle in close proximity also affected the measured contrast. Therefore, only 6 particles with a nearest neighbor distance of $\gtrsim 400\,\mathrm{nm}$ during the deposition are considered. All particles show a jump into contact between 5 and $9\,\mathrm{nm}$ at an average gap distance of $d_{\mathrm{IBM}} \approx 53 \pm 3\,\mathrm{nm}$. Even if we add the total trap depth of 10 nm the particle were not capable of traveling such a long distance at such an confinement. However, the four particles in Figure 7.5 (b) rested at an average height of $\approx 15\,\mathrm{nm}$ after the jump, which indicates that the traps were rather $\gtrsim 15\,\mathrm{nm}$ deep.

The Hamaker constants of PPA and of the glass (see Table 2.1) are almost equal. However, the thermally excited particle only jumps from the glass to the polymer surface, which is most likely caused by stronger adhesion due to an increased contact region with the polymer surface. Another effect which would support a particle jump from close to the glass surface towards the polymer surface would be a strong charge regulation of the polymer surface.

After deposition, the particles stay immobilized even while retracting the cover-glass. At a sufficiently large gap distance other particles diffuse into the field of view and the transport, trapping and assembly process can be repeated. With each approach we assemble approximately 5–8 particles. This number is only limited by the amount of particles delivered to the assembly site and could be easily increased by a higher particle density, a larger surface area underneath the glass mesa or an increased size of the reservoirs.

The third schematic in Figure 7.5 (b) illustrates that a particle with a final height of $h = 10\,\mathrm{nm}$ (dashed blue line) sticks out $40\,\mathrm{nm}$ from to the floor of the assembly site. This is in good agreement with the AFM image and the cross-sectional profile of the letter M in Figure 7.6 (a). In order to quantify the positioning accuracy, an SEM image of all the assembled particles was taken, see Figure 7.6 (b). The centers of the deposited nanospheres in this image are determined by radial-symmetry-based tracking [116] and the 34 red plus signs indicate the central position of nano-objects placed at a correct location. The black plus sign shows the position of one particle which was deposited at a wrong location. One trap in the letter I is vacant and one dumbell particle has been assembled in the letter M. The positions of correctly assembled objects are also shown by the red plus signs in Figure 7.6 (c). The targeted position of the traps were located on a 200 nm

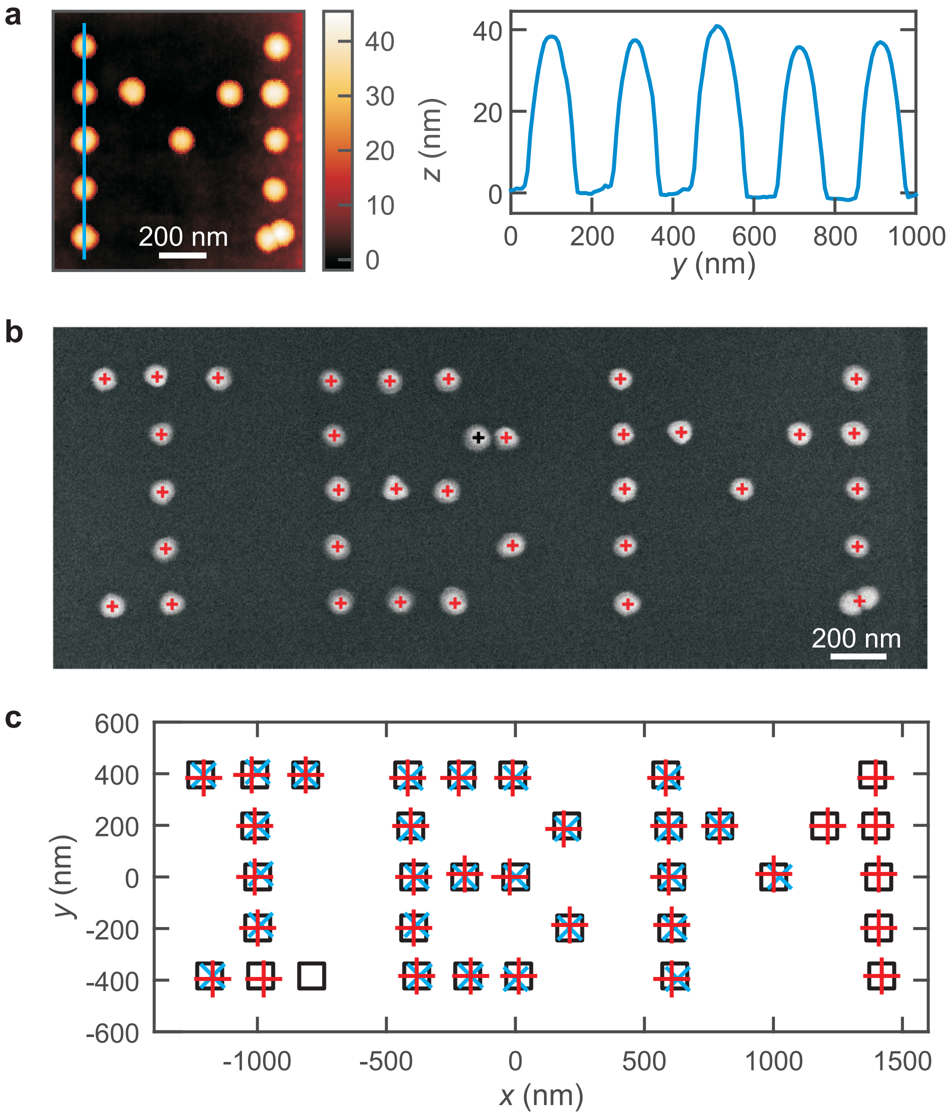

FIGURE 7.6: Assembled 60 nm Au spheres. (a) Topographical AFM scan of particles assembled to form the letter M. The cross-sectional profile along the blue line indicates that particles sticked out 40 nm from the bottom surface of the assembly site. (b) SEM image of all assembled particles form the letters IBM. Position of correctly assembled particles are shown by red plus signs. A black plus sign indicates the position of a particle at a wrong location. (c) The red plus signs have the same meaning as in (b). The black squares represent the estimated trap positions; a scaled and skewed 200 nm grid was used to compensate the thermal drift of the scanning systems for imaging and patterning. The centers of measured particle distributions at a gap distance of $d_{IBM} \approx 120.2$ nm (see Figure 7.4 (a)) are depicted by the blue crosses.

grid. Please note that the patterning and the imaging of the assembled particles are done with scanning systems, which are prone to thermal drift. To compensate this effect, we preformed a least-square fit of a skewed and y-scaled 200 nm squared grid to the data of detected particle positions. The obtained trap positions are shown by the black squares in Figure 7.6 (c). With the same method we also determined the best fitting parameters for detected particle distributions from Figure 7.4 (a). The resulting positions are depicted by the blue x-signs in Figure 7.6 (c).

As a measure of positioning accuracy, we determined the distances $r$ between the centers of the nanospheres and the traps. The standard deviation of the radial displacement is $\sigma_r = 8.3$ nm. Before jumping into contact, the standard deviation of the radial particle positions was $\sigma_r \approx 5$ nm as determined from the black line in Figure 7.4 (f). The additional $\approx 3$ nm displacement were probably caused by writing inaccuracies or while the cover-glass was in contact with the particles. For the assembled particles, the standard deviation of the position in the x-direction $\sigma_x = 6.6$ nm is slightly larger compared to the y-direction $\sigma_y = 5.2$ nm, which is in agreement with the aforementioned asymmetry of the trap topography.

## 7.3 Assembly of 150 nm gold spheres

In the last section we investigated the assembly of 60 nm gold spheres in PPA traps with a similar diameter. Here, we will show the assembly of citrate stabilized 150 nm Au spheres (BBI Solutions) into traps with a 3 and 5.5 times larger diameter. Figure 7.7 (a) shows an AFM image of an assembled 150 nm Au sphere in a PPA recess with a diameter of 500 nm. Figure 7.7 (b) shows that the topographical trap is located in an array of traps, which are recessed by $\approx 58$ nm. The red dots depict the detected particle positions and for the medium and large trap we observed particle trapping at gap distances below $d \lesssim 230$ nm. We used the same scaling and orientation to overlay the particle positions with the AFM images in Figure 7.7 (a) and (b). The color indicates the gap distance between the unpatterned PPA surface and the cover-glass at that particular moment. At gap distances $d \lesssim 150$ nm, we only detect particle positions which are close to the rim of the trap. At first glance this seems to be counterintuitive to what one would expect for negatively charged particles and confining surfaces. However, such a behavior has been already observed by others for 100 nm gold spheres [54], 20 nm polysytrene spheres [150] and DNA [151]. Simulations of the electrostatic potential of the structure alone cannot explain this effect [150].

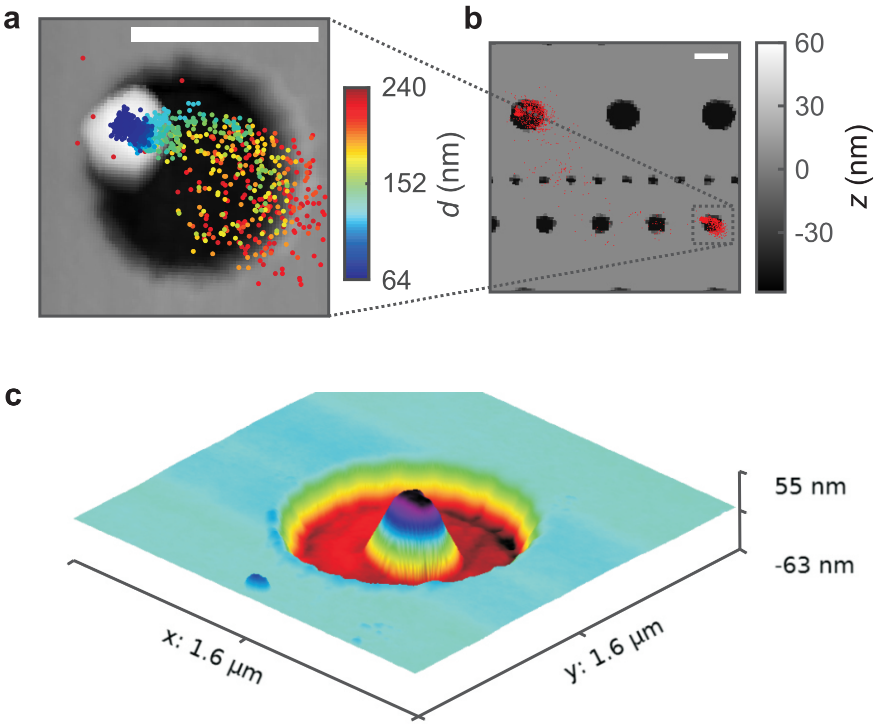

FIGURE 7.7: (a) AFM topography image of a deposited gold particle with a diameter of $2a = 150$ nm. Both the diameter of the medium sized cylindrical recess and the width of the white scale bars are 500 nm. The optically measured particle positions are depicted by the colored dots; the color indicates the gap distance $d$ during the assembly of the nanosphere. (b) The particle was first trapped in a large cylindrical recess, then released at a larger gap distance and again trapped and assembled in the recess shown in (a). The red dots show the detected particle positions. (c) 3D AFM image of a 150 nm Au sphere placed close to the center of a 815 nm trap.

A change in particle contrast indicates that the particles were deposited at a gap distance of $d \approx 105\,\text{nm}$, which corresponds to a $d_{\text{trap}} \approx 165\,\text{nm}$ separation between the cover-glass and the bottom of the trap. Figure 7.7 (c) shows a 3D AFM image of one particle which has been assembled close to the center of the trap. The difference in placement precision between the assembled 150 nm and 60 nm gold spheres suggests that, for precise positioning of particles with a relative radius between $2 \lesssim \kappa a \lesssim 10$, the trap should have a similar size as particle.

## 7.4 Assembly of gold nanorods

The assembly of nanostructures as decribed in the previous sections is not restricted to spherical particles, but can also be applied to particles with a more complex shape e.g. nanorods.

Today, colloidal gold nanorods of high quality are commercially available. They are most often synthesized by a seed mediated growth method, since this leads to high quality, mono-disperse and well characterized nanorods [5]. Typically, citrate stabilized gold nanospheres, with a diameter of 3–4 nm, are added to a $HAuCl_2$ growth solution. The growth solution is obtained by the reduction of $HAuCl_4$ with ascorbic acid in the presence of cetyltrimethylammonium bromide (CTAB) surfactant and silver ions [152]. Due to a catalytic effect of gold the ascorbic acid reduces gold ions to gold atoms only at the surface of the seed particles. Parameters, such as the concentrations of ascorbic acid, seed particles and surfactant, as well as the temperature and pH determine the yield, size, shape, and monodispersity of the resulting gold nanorods. The directional growth is most likely initiated by the development of facets on the surface of the seed particles [153, 154]. A preferential binding of the CTAB to one facet leads to a blockage of this facet. The growth of the other facets results in the rod like shape. The CTAB forms a bilayer structure on the longitudinal surface of gold nanorods and stabilizes the colloid by its positive charge. Alternatively, stabilization can be achieved by a negative surface charge or a conjugation of biomolecules. This can be achieved by exchanging CTAB with thiols, the use of biofunctional linkers, surface coatings or through electrostatic absorption [5].

Due to the elongated shape, gold nanorods have a second red shifted surface plasmon resonance corresponding to electron oscillations along the long axis. The wavelength can be in the near-IR region, which is not absorbed by biological tissue and thus makes them particularly interesting for photo-thermal cancer therapy [155–157].

The trapping method presented in the last section is also not restricted to negatively charged particles and could in principle be adopted for positively charged particles and confining walls. In order to test this assumption, we used commercially available CTAB stabilized nanorods and microgold with a zeta potential of $\zeta \approx +38\,\text{mV}$ measured by the manufacturer Nanopartz. Similar to the citrate stabilized particles, we observed that the particles are generally stable and do not adhere to neither the glass surface nor the polymer surface. The stability of the positively charged nanorods is most likely due to the free CTAB in the solution which also forms a bilayer on the confining surfaces. In our experiments we could not observe any trapping of CTAB stabilized $75 \times 500\,\text{nm}$ gold microrods. It even seemed that the particles avoided the topographical traps. The grooves were patterned with a depths of $\approx 50\,\text{nm}$ and with the same aspect ratios as the rods but between 1.5 and 8 times larger lateral dimensions. The manufacturer claims that the CTAB bilayer has a thickness of $\approx 6\,\text{nm}$, which also can not explain the observed effect. However, a high CTAB concentration, which is necessary for the stability of the colloid, leads to the formation of micelles [5]. A strong affinity of the CTAB to the PPA could lead to the formation of micelles or multi layers in the recessed geometries, which would explain the repulsion of the particles from the traps.

For our next experiment we used nanorods, which were stabilized by the negative charge of 11-Mercapto-undecanoic acid (MUA). According to the manufacturer (Nanopartz), the density of the colloid was $6.2 \cdot 10^{12}$ particles per milliliter, with a zeta potential of $\zeta = -16\,\text{mV}$. The conjugated gold nanorods had a diameter of 25 nm and a length of 94 nm, i.e. an aspect ratio of 3.8, which led to a longitudinal plasmon resonance centered at 780 nm. To track the particles, we therefore used a continuous wave laser at 785 nm (StingRay-785 90 mW, Coherent) and a AOD (DTSXY, AA Opto-Electronic) suitable for this wavelength. For linear polarized light, the orientation of the nanorod with respect to the polarization axis strongly affected the amount of scattered light, while the shape of the scattering pattern is diffraction limited and therefore circular. The circular shape of the particle contrast allowed us to determined the center of the particles with radial-symmetry based tracking [116].

Figure 7.8 (a) shows the topography of a selected region patterned by tSPL into PPA. The purpose of the grove was to trap and align the nanorods. The red line shows the measured trajectory of a single particle while reducing the separation between the cover-glass and the polymer surface. The blue arrows indicate the approximate gap distance $d$, when the particle was detected at that particular location. At a confinement of $d \approx 360\,\text{nm}$ and $d \approx 340\,\text{nm}$, the particle was directly

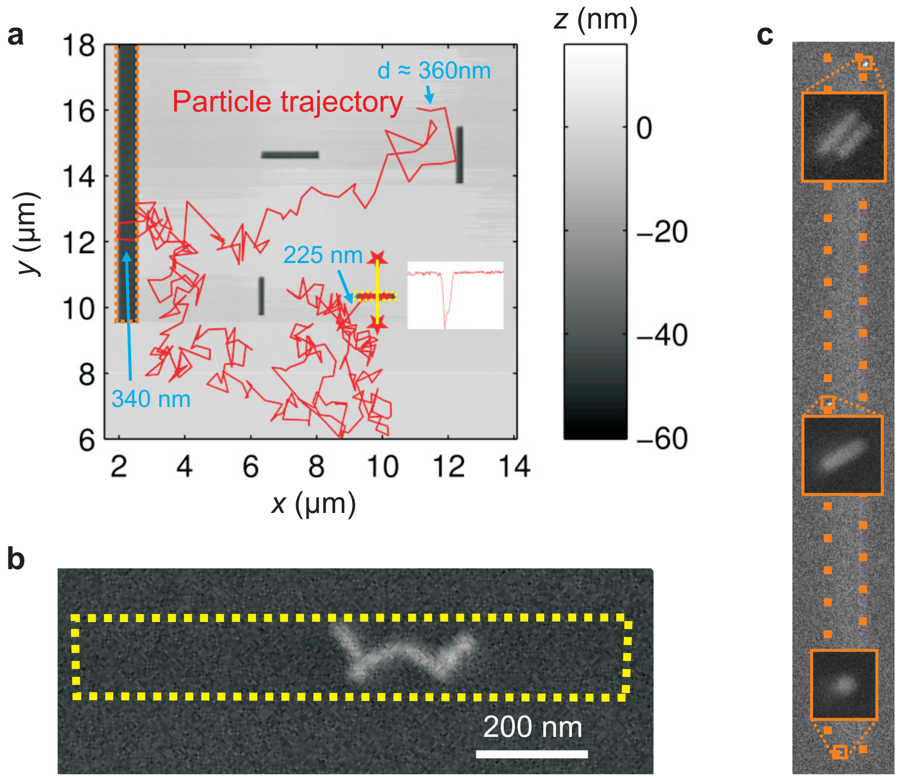

FIGURE 7.8: Assembly of gold nanorods conjugated by 11-Mercapto-undecanoic acid. (a) tSPL topography image of elongated traps to trap and deposit gold nanorods. The overlayed red line depicts an optically detected particle trajectory, while the gap distance $d$ between the cover-glass and unpatterned PPA surface was reduced. The blue numbers indicate the approximate gap distances at a particular position of the particle. The inset shows the cross-sectional profile of the trap, in which the particle was trapped and assembled. (b) The SEM image shows that the assembled particle was an agglomerate of four $25\,\mathrm{nm} \times 94$ nm Au nanorods. However, the elongated shape of the agglomerate matches the elongated trap, illustrated by the dotted yellow line. (c) Two single particles and a double particle were assembled at the rim of the recessed area as highlighted by the doted orange line.

above a recessed structure, but the trapping potential had only a negligible effect on the motion of the particle. At a gap distance of $d \approx 225\,\text{nm}$, the trapping potential was sufficiently high and the particle got trapped. At an even shorter gap distance, the motion and contrast fluctuations of the particle stopped, which indicated that the particle was assembled and that the cover-glass could be recessed. The SEM image in Figure 7.8 (b) shows that the deposited particle was not a single nanorod, but rather an agglomerate of four nanorods. But the particles were arranged in the form of a stretched "w" and the orientation of the agglomerate matched the shape of the topography, which is indicated by the dotted yellow line.

The recessed stripe in Figure 7.8 (a) (see orange dotted line) was patterned to allow the feedback of the tSPL tool to optimize the writing parameters, such that the traps are patterned with a constant depth. However, it was also used to trap and assemble particles. As with the 150 nm gold spheres, the particles were assembled at the rim of the structure as shown by the orange dashed line in Figure 7.8 (c). The three insets depict SEM images of a double-rod, a single rod and a spherical particle. From a total of 7 assembled particles only two were single nanorods and three were agglomerates consisting of $\leq 4$ nanorods.

## 7.5 Overlay of two silver nanorods

The size and shape of a plasmonic nanoparticle are not the only parameters which influence the optical response of nanoparticles. The scattering and absorbance cross-sections also depended on the relative permittivity of the surrounding medium and the particle. The scattering cross-section of silver e.g. is even larger than that of gold, which makes silver nanoparticles particularly interesting for optical sensing applications such as surface-enhanced Raman scattering (SERS) [158]. To demonstrate the tracking, trapping and assembly of silver nanoparticles we purchased pentagonal silver nanorods with a plasmon peak at $\approx 780\,\text{nm}$ and a diameter of $\approx 45\,\text{nm}$ (Sciventions). The nanorods were synthesized by thermal regrowth of decahedral silver nanoparticle in an aqueous solution, using citrate as a reducing agent [159].

The advantages of patterning the topography by tSPL are not only the high resolution and the capability of patterning 3D structures, but also the ability to detected the residual topography of an buried structure. Rawlings et al. have shown theoretically and experimentally that spin coating across features with a width below $20\,\mu\text{m}$ results in a remaining topography, which is vertically aligned with the buried structure [160]. This feature can be used to precisely

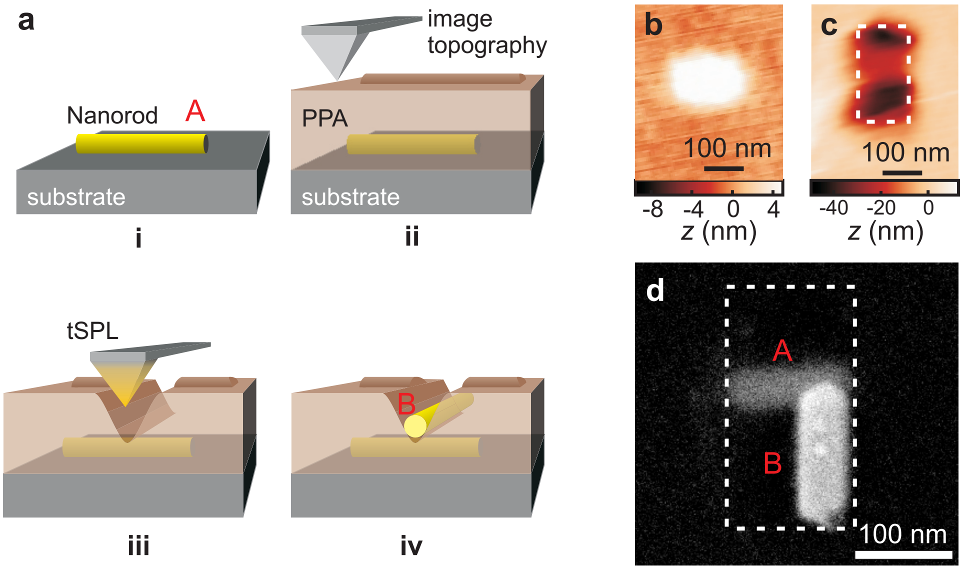

FIGURE 7.9: (a) Process flow of the overlay of two nanorods. (i) Particle (A) is deposited by droplet drying. (ii) A PPA film is spin coated on top of the pre-assembled particle. A remaining topography exists at the location of the particle, which is used to align the assembly structure for the second particle (iii). (iv) The second nanorod is placed perpendicular on top of the first particle. (b, c) Topographical tSPL images after (b) the spin coating and (c) patterning the trap. (d) The SEM image shows the position of the first deposited nanorod (A) and the on top assembled nanorod (B). The pentagonal silver nanorods have a diameter of $\approx 40\,\text{nm}$ and a length of $\approx 150\,\text{nm}$. The position and shape of the topographical trap is indicated by the dashed white line.

pattern a topographical trap to assemble a nano- or micro-objects in alignment with another structure. Figure 7.9 (a) shows the process flow of stacking one nanorod on top of another:

(i) First, several nanorods were deposited on a piece of a silicon wafer, by droplet drying.

(ii) Second, a 65 nm thick PPA film was spin-coated on top of the sample. At the location of a buried nanorod, a small bump in the PPA surface was measured by means of a scanning probe technique, e.g. tSPL (see Figure 7.9 (b)).

(iii) The combination of imaging and writing with the same tool allowed us to precisely pattern a topographical trap at the center and perpendicular to the first assembled nanoparticle (see Figure 7.9 (c)).

(iv) Using the topographical trap and our NCA, a second particle was placed on top of the first assembled particle (see Figure 7.9 (d)).

The nanorod (A) in the SEM image is the one which was buried and the second particle was first partially immobilized to the cover-glass and then, by using the lateral piezo stage, delivered to the trap. In principle, this restricts the mobility of the particle and thus the alignment with respect to the trap. However, experimentally we observed strong contrast fluctuations of the nanorod at larger gap distances, which indicated that only one end of the particle was connected to the cover-glass and that the nanorod was still capable of performing a precision around this point. Therefore, the alignment was done by means of electrostatic repulsion. Both nanorods were almost vertically aligned; the deviation was only $\approx 4°$. The lateral displacement was around 80 nm, which could easily be improved by a narrower trap geometry.

## 7.6 Semiconductor nanowires placed on electrodes

The aim of this section is to place nanowires on top of pre-patterned electrodes. A highly doped silicon substrate was used; to prevent a short-circuiting of the devices, a 135 nm thick layer of $SiO_2$ and 5 nm of $HfO_2$ were evaporated on top of the silicon substrate. Subsequently, a $\approx$ 5 nm Cr adhesion layer and a $\approx$ 20 nm thick gold layer was evaporated. The metal layers were patterned into several pairs of $\gtrsim 1\,\mu$m wide electrodes, which face each other at a distance of $\gtrsim 1\,\mu$m by using optical lithography. In an next step a 135 nm thick PPA film was spin coated on top of the substrate.

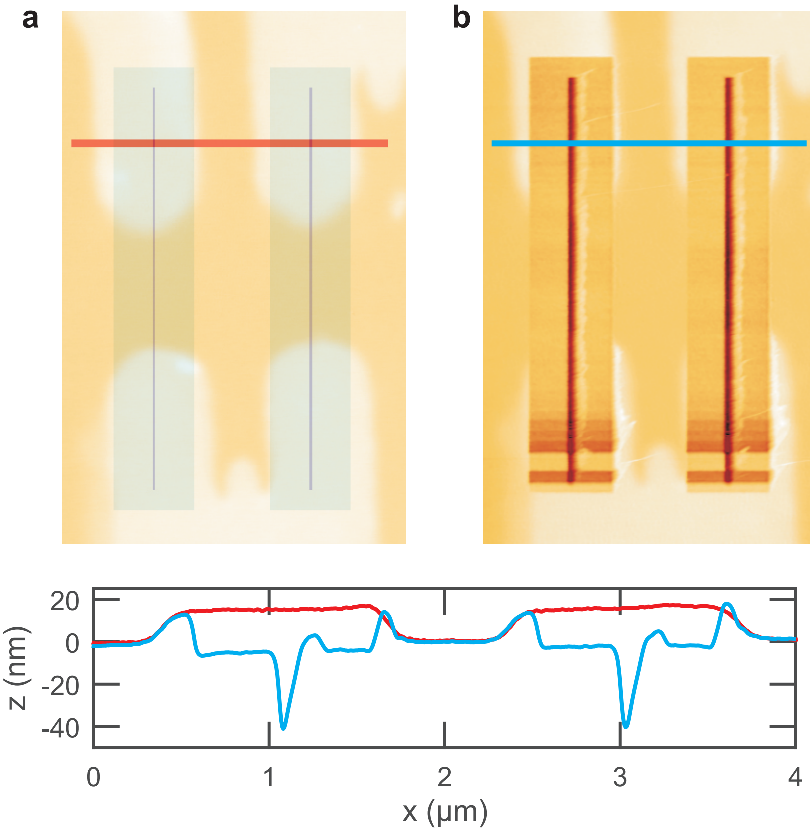

FIGURE 7.10: Overlay of traps on electrodes. (a) tSPL image of the surface of a 135 nm thick PPA film, which is spin coated on top of the ≈ 25 nm thick electrodes. The position of the buried electrodes is detected by measuring a remaining topography of ≈ 17 nm. The transparent blue lines indicate the intended positions of the traps. (b) The traps for the assembly of the nanowires are overlayed with nanometer precision. (a,b) The sub panel shows the cross section along the (a) red and (b) blue line.

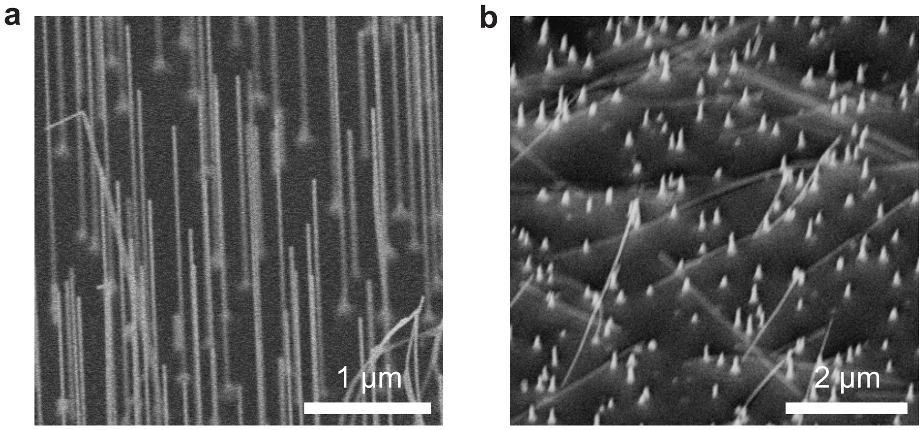

FIGURE 7.11: Harvesting of nanowires. (a) SEM image of InAs nanowires grown on a InAs wafer. The wires are approximately $4.3\,\mu$m long and have a diameter of $\approx$ 35 nm. The wires are coated with 3 nm $Al_2O_3$ and 3 nm $SiO_2$. (b) The nanowires are harvested by shearing a frozen drop of ultrapure water. (a, b) For the imaging the sample was tilted by $45°$.

The optical detection system of the tSPL tool was used to coarsely position the patterning tip, close to the end of the micon sized electrodes, which were buried under the PPA layer. The surface topography imaged with the tip of the tSPL is shown in Figure 7.10 (a). The intended position of the traps with respect to the electrodes is illustrated by the transparent blue overlay. Figure 7.10 (b) shows the topography after the tSPL patterning. The measured cross section before and after the patterning is indicated in the sub panel of Figure 7.10 by the red and blue line, respectively. The elongated traps were $\approx 5\,\mu$m long and had a maximum depth of $\approx 40$ nm; this dimensions were chosen due to the size of the InAs nanowires, which were grown at IBM Research - Zurich.

The InAs nanowires were grown epitaxially by using gold seed particles, which act as collectors of vapour-phase precursor materials [161]. The growth was initiated as soon as the precursor gases arsine ($AsH_3$) and trimethylindium (TMIn) were available at a growth temperature of 430 °C. The wires were also coated with 3 nm $Al_2O_3$ and 3 nm $SiO_2$. The high-$\kappa$ dielectric $Al_2O_3$ is well suited for gating, yet it has an isoelectric point close to $\mathrm{pH} \approx 9$ [162], which means that the surface does only develop a negative charge in a very basic solution. A second oxide layer (silicon dioxide) was added, which has an isoelectric point around $\mathrm{pH} \approx 2$ [162].

Figure 7.11 (a) shows an SEM image of the InAs nanowires grown on a (111) InAs substrate with a density of $\leq 9$ per $\mu\mathrm{m}^2$. The wires were approximately $4.3\,\mu$m long and had a diameter of $\approx 35\,\text{nm}$. The wires were harvested by first freezing a drop of ultrapure water (Millipore) on a small substrate piece. The drop was frozen by letting the sample float in a metal dish on liquid nitrogen. Two different methods were used to obtain a final suspension of nanowires. Either the frozen drop was sheared off with tweezers before it started to melt or it was waited until the frozen drop was molten. Some of the wires seem to break during the freezing or melting due to thermal expansion, since later observation of the not sheared suspension contained nanowires of similar length, yet the concentration was much lower. Figure 7.11 (b) shows that most of the nanowires are harvested after shearing the frozen drop. For the assembly experiments we harvested the nanowires from $\approx 3 \times 3\,\text{mm}^2$ large samples, which should provide $\approx 80$ million nanowires. For stable conditions we typically work with $\geq 20\,\mu\text{l}$ colloidal suspensions and the suspension has to be confined to gap distances below $d \leq 500\,\text{nm}$, which should result in $\leq 9$ nanowires for the entire field of view ($\approx 65 \times 65\,\mu\text{m}^2$). However, due to agglomeration and adsorption to the surfaces we typically observed only around one nanowire at such a confinement.

The nanowire suspension was placed on the patterned sample and confined in the NCA. Figure 7.12 (a) shows the transport of a nanowire from the left hand side along the yellow dotted trajectory to the electrodes on the right hand side. The insets show images of the same nanowire at different locations (inside the red boxes). The tracking of the nanowire was done by using some of the Matlab Image Processing Toolbox functions. First, we determined the contrast of the nanowire by subtracting a background image as described in Section 4.5. Second, the edges of the nanowire in the contrast image were determined by using the Canny edge detection algorithm, which generated a binary image [163]. Third, we performed the Standard Hough Transform on the binary image, which generated a so-called accumulator space of how many points lie on a line with a particular distance to the origin and angle towards the x-axis. Line candidates were determined by local maxima in the parameter space. The ten most dominant peak values, with a minimum line length similar to the length of the nanowire, are depicted by the light blue lines in Figure 7.12 (a). The average of all detected lines is shown by the dark blue line; this line was used to determine the central position and orientation angle of the nanowire.

The position as well as the orientation of the nanowire were affected by Brownian motion and an electro-osmotic flow. The electro-osmotic flow was generated in either x- or y-direction by applying a square wave-voltage ±0.1V 5 Hz on top of a constant voltage of +0.1 V. The light blue and light red regions in Figure 7.12 (b) indicate when these potentials were switched on. The effective motion of the

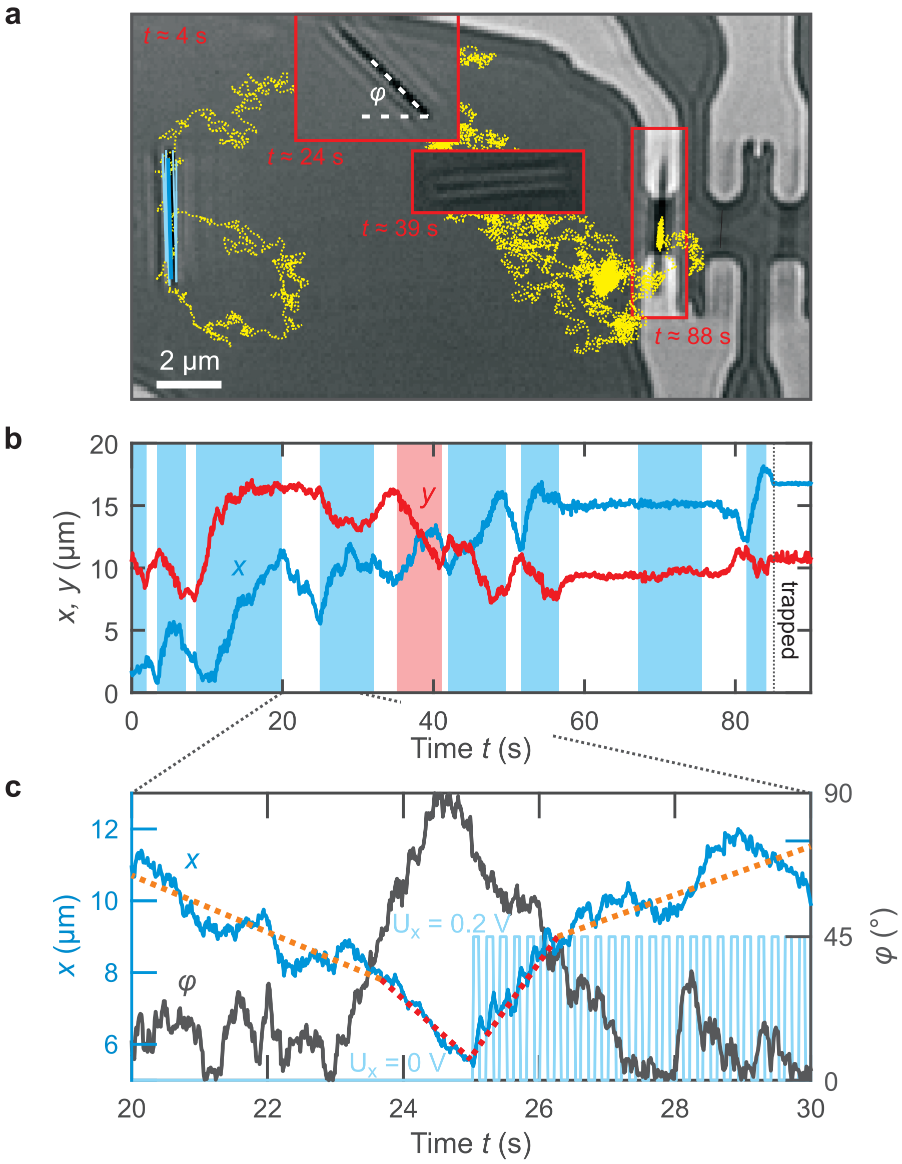

FIGURE 7.12: Transport of a nanowire to the trap. (a) Optical images of a nanowire in our NCA. The blue lines depict the detected nanowire position and orientation. The dotted yellow line shows the trajectory of center of mass of the nanowire and the insets show the nanowire at at a particular time. The wire was trapped after $\gtrsim$ 85 s in the PPA grove across two electrodes. (b) The x and y position of the nanowire as a function of time is depicted by the blue and red line, respectively. The nanowire was directed to the trap by applying a square wave-voltage of ±0.1V and 5 Hz on top of a constant potential +0.1 V in either x- or y-direction as indicated by the light blue and light red regions, respectively. (c) The drag on the nanowire depended on its orientation towards the direction of the plug flow. As illustrated by the black line and the slope of the dotted orange/red lines, the more vertical the wire was aligned to the flow direction the larger was the drift of the nanowire. The effective transport was a result of switching the potentials on and off depending on the orientation of the wire.

counter-ions was towards the more negative electrode to compensate the effective potential. This induced a plug flow, which dragged the nanowires in the same direction. After switching the potential off the counter-ions diffused back and dragged the nanowire in the opposite direction. However, the drift of the nanowire was not linear and the net drift was towards the electrodes.

We had observed an orientation dependent drag of the nanowire, which was stronger if the nanowire was vertically aligned to the flow direction. Figure 7.12 (c) shows a typical section of the x-position and the angle $\phi$ between the nanowire and the x-axis. The dotted orange and red lines are guides to the eye. The higher slope of the dotted red lines indicates an increased drift when the nanowire was aligned more vertically ($\phi > 45\,°$), while it was reduced for a more horizontal alignment (dotted orange lines, $\phi < 45\,°$). By selectively switching the electrical field on and off, the particle was transported towards the electrodes. It is important to note that the electric field induced a torque on the polarized nanowire, which tried to align the nanowire parallel to the electric field (flow direction). This force was exploited in dielectrophoretic trapping [39]. However, in our case the applied field strength was $\gtrsim 100$ times smaller and the Brownian motion dominated the reorientation of the nanowire. By taking care that the nanowire was in the proximity of a particular polymer groove and by setting the trapping strength with the gap distance, we could select in which groove the nanowire was trapped. The gap distance was reduced from $d \approx 380\,\mathrm{nm}$ to $d \approx 300\,\mathrm{nm}$, during the transport of the nanowire shown in Figure 7.12.

Figure 7.13 (a) shows the assembled nanowire inside the trap at the left hand side. In this case, it was not a single nanowire but two nanowires next to each other. The double-wire was deposited by reducing the gap distance until it was in direct contact with both confining surfaces. In a second and third transport and assembly step the two bundles of nanowires were placed next to the double-wire.

We found that the nanowires preferentially sticked to the polymer in case the dimensions of the topographical trap matched the geometry of the assembled object or if parts of the wire were pressed into the PPA as depicted in Figure 7.13 (b,c). The cross sections along the green and blue lines are shown in Figure 7.13 (d). The black dashed line shows the cross-section of the nanowire after the evaporation of the PPA as shown in Figure 7.13 (f). This reveals that the nanowire sits on the polymer surfaces at the position of the light green line and that up to 50 % of the nanowire were pressed into the polymer at the lowest position of the cover-glass at the location of the dark blue line. 25 – 33 % of the compression was elastic, since the final height is $\approx 7\,\mathrm{nm}$ higher. This is in

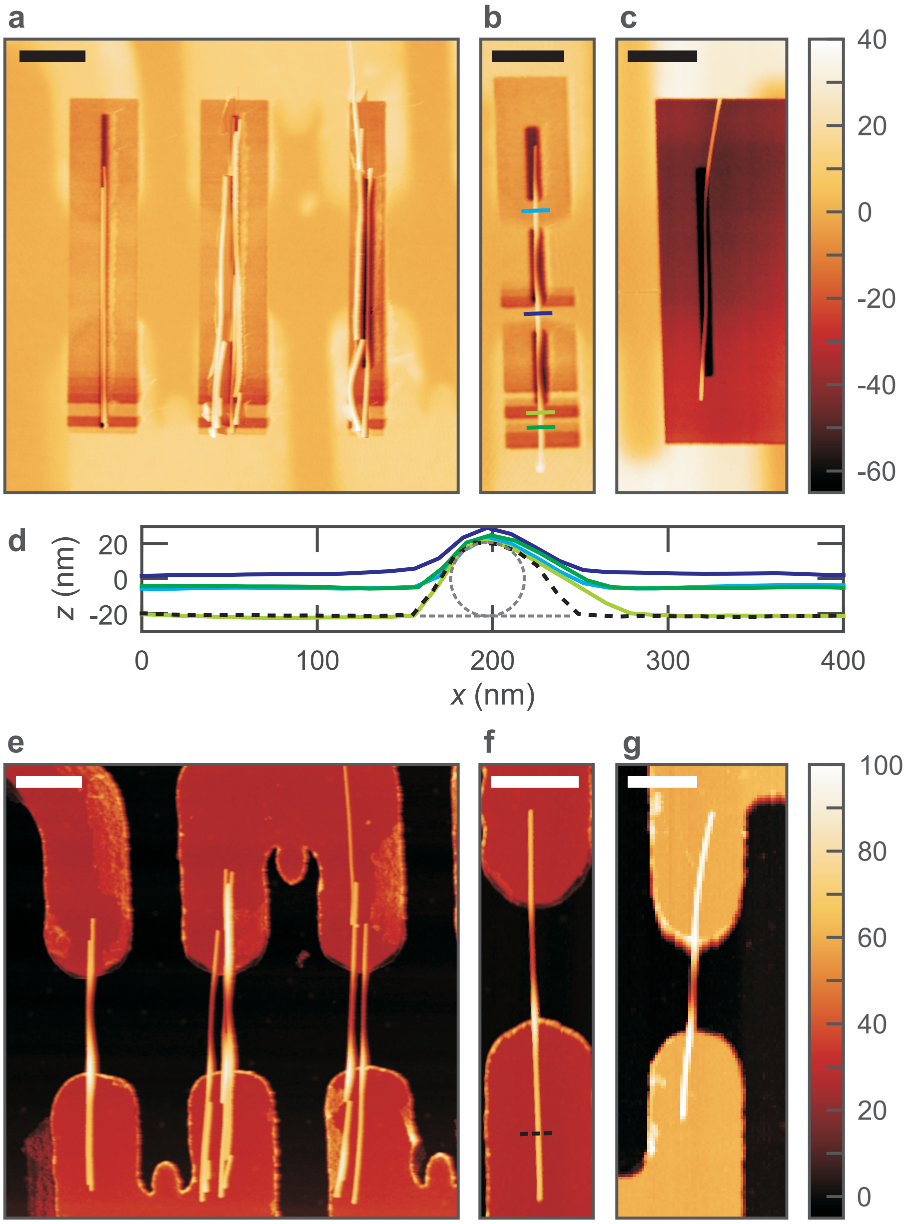

FIGURE 7.13: Assembled InAs nanowires. (a) AFM image of a double-wire and two bundles of several nanowires deposited inside PPA traps. (b, c) Two single nanowires are deposited on the polymer surface, they are pressed into the PPA, which increases the adhesion. (d) Cross sections along the green and blue lines in (b) and the dashed black line in (f). The dashed black line has an offset for clarity. (e - g) The PPA film is evaporated heating the sample $\approx$ 220° C on a hot plate for 10 s. The wires connect two electrodes. In (f) and (g), the electrodes have a thickness of 27 nm and 60 nm, and the single nanowires have a diameter of 39 nm and 40 nm, respectively. (a - f) The scale bars are 1 $\mu$m.

agreement with the observations we have already made for the 60 nm gold spheres (see Section 7.2.3).

Another single nanowire is shown in Figure 7.13 (c). Here, the wire was assembled on a sample with $\approx$ 60 nm thick electrodes and a $\approx$ 230 nm thick PPA film. In order to place the nanowires on the electrodes, the PPA film was evaporated. This was done by placing the sample for 10 s on a hot plate with a Temperature of $\approx$ 220 °C. Figure 7.13 (e,f,g) shows AFM topography images of the assembled nanowires. The evaporation of the polymer film has altered their lateral position only marginal.

## 7.7 Conclusion

In summary, we have demonstrated the controlled trapping and precise placement of several spherical and elongated nanoparticles into 3D guiding structures by exploiting the gap distance dependent interaction energies in a nanofluidic slit. The particles are confined between a glass and a polymer surface and the electrostatic interactions are shaped into a potential well by a recessed structure in the polymer layer. The depth of the well increases with the decreasing gap distance and keeps the particles tightly trapped. When the particles are almost in direct contact with the confining surfaces, Van der Waals forces dominates electrostatic interactions and the particles jump into contact with the guiding structures.

A challenge for the presented method is the transport of particles to the assembly site. Only a small volume of colloidal suspension is confined under the glass mesa at gap distances, which are required to trap the particles. We demonstrate that the Brownian ratchets are capable of increasing the concentration of spheres at the targeted assembly site. At gap distances of $d_{IBM} \gtrsim 100$ nm the particles are trapped in 10 nm deep conical recesses for a finite time. The short illumination time enables an almost instantaneous measurement of the particle positions with high frequency. As a result the absolute trapping energies of the few $k_B T$ deep potential wells can be determined via the Boltzmann relation. A strong enhancement of the trapping energy is observed for shorter gap distances. Furthermore, exploiting the known effect of motion blur on detected particle positions in a harmonic potential due to a finite illumination time, we are capable of obtaining motion blur and detection noise free particle positions, which are in particular important to estimate the exponential decay of the trapping stiffness. Interestingly, a correlation between narrower trap width in the y-direction and increased particle confinement is observed, although the full width at half maximum of the average trap is less than the diameter of the particles. The average particle diameter is $2a = 58.6 \pm 6.2\,\mathrm{nm}$ (see Figure 3.8) and the average trap (see Figure 7.4 (c)) has a full width at half maximum of FWHM-$x \approx 58\,\mathrm{nm}$ and FWHM-$y \approx 34\,\mathrm{nm}$. The assembly of spheres and nanorods in a few times larger topographical structures revealed that the placement precision was significantly deteriorated due to a preferential deposition close to the rim of the guiding structures.

The interference signal of light reflected from the substrate and glass surface with light scattered by the 60 nm spheres is used to determine the axial position during the assembly process. In Section 4.7 we have already observed that the spheres preferentially occupy the space closer to the cover-glass at gap distances between $90\,\mathrm{nm} \lesssim d \lesssim 200\,\mathrm{nm}$. In this Section we have shown that this is also the case for shorter gap distances, which further indicates that the polymer surface develops a larger surface charge than the glass surface. Unfortunately, such conditions require short gap distances of $d_{\mathrm{IBM}} \approx 52\,\mathrm{nm}$ for the particles to jump between 5 and 9 nm into contact with the polymer surface. However, the thermally excited particle only jump once, which indicates a stronger adhesion to the polymer due to an increased contact region. In total 34 spheres were placed with a pitch of 200 nm and a sub 10 nm precision to form the letters IBM.

Furthermore, the tSPL patterning technique provides the capability of detecting the remaining topography of a buried structure and enables the precise patterning of traps with regard to the existing structure. The prospects of such a patterning technique in combination with the presented assembly process are demonstrated by placing a nanorod vertically aligned on top of another nanorod. The method is further utilized by patterning elongated traps above two separated electrodes and assembling well aligned InAs nanowires into this guiding structures with high precision. Finally, the thermal decomposable polymer was evaporated at moderate temperature and the nanowires were placed directly on the electrodes.

# 8 Final remarks and outlook

In the introduction several assembly techniques were mentioned, which are capable of placing nanoparticles on a substrate. Some of these techniques are capable of placing large quantities of particles in parallel, while others provide more control over the position of individual particles. However, most of these techniques focus on a certain type of nanoparticle and provide only a very limited insight into the dynamics during the assembly, which makes it difficult to optimize the involved parameters. In this thesis an apparatus and method was presented which is not only capable of placing different types of nanoparticles with high precision but also facilitates the observation of the particles during the entire assembly process. It is the combination of tunable confinement and optical access which distinguishes the presented setup from other implementations and defines the significance of the presented work.

The capability of detecting the position of 60 nm spheres in all three dimensions with high spatio-temporal resolution was shown in Chapter 4. Due to the high sensitivity of the interference signal short illumination times are achievable. This provides almost instantaneous particle positions, which enables an *in-situ* access to the 3D free energy landscape of the system at the individual particle level and as a function of confinement. This opens up new possibilities to study in great detail the behavior of individual confined nano-objects as a function of various system parameters. These parameters include not only the nature of the particles and confining surfaces, but also the application of external electric or magnetic fields. Similarly, laterally inhomogeneous surfaces patterned by topography, charge or magnetic moments are also accessible. Using the NCA, these systems can be studied as a function of confinement, which will be important to separate effects arising from the charged surfaces and the electric or magnetic fields [79].

The measurements in Chapter 5 on a sub-diffusive behavior induced by surface roughness and a gap distance dependent electro-viscous effect, which hinders the diffusion of nanoparticles, concern the transport of all kind of nanoscale objects in different nanofluidic systems with a low ionic strength. In general, the shown results demonstrate the versatility of this tool which in future experiments can be used to characterize the transport of particles in dependence of surface morphology or hydrophobicity [93]. It is also easy to envision that the detection of biomolecular behavior in the presented tunable slit could realize the investigation of phenomena such as selective permeability, hydrodynamic friction, liquid slip, modified electroosmotic velocity, and dielectrophoresis under reliable conditions [136].

The realization of the first rocking Brownian ratchet to efficiently transport nanoparticles has been demonstrated in Chapter 6. Further experiments have shown that this concept can not only be used to control the transport of a certain type of particle, but also to separate different types in dependence of their charge and size. Others have already demonstrated the potential of controlled mixing of spatially isolated reagents, which optimized the efficiency of multistep synthetic processes in a microreactor [164]. The demonstrated nanofluidic Brownian ratchets might lay the foundation of future nanoreactors or provide the platform to investigate novel biological or chemical reactions.

Finally, in Chapter 7 the motion of diffusing particles was confined in all three dimensions by an electrostatic trapping potential. The tuning of the gap distance enabled not only the assembly of 60 nm gold spheres with a sub 10 nm precision, but also the variation of the trapping stiffness between $15 \lesssim k \lesssim 150\,\mathrm{fN/nm}$. Similar to optical tweezers such a low stiffness would facilitate the usage of trapped particles as highly sensitive sensors e.g. for the detection of acoustic vibrations [165]. The passive topographical trapping has a big advantage compared to the optical tweezers, since no energy is consumed for the trapping itself, while the active traps of optical tweezers require strong electromagnetic fields. In terms of assembly technique, still some obstacles have to be overcome until the presented method will be capable of fabricating competitive integrated nanowire circuits. It requires billions of monodisperse suspended nanowires, the same amount of patterned traps and a efficient and reliable transport process such that all traps can be filled at gap distances where sufficient trapping potentials are developed. Nevertheless, the apparatus could be already used to build complex plasmonic structures or novel nanowire sensors.

# Bibliography

[1] D. V. Talapin et al. “Prospects of colloidal nanocrystals for electronic and optoelectronic applications”. In: *Chemical reviews* 110.1 (2009), pp. 389–458.

[2] E. Jang et al. “White-Light-Emitting Diodes with Quantum Dot Color Converters for Display Backlights”. In: *Advanced materials* 22.28 (2010), pp. 3076–3080.

[3] T.-H. Kim et al. “Full-colour quantum dot displays fabricated by transfer printing”. In: *Nature photonics* 5.3 (2011), pp. 176–182.

[4] M. E. Stewart et al. “Nanostructured plasmonic sensors”. In: *Chemical reviews* 108.2 (2008), pp. 494–521.

[5] X. Huang, S. Neretina, and M. A. El-Sayed. “Gold Nanorods: From Synthesis and Properties to Biological and Biomedical Applications”. In: *Adv. Mater.* 21.48 (Dec. 2009), pp. 4880–4910.

[6] A. V. Krasavin and A. V. Zayats. “Photonic Signal Processing on Electronic Scales: Electro-Optical Field-Effect Nanoplasmonic Modulator”. In: *Phys. Rev. Lett.* 109 (5 2012), p. 053901.

[7] M. Z. Alam, J. S. Aitchison, and M. Mojahedi. “A marriage of convenience: Hybridization of surface plasmon and dielectric waveguide modes”. In: *Laser & Photonics Reviews* 8.3 (2014), pp. 394–408.

[8] K. Saha et al. “Gold nanoparticles in chemical and biological sensing”. In: *Chemical reviews* 112.5 (2012), pp. 2739–2779.

[9] P. D. Howes, R. Chandrawati, and M. M. Stevens. “Colloidal nanoparticles as advanced biological sensors”. In: *Science* 346.6205 (2014), p. 1247390.

[10] S. Natarajan et al. “A 14nm logic technology featuring 2 nd-generation FinFET, air-gapped interconnects, self-aligned double patterning and a 0.0588 $\mu$m 2 SRAM cell size”. In: *2014 IEEE International Electron Devices Meeting*. IEEE. 2014, pp. 3–7.

[11] W. Lu, P. Xie, and C. M. Lieber. “Nanowire transistor performance limits and applications”. In: *IEEE transactions on Electron Devices* 55.11 (2008), pp. 2859–2876.

[12] M. C. Wang and B. D. Gates. “Directed assembly of nanowires”. In: *Materials Today* 12.5 (2009), pp. 34 –43.

[13] A. D. Franklin et al. "Sub-10 nm carbon nanotube transistor". In: *Nano letters* 12.2 (2012), pp. 758–762.

[14] W. Lu and C. M. Lieber. "Nanoelectronics from the bottom up". In: *Nature materials* 6.11 (2007), pp. 841–850.

[15] Y. Chen et al. "Sensing and energy harvesting of fluidic flow by InAs nanowires". In: *Nano letters* 13.8 (2013), pp. 3953–3957.

[16] Y. Cui et al. "Nanowire nanosensors for highly sensitive and selective detection of biological and chemical species". In: *Science* 293.5533 (2001), pp. 1289–1292.

[17] N. Vogel et al. "Advances in colloidal assembly: the design of structure and hierarchy in two and three dimensions". In: *Chemical reviews* 115.13 (2015), pp. 6265–6311.

[18] M. Grzelczak et al. "Directed self-assembly of nanoparticles". In: *ACS nano* 4.7 (2010), pp. 3591–3605.

[19] B. D. Hatton and J. Aizenberg. "Writing on superhydrophobic nanopost arrays: Topographic design for bottom-up assembly". In: *Nano letters* 12.9 (2012), pp. 4551–4557.

[20] A. V. Pinheiro et al. "Challenges and opportunities for structural DNA nanotechnology". In: *Nature nanotechnology* 6.12 (2011), pp. 763–772.

[21] K. Flöhr et al. "Manipulating InAs nanowires with submicrometer precision". In: *Review of scientific instruments* 82.11 (2011), p. 113705.

[22] J. Yao et al. "Nanowire nanocomputer as a finite-state machine". In: *Proceedings of the National Academy of Sciences* 111.7 (2014), pp. 2431–2435.

[23] J. Yao, H. Yan, and C. M. Lieber. "A nanoscale combing technique for the large-scale assembly of highly aligned nanowires". In: *Nature nanotechnology* 8.5 (2013), pp. 329–335.

[24] Y. Zhao et al. "Shape-controlled deterministic assembly of nanowires". In: *Nano letters* 16.4 (2016), pp. 2644–2650.

[25] W. Zhou, C. Rutherglen, and P. J. Burke. "Wafer scale synthesis of dense aligned arrays of single-walled carbon nanotubes". In: *Nano Research* 1.2 (2008), pp. 158–165.

[26] M. M. Shulaker et al. "Carbon nanotube computer". In: *Nature* 501.7468 (2013), pp. 526–530.

[27] A. D. Franklin and Z. Chen. "Length scaling of carbon nanotube transistors". In: *Nature nanotechnology* 5.12 (2010), pp. 858–862.

[28] Q. Cao et al. "Medium-scale carbon nanotube thin-film integrated circuits on flexible plastic substrates". In: *Nature* 454.7203 (2008), pp. 495–500.

[29] A. Tao et al. "Langmuir-Blodgett silver nanowire monolayers for molecular sensing using surface-enhanced Raman spectroscopy". In: *Nano Letters* 3.9 (2003), pp. 1229–1233.

[30] D. Whang et al. “Large-scale hierarchical organization of nanowire arrays for integrated nanosystems”. In: *Nano letters* 3.9 (2003), pp. 1255–1259.

[31] K. Lenzmann F.and Li, A. H. Kitai, and H. D. H. Stover. “Thin-film micropatterning using polymer microspheres”. In: *Chemistry of Materials* 6.2 (1994), pp. 156–159.

[32] S. M. Weekes et al. “Macroscopic arrays of magnetic nanostructures from self-assembled nanosphere templates”. In: *Langmuir* 23.3 (2007), pp. 1057–1060.

[33] Y. Cui et al. “Integration of colloidal nanocrystals into lithographically patterned devices”. In: *Nano Letters* 4.6 (2004), pp. 1093–1098.

[34] T. Kraus et al. “Nanoparticle printing with single-particle resolution”. In: *Nature nanotechnology* 2.9 (2007), pp. 570–576.

[35] C. Kuemin et al. “Oriented Assembly of Gold Nanorods on the Single-Particle Level”. In: *Advanced Functional Materials* 22.4 (2012), pp. 702–708.

[36] F. Holzner et al. “Directed Placement of Gold Nanorods Using a Removable Template for Guided Assembly”. In: *Nano Letters* 11.9 (2011), pp. 3957–3962.

[37] K. Heo et al. “Large-scale assembly of silicon nanowire network-based devices using conventional microfabrication facilities”. In: *Nano letters* 8.12 (2008), pp. 4523–4527.

[38] H. Park et al. “High-density integration of carbon nanotubes via chemical self-assembly”. In: *Nature nanotechnology* 7.12 (2012), pp. 787–791.

[39] E. M. Freer et al. “High-yield self-limiting single-nanowire assembly with dielectrophoresis”. In: *Nat. Nano* 5.7 (July 2010), pp. 525–530.

[40] M. Li et al. “Bottom-up assembly of large-area nanowire resonator arrays”. In: *Nature Nanotechnology* 3.2 (2008), pp. 88–92.

[41] P. Li and W. Xue. “Selective deposition and alignment of single-walled carbon nanotubes assisted by dielectrophoresis: from thin films to individual nanotubes”. In: *Nanoscale research letters* 5.6 (2010), p. 1072.

[42] A. Ashkin. “Acceleration and trapping of particles by radiation pressure”. In: *Physical review letters* 24.4 (1970), p. 156.

[43] A. S. Urban et al. “Optical trapping and manipulation of plasmonic nanoparticles: fundamentals, applications, and perspectives”. In: *Nanoscale* 6.9 (2014), pp. 4458–4474.

[44] A. S. Urban et al. “Laser printing single gold nanoparticles”. In: *Nano letters* 10.12 (2010), pp. 4794–4798.

[45] S. Nedev et al. “Optical force stamping lithography”. In: *Nano letters* 11.11 (2011), pp. 5066–5070.

[46] J. Do et al. “Two-color laser printing of individual gold nanorods”. In: *Nano letters* 13.9 (2013), pp. 4164–4168.

[47] S. Weisenburger and V. Sandoghdar. "Light microscopy: an ongoing contemporary revolution". In: *Contemporary Physics* 56.2 (2015), pp. 123–143.

[48] V. Jacobsen et al. "Interferometric optical detection and tracking of very small gold nanoparticles at a water-glass interface". In: *Opt. Express* 14.1 (2006), pp. 405–414.

[49] P. Kukura. "High-speed nanoscopic tracking of the position and orientation of a single virus". In: *Nat. Methods* 6 (2009), pp. 923–927.

[50] M. Celebrano et al. "Single-molecule imaging by optical absorption". In: *Nature Photonics* 5.2 (2011), pp. 95–98.

[51] M. Piliarik and V. Sandoghdar. "Direct optical sensing of single unlabelled proteins and super-resolution imaging of their binding sites". In: *Nat. Commun.* 5 (2014), p. 4495.

[52] G. Daaboul et al. "High-throughput detection and sizing of individual low-index nanoparticles and viruses for pathogen identification". In: *Nano letters* 10.11 (2010), pp. 4727–4731.

[53] J. Andrecka et al. "Structural dynamics of myosin 5 during processive motion revealed by interferometric scattering microscopy". In: *Elife* 4 (2015), e05413.

[54] M. Krishnan et al. "Geometry-induced electrostatic trapping of nanometric objects in a fluid". In: *Nature* 467.7316 (2010), pp. 692–695.

[55] N. Mojarad, V. Sandoghdar, and M. Krishnan. "Measuring three-dimensional interaction potentials using optical interference". In: *Opt. Express* 21.8 (2013), pp. 9377–9389.

[56] J. N. Israelachvili. *Intermolecular and Surface Forces*. London: Academic Press, 1992.

[57] Y. Liang et al. "Interaction forces between colloidal particles in liquid: Theory and experiment". In: *Advances in colloid and interface science* 134 (2007), pp. 151–166.

[58] L. Bergström. "Hamaker constants of inorganic materials". In: *Advances in Colloid and Interface Science* 70 (1997), pp. 125–169.

[59] D. Pires et al. "Ultraflat templated polymer surfaces". In: *Langmuir* 25.9 (2009), pp. 5141–5145.

[60] S. H. Behrens and D. G. Grier. "The charge of glass and silica surfaces". In: *J. Chem. Phys* 115.14 (2001), p. 6716.

[61] Z. Adamczyk and P. Warszyński. "Role of electrostatic interactions in particle adsorption". In: *Adv. Colloid Interface Sci.* 63 (1996), pp. 41–149.

[62] H. Ohshima, T. W. Healy, and L. R. White. "Accurate analytic expressions for the surface charge density/surface potential relationship and double-layer potential distribution for a spherical colloidal particle". In: *Journal of Colloid and Interface Science* 90.1 (1982), pp. 17–26.

[63] G. Bell, S Levine, and L. McCartney. "Approximate methods of determining the double-layer free energy of interaction between two charged colloidal spheres". In: *J. Colloid Interface Sci.* 33.3 (1970), pp. 335–359.

[64] A. Einstein. "Über die von der molekularkinetischen Theorie der Wärme geforderte Bewegung von in ruhenden Flüssigkeiten suspendierten Teilchen". In: *Annalen der Physik* 322.8 (1905), pp. 549–560.

[65] R. Metzler and J. Klafter. "The random walk's guide to anomalous diffusion: a fractional dynamics approach". In: *Physics reports* 339.1 (2000), pp. 1–77.

[66] S. L. Eichmann, S. G. Anekal, and M. A. Bevan. "Electrostatically Confined Nanoparticle Interactions and Dynamics". In: *Langmuir* 24.3 (2008), pp. 714–721.

[67] Y. Pawar and J. L. Anderson. "Hindered diffusion in slit pores: an analytical result". In: *Industrial & Engineering Chemistry Research* 32.4 (1993), pp. 743–746.

[68] H. Faxèn. "Die Bewegung einer starren Kugel längs der Achse eines mit zäher Flüssigkeit gefüllten Rohres". In: *Ark. Mat. Astron. Fys.* 17.27 (1923).

[69] A. Goldman, R. Cox, and H. Brenner. "Slow viscous motion of a sphere parallel to a plane wall: Motion through a quiescent fluid". In: *Chemical Engineering Science* 22.4 (1967), pp. 637 –651.

[70] C. W. Oseen. *Neuere Methoden und Ergebnisse in der Hydrodynamik.* Akademische Verlagsgesellschaft, Leipzig, 1927.

[71] L. Lobry and N. Ostrowsky. "Diffusion of Brownian particles trapped between two walls: Theory and dynamic-light-scattering measurements". In: *Phys. Rev. B* 53 (18 1996), pp. 12050–12056.

[72] B. Lin, J. Yu, and S. A. Rice. "Direct measurements of constrained Brownian motion of an isolated sphere between two walls". In: *Phys. Rev. E* 62 (3 2000), pp. 3909–3919.

[73] F. Perrin. "LE RAD1UM". In: (1934).

[74] M. O. Magnasco. "Forced thermal ratchets". In: *Phys. Rev. Lett.* 71 (10 1993), pp. 1477–1481.

[75] R. Astumian. "Thermodynamics and kinetics of a brownian motor". In: *Science* 276 (1997), pp. 917–922.

[76] P. Reimann. "Brownian motors: noisy transport far from equilibrium". In: *Physics reports* 361.2 (2002), pp. 57–265.

[77] C Marquet et al. "Rectified motion of colloids in asymmetrically structured channels". In: *Physical review letters* 88.16 (2002), p. 168301.

[78] R. Bartussek, P. Hänggi, and J. G. Kissner. "Periodically rocked thermal ratchets". In: *EPL (Europhysics Letters)* 28.7 (1994), p. 459.

[79] S. Fringes, M. Skaug, and A. W. Knoll. "In situ contrast calibration to determine the height of individual diffusing nanoparticles in a tunable confinement". In: *Journal of Applied Physics* 119.2, 024303 (2016).

[80] H. Zhu et al. "Characterization of deep wet etching of fused silica glass for single cell and optical sensor deposition". In: *Journal of Micromechanics and Microengineering* 19.6 (2009), p. 065013.

[81] C. Rawlings et al. "Fabrication of nanometer-accurate 3D profiles using closed-loop thermal scanning probe lithography". To be published.

[82] A. W. Knoll et al. "Closed-loop high-speed 3D thermal probe nanolithography". In: *Proc. SPIE* 9049 (2014), 90490B–90490B–8.

[83] D. Pires et al. "Nanoscale Three-Dimensional Patterning of Molecular Resists by Scanning Probes". In: *Science* 328.5979 (2010), pp. 732–735.

[84] A. W. Knoll et al. "Probe-Based 3-D Nanolithography Using Self-Amplified Depolymerization Polymers". In: *Advanced Materials* 22.31 (2010), pp. 3361–3365.

[85] J. Turkevich, P. C. Stevenson, and J. Hillier. "A study of the nucleation and growth processes in the synthesis of colloidal gold". In: *Discussions of the Faraday Society* 11 (1951), pp. 55–75.

[86] G Frens. "Controlled nucleation for the regulation of the particle size in monodisperse gold suspensions". In: *Nature* 241.105 (1973), pp. 20–22.

[87] J. Turkevich. "Colloidal gold. Part II". In: *Gold Bulletin* 18.4 (1985), pp. 125–131.

[88] A. Apelblat and J. Barthel. "Conductance studies on aqueous citric acid". In: *Zeitschrift für Naturforschung A* 46.1-2 (1991), pp. 131–140.

[89] G. H. Zimmerman, H. Arcis, and P. R. Tremaine. "Limiting Conductivities and Ion Association Constants of Aqueous NaCl under Hydrothermal Conditions: Experimental Data and Correlations". In: *Journal of Chemical & Engineering Data* 57.9 (2012), pp. 2415–2429.

[90] A. O. Govorov et al. "Gold nanoparticle ensembles as heaters and actuators: melting and collective plasmon resonances". In: *Nanoscale Research Letters* 1.1 (2006), pp. 84–90.

[91] A. O. Govorov and H. H. Richardson. "Generating heat with metal nanoparticles". In: *Nano today* 2.1 (2007), pp. 30–38.

[92] S. Fringes, F. Holzner, and A. W. Knoll. "The Nanofluidic Confinement Apparatus: Studying confinement dependent nanoparticle behavior and diffusion". Submitted to Journal of Chemical Physics.

[93] L. Bocquet and P. Tabeling. "Physics and technological aspects of nanofluidics". In: *Lab on a Chip* 14.17 (2014), pp. 3143–3158.

[94] M. Baum et al. “Retrieving the intracellular topology from multi-scale protein mobility mapping in living cells”. In: *Nat. Commun.* 5 (2014), p. 4494.

[95] J. Karger and R. Valiullin. “Mass transfer in mesoporous materials: the benefit of microscopic diffusion measurement”. In: *Chem. Soc. Rev.* 42.9 (2013), pp. 4172–97.

[96] R. Li, J. A. Fowler, and B. A. Todd. “Calculated Rates of Diffusion-Limited Reactions in a Three-Dimensional Network of Connected Compartments: Application to Porous Catalysts and Biological Systems”. In: *Phys. Rev. Lett.* 113.2 (2014), p. 028303.

[97] S. R. P. Pavani, A. Greengard, and R. Piestun. “Three-dimensional localization with nanometer accuracy using a detector-limited double-helix point spread function system”. In: *Appl. Phys. Lett.* 95.2, 021103 (2009), p. 021103.

[98] Y. Shechtman et al. “Precise Three-Dimensional Scan-Free Multiple-Particle Tracking over Large Axial Ranges with Tetrapod Point Spread Functions”. In: *Nano Lett.* 15.6 (2015), pp. 4194–4199.

[99] Y. Shechtman et al. “Multicolour localization microscopy by point-spread-function engineering”. In: *Nature Photonics* (2016).

[100] F. Verpillat et al. “Dark-field digital holographic microscopy for 3D-tracking of gold nanoparticles”. In: *Opt. Express* 19.27 (2011), pp. 26044–26055.

[101] H. P. Kao and A. Verkman. “Tracking of single fluorescent particles in three dimensions: use of cylindrical optics to encode particle position.” In: *Biophys. J.* 67.3 (1994), pp. 1291–1300.

[102] B. Huang et al. “Three-dimensional super-resolution imaging by stochastic optical reconstruction microscopy”. In: *Science* 319.5864 (2008), pp. 810–813.

[103] L. Zhao et al. “Microscopic Movement of Slow-Diffusing Nanoparticles in Cylindrical Nanopores Studied with Three-Dimensional Tracking”. In: *Analytical Chemistry* 88.10 (2016), pp. 5122–5130.

[104] D. Axelrod. “Total internal reflection fluorescence microscopy in cell biology”. In: *Traffic* 2.11 (2001), pp. 764–774.

[105] S. L. Eichmann and M. A. Bevan. “Direct Measurements of Protein-Stabilized Gold Nanoparticle Interactions”. In: *Langmuir* 26.18 (2010), pp. 14409–14413.

[106] M. Speidel, A. Jonáš, and E.-L. Florin. “Three-dimensional tracking of fluorescent nanoparticles with subnanometer precision by use of off-focus imaging”. In: *Opt. Lett.* 28.2 (2003), pp. 69–71.

[107] M. F. Juette et al. "Three-dimensional sub-100 nm resolution fluorescence microscopy of thick samples". In: *Nat. Methods* 5.6 (June 2008), pp. 527–529.

[108] S. Ram et al. "High Accuracy 3D Quantum Dot Tracking with Multifocal Plane Microscopy for the Study of Fast Intracellular Dynamics in Live Cells". In: *Biophys. J.* 95.12 (2008), pp. 6025 –6043.

[109] S. Ram et al. "3D single molecule tracking with multifocal plane microscopy reveals rapid intercellular transferrin transport at epithelial cell barriers". In: *Biophys. J.* 103.7 (2012), pp. 1594–1603.

[110] M. Born and E. Wolf. *Principles of Optics*. Cambridge University Press, 1999.

[111] B. E. Sernelius. *Surface Modes in Physics*. Wiley-VCH, 2005.

[112] B. Richards and E. Wolf. "Electromagnetic Diffraction in Optical Systems. II. Structure of the Image Field in an Aplanatic System". In: *Proc. R. Soc. A* 253.1274 (1959), pp. 358–379.

[113] L. Novotny and B. Hecht. *Principles of Nano-Optics*. Cambridge University Press, 2006.

[114] W. A. Pliskin and R. P. Esch. "Effect of Numerical Aperture of Microscope Objectives on Film-Thickness Determinations". In: *J. Appl. Phys.* 39.7 (1968), pp. 3274–3276.

[115] E. M. V. Association et al. "Standard for characterization of image sensors and cameras". In: *EMVA Standard* 1288 (2010).

[116] R. Parthasarathy. "Rapid, accurate particle tracking by calculation of radial symmetry centers". In: *Nat. Methods* 9.7 (July 2012), pp. 724–726.

[117] P. K. Jain et al. "Calculated Absorption and Scattering Properties of Gold Nanoparticles of Different Size, Shape, and Composition: Applications in Biological Imaging and Biomedicine". In: *J. Phys. Chem B* 110.14 (2006), pp. 7238–7248.

[118] H. Brenner. "The slow motion of a sphere through a viscous fluid towards a plane surface". In: *Chem. Eng. Sci.* 16.3–4 (1961), pp. 242 –251.

[119] C. Tian and Y. Shen. "Structure and charging of hydrophobic material/water interfaces studied by phase-sensitive sum-frequency vibrational spectroscopy". In: *Proc. Natl. Acad. Sci. USA* 106.36 (2009), pp. 15148–15153.

[120] B. M. Regner et al. "Anomalous Diffusion of Single Particles in Cytoplasm". In: *Biophysical Journal* 104.8 (2013), pp. 1652 –1660.

[121] R. Langer and N. A. Peppas. "Advances in biomaterials, drug delivery, and bionanotechnology". In: *AIChE Journal* 49.12 (2003), pp. 2990–3006.

[122] T. Gong, D. T. Wu, and D. W. M. Marr. "Two-Dimensional Electrohydrodynamically Induced Colloidal Phases". In: *Langmuir* 18.26 (2002), pp. 10064–10067.

[123] A. Reinmüller et al. "Colloidal crystallization in the quasi-two-dimensional induced by electrolyte gradients". In: *The Journal of Chemical Physics* 136.16, 164505 (2012).

[124] L. R. Huang et al. "Continuous Particle Separation Through Deterministic Lateral Displacement". In: *Science* 304.5673 (2004), pp. 987–990.

[125] M. Grzelczak et al. "Directed self-assembly of nanoparticles". In: *ACS Nano* 4.7 (2010), pp. 3591–3605.

[126] R. J. Hunter and L. R. White. *Foundations of colloid science*. Clarendon Oxford, 1987.

[127] A. Dhinojwala and S. Granick. "Micron-gap rheo-optics with parallel plates". In: *J. Chem. Phys.* 107.20 (1997), pp. 8664–8667.

[128] C. Clasen and G. H. McKinley. "Gap-dependent microrheometry of complex liquids". In: *J. Non-Newtonian Fluid Mech.* 124.1 (2004), pp. 1–10.

[129] J. Tae Kim, S. Spindler, and V. Sandoghdar. "Scanning-aperture trapping and manipulation of single charged nanoparticles". In: *Nat. Commun.* 5 (2014), p. 3380.

[130] E. R. Dufresne, D. Altman, and D. G. Grier. "Brownian dynamics of a sphere between parallel walls". In: *EPL (Europhysics Letters)* 53.2 (2001), p. 264.

[131] N. Kaji et al. "Study of water properties in nanospace". In: *Analytical and Bioanalytical Chemistry* 386.3 (2006), pp. 759–764.

[132] G. Volpe, G. Volpe, and S. Gigan. "Brownian Motion in a Speckle Light Field: Tunable Anomalous Diffusion and Selective Optical Manipulation". In: *Sci. Reports* 4 (Jan. 2014), pp. 3936–.

[133] B. Conway, A Dobry-Duclaux, and F Eirich. "Rheology: Theory and Applications". In: vol. 3. Academic Press New York and London, 1960, p. 83.

[134] M. D. Carbajal-Tinoco, G. Cruz de León, and J. L. Arauz-Lara. "Brownian motion in quasibidimensional colloidal suspensions". In: *Phys. Rev. E* 56 (6 1997), pp. 6962–6969.

[135] W Sparreboom, A Van Den Berg, and J. Eijkel. "Principles and applications of nanofluidic transport". In: *Nature nanotechnology* 4.11 (2009), pp. 713–720.

[136] M. Napoli, J. C. T. Eijkel, and S. Pennathur. "Nanofluidic technology for biomolecule applications: a critical review". In: *Lab on a Chip* 10.8 (2010), pp. 957–985.

[137] P. Hänggi and F. Marchesoni. “Artificial Brownian motors: Controlling transport on the nanoscale”. In: *Reviews of Modern Physics* 81.1 (2009), p. 387.

[138] J. Rousselet et al. “Directional motion of Brownian particles induced by a periodic asymmetric potential”. In: *Nature* 370.6489 (1994), pp. 446–448.

[139] L. Faucheux et al. “Optical thermal ratchet”. In: *Physical review letters* 74.9 (1995), p. 1504.

[140] L Gorre-Talini, S Jeanjean, and P Silberzan. “Sorting of brownian particles by the pulsed application of an asymmetric potential”. In: *Physical Review E* 56.2 (1997), p. 2025.

[141] L. Bogunovic et al. “Particle sorting by a structured microfluidic ratchet device with tunable selectivity: theory and experiment”. In: *Soft Matter* 8.14 (2012), pp. 3900–3907.

[142] K. Mathwig, F. Müller, and U. Gösele. “Particle transport in asymmetrically modulated pores”. In: *New Journal of Physics* 13.3 (2011), p. 033038.

[143] J. Nilsson et al. “Review of cell and particle trapping in microfluidic systems”. In: *Analytica chimica acta* 649.2 (2009), pp. 141–157.

[144] Y. Pang and R. Gordon. “Optical trapping of a single protein”. In: *Nano letters* 12.1 (2011), pp. 402–406.

[145] R. Krupke et al. “Separation of metallic from semiconducting single-walled carbon nanotubes”. In: *Science* 301.5631 (2003), pp. 344–347.

[146] M. A. Gerspach et al. “Glass-based geometry-induced electrostatic trapping devices for improved scattering contrast imaging of nano-objects”. In: *Microelectron. Eng.* 145.0 (2015), pp. 43 –48.

[147] M. Celebrano et al. “Angular trapping of anisometric nano-objects in a fluid”. In: *Nano letters* 12.11 (2012), pp. 5791–5796.

[148] C. J. Myers, M. Celebrano, and M. Krishnan. “Information storage and retrieval in a single levitating colloidal particle”. In: *Nature nanotechnology* 10.10 (2015), pp. 886–891.

[149] W. P. Wong and K. Halvorsen. “The effect of integration time on fluctuation measurements: calibrating an optical trap in the presence of motion blur”. In: *Opt. Express* 14.25 (2006), pp. 12517–12531.

[150] M. Krishnan et al. “Electrostatic Self-Assembly of Charged Colloids and Macromolecules in a Fluidic Nanoslit”. In: *Small* 4.11 (2008), pp. 1900–1906.

[151] M. Krishnan, I. Mönch, and P. Schwille. “Spontaneous Stretching of DNA in a Two-Dimensional Nanoslit”. In: *Nano Letters* 7.5 (2007), pp. 1270–1275.

[152] N. R. Jana, L. Gearheart, C. J. Murphy, et al. "Seed-mediated growth approach for shape-controlled synthesis of spheroidal and rod-like gold nanoparticles using a surfactant template". In: *Advanced Materials* 13.18 (2001), p. 1389.

[153] C. J. Johnson et al. "Growth and form of gold nanorods prepared by seed-mediated, surfactant-directed synthesis". In: *J. Mater. Chem.* 12 (6 2002), pp. 1765–1770.

[154] C. J. Murphy et al. "Anisotropic Metal Nanoparticles: Synthesis, Assembly, and Optical Applications". In: *The Journal of Physical Chemistry B* 109.29 (2005), pp. 13857–13870.

[155] X. Huang et al. "Cancer Cell Imaging and Photothermal Therapy in the Near-Infrared Region by Using Gold Nanorods". In: *Journal of the American Chemical Society* 128.6 (2006), pp. 2115–2120.

[156] G. von Maltzahn et al. "Computationally Guided Photothermal Tumor Therapy Using Long-Circulating Gold Nanorod Antennas". In: *Cancer Research* 69.9 (2009), pp. 3892–3900.

[157] B. Jang et al. "Gold Nanorod – Photosensitizer Complex for Near-Infrared Fluorescence Imaging and Photodynamic/Photothermal Therapy In Vivo". In: *ACS Nano* 5.2 (2011), pp. 1086–1094.

[158] O. Bar-Ilan et al. "Toxicity assessments of multisized gold and silver nanoparticles in zebrafish embryos". In: *Small* 5.16 (2009), pp. 1897–1910.

[159] B. Pietrobon, M. McEachran, and V. Kitaev. "Synthesis of size-controlled faceted pentagonal silver nanorods with tunable plasmonic properties and self-assembly of these nanorods". In: *ACS nano* 3.1 (2008), pp. 21–26.

[160] C. Rawlings et al. "Accurate Location and Manipulation of Nanoscaled Objects Buried under Spin-Coated Films". In: *ACS Nano* 9.6 (2015), pp. 6188–6195.

[161] K. A. Dick et al. "InAs nanowires grown by MOVPE". In: *Journal of crystal growth* 298 (2007), pp. 631–634.

[162] G. A. Parks. "The isoelectric points of solid oxides, solid hydroxides, and aqueous hydroxo complex systems". In: *Chemical Reviews* 65.2 (1965), pp. 177–198.

[163] J. Canny. "A computational approach to edge detection". In: *IEEE Transactions on pattern analysis and machine intelligence* 6 (1986), pp. 679–698.

[164] C.-C. Lee et al. "Multistep synthesis of a radiolabeled imaging probe using integrated microfluidics". In: *Science* 310.5755 (2005), pp. 1793–1796.

[165] A. Ohlinger et al. "Optically trapped gold nanoparticle enables listening at the microscale". In: *Physical review letters* 108.1 (2012), p. 018101.

# List of Symbols

| | |
|---|---|
| $a$ | particle radius |
| AFM | **a**tomic **f**orce **m**icroscope |
| $A_H$ | Hamaker constant |
| AOD | **a**cousto-**o**ptic **d**eflector |
| $c$ | ionic concentration |
| $\gamma$ | fraction of incoming light interacting with the particle |
| CSA | **c**oherent **s**uperposition **a**pproximation |
| CTAB | **c**etyl**t**rimethyl**a**mmonium **b**romide |
| $d$ | gap distance in the nanofluidic slit |
| $D_0$ | bulk diffusion coefficient |
| D263 | borosilicate cover-glass |
| $\zeta$ | zeta potential |
| FPS | **f**rames **p**er **s**econd |
| $\eta$ | bulk dynamic viscosity |
| $h$ | particle height |
| HM | cross linking polymer (HM8006, JSR) |
| $I$ | ionic strength |
| $I'$ | normalized intensity |
| iSCAT | **i**nterferometic **s**cattering **d**etection |
| $\kappa^{-1}$ | Debye length |
| $k_B$ | Boltzmann constant |
| $k_r$ | radial trapping stiffness |
| LSA | **l**inear **s**uperposition **a**pproximation |
| MSD | **m**ean **s**quared **d**isplacement |
| NA | **n**umerical **a**perature |
| $N_A$ | Avogadro constant |
| NCA | **n**anofluidic **c**onfinement **a**pparatus |
| $p$ | scattering amplitude of the particle |
| PPA | **p**oly**p**hthal**a**ldehyde |
| SEM | **s**canning **e**lectron **m**icroscope |
| SNR | **s**ignal to **n**oise **r**atio |
| $T$ | absolute temperature |
| $\tau_{exp}$ | camera exposure time |

| | |
|---|---|
| $\tau_{illu}$ | illumination time per particle |
| $\tau_{line}$ | time per line scan |
| $\tau_{rel}$ | relaxation time |
| tSPL | **t**hermal **s**canning **p**robe **l**ithography |
| $\phi_0$ | effective scattering phase of the particle |
| $W_{PP}$, $W_{PS}$, $W_{SS}$ | interaction energies between (P)lane and (S)phere |
| $\Psi$ | electrostatic potential |
| $\Psi_0$ | electrostatic surface potential |

# Acknowledgments

I had the opportunity to carry out this thesis at IBM Research - Zurich and at the group of Control and Manipulation of Matter at the Nanoscale at the University of Zurich (UZH). The outcome of this thesis and the great time I have had is also the result of the many positive contributions from several people. I am grateful to all of them. In particular, I would like to thank the people from the group of Physics of Nanoscale Systems at IBM with whom I worked together on a daily basis for all the discussions about science and other important topics during coffee and lunch breaks.

The project was led by Armin Knoll at IBM, who is such a pleasant and joyful character that it is hard to imagine a better advisor. Thank you for all the support and encouragement. Every day I could step into his open office and ask him any question and he has always answered them with patience and serenity. I learned a lot from his way of doing research, his style of writing papers and his composure of playing pool.

At the University of Zurich Madhavi Krishnan was my supervising professor. I thank her for doing an efficient job, the fruitful discussions and the freedom I have had to carry out this project.

In terms of patterning the ratchets and topographical traps I thank especially Colin Rawlings and Armin Knoll. Both supported me in using tSPL and I wish SwissLitho all the best in distributing this versatile patterning technique.

The first PostDoc who joined the project was Mike Skaug and he pursued the goal of using the system to realize the first rocking Brownian ratchet to transport nanoparticles. Unfortunately, he left just after the first successful experiments were carried out. Fortunately, a few month later Christian Schwemmer joined also as a PostDoc and together we carried out two of the experiments shown in this thesis. Thank you for doing an excellent job.

Heiko Wolf and Urs Dürig are the two other permanent researchers, which were involved in the project and I benefited a lot from their profound chemical and physical knowledge. Furthermore, I would like to thank the three managers I had during my time at IBM Michel Despont, Urs Dürig and Rolf Allenspach and

the manager of Science & Technolgy Walter Riess for establishing a professional and pleasant work environment.

I also appreciate a lot the work-life-balance at IBM created by the events of the IBM Hobby Club, our group, and the PhD community: The IBM ski weekends, the weekly training sessions and going to Tenero with the soccer team, the river rafting, the wine tasting on the boats, the BBQs at the lake and the nights in downtown Zurich. For the wonderful experiences and long lasting memories I would like to thank all the people I have met and in particular Colin Rawlings, Martin Spieser, Olivier Gallay, Bruno Schuler, Stefan Abel, Felix Holzner, Philip Eib, Martina Hitzbleck, Daniel Grogg, "the coach" Marcus Oestreicher, Antonio La Porta, Julien Cors, Steffen Reidt, Armin Knoll, Philip Paul, Samuel Bisig, Heiko Wolf, Songbo Ni, Elad Koren, Keith Carroll, Christian Schwemmer and Yu Kyoung Ryu Cho.

Furthermore, I would like to thank ...

... Stefan Seeger for being the third member of my doctoral committee.

... Cristina Benea for introducing me to the first NCA prototype built by Felix Holzner.

... the people from the model shop for all the excellent work they have done.

... Ute Drechsler for helping me with the fabrication of the glass mesas.

... Steffen Reidt for writing the optical masks.

... Meinrad Tschudy for evaporating the metal layers.

... Marilyne Sousa for providing the ellipsometry measurements.

... Songbo Ni and Nassir Mojarad for helping me with the Zetasizer measurements.

... Rainer Mahrt and Thilo Stöferle for helping out with optical equipment.

... Charlotte Bolliger for proofreading the manuscripts.

... Christian Schwemmer and Keith Carroll for proofreading the thesis.

... you for reading the thesis.

... last but not least my family and Christin.

# Curriculum Vitae

## PERSONAL DETAILS

Name: Stefan Fringes
Date of birth: 31.07.1985
E-Mail : stefan.fringes@rwth-aachen.de

## ACADEMIC CAREER

| | |
|---|---|
| 10/2012 – 01/2017 | UZH Zurich, Switzerland<br>PhD Thesis, Group of Prof. Madhavi Krishnan |
| 10/2005 – 07/2011 | RWTH-Aachen, Germany<br>Studies of Physics |
| 01/2009 – 06/2009 | KTH-Stockholm, Sweden<br>Semester abroad with ERASMUS-grant |

## PROFESSIONAL CAREER

| | |
|---|---|
| 10/2012 – 12/2016 | PhD Thesis at IBM Research - Zurich, Switzerland<br>Research in the Physics of Nanoscale Systems group |
| 06/2012 | Internship at BVK-Patent in Cologne, Germany |
| 06/2010 – 10/2011 | Diploma Thesis at RWTH-Aachen, Germany<br>Research in the carbon nanoelectronics group |
| 07/2009 – 02/2010 | Student assistant at RWTH-Aachen, Germany<br>Laser polishing at the Chair for Technology of Optical Systems |
| 07/2008 – 12/2008 | Student assistant at RWTH-Aachen, Germany<br>Fabrication of GaN-Devices at the Chair of Electromagnetic Theory |

- S. Fringes, F. Holzner, and A. W. Knoll. “The Nanofluidic Confinement Apparatus: Studying confinement dependent nanoparticle behavior and diffusion”. Submitted to Journal of Chemical Physics
- S. Fringes, M. Skaug, and A. W. Knoll. “In situ contrast calibration to determine the height of individual diffusing nanoparticles in a tunable confinement”. In: *Journal of Applied Physics* 119.2, 024303 (2016)
- C. Volk, C. Neumann, S. Kazarski, S. Fringes, S. Engels, F. Haupt, A. Müller, and C. Stampfer. “Probing relaxation times in graphene quantum dots”. In: *Nature communications* 4 (2013), p. 1753
- S. Fringes, C. Volk, B. Terrés, J. Dauber, S. Engels, S. Trellenkamp, and C. Stampfer. “Tunable capacitive inter-dot coupling in a bilayer graphene double quantum dot”. In: *physica status solidi (c)* 9.2 (2012), pp. 169–174
- S. Fringes, C. Volk, C. Norda, B. Terrés, J. Dauber, S. Engels, S. Trellenkamp, and C. Stampfer. “Charge detection in a bilayer graphene quantum dot”. In: *physica status solidi (b)* 248.11 (2011), pp. 2684–2687
- C. Stampfer, S. Fringes, J. Güttinger, F. Molitor, C. Volk, B. Terrés, J. Dauber, S. Engels, S. Schnez, A. Jacobsen, et al. “Transport in graphene nanostructures”. In: *Frontiers of Physics* 6.3 (2011), pp. 271–293
- C. Volk, S. Fringes, B. Terrés, J. Dauber, S. Engels, S. Trellenkamp, and C. Stampfer. “Electronic excited states in bilayer graphene double quantum dots”. In: *Nano letters* 11.9 (2011), pp. 3581–3586